THE ANISOTROPY OF MOMENTUM DISTRIBUTIONS IN ATOMIC COLLISION CASCADES

Marc Hou*) and Wolfgang Eckstein

IPP 9/65 May 1988

MAX-PLANCK-INSTITUT FÜR PLASMAPHYSIK

8046 GARCHING BEI MÜNCHEN

MAX-PLANCK-INSTITUT FÜR PLASMAPHYSIK

GARCHING BEI MÜNCHEN

THE ANISOTROPY OF MOMENTUM DISTRIBUTIONS IN ATOMIC COLLISION CASCADES

Marc Hou*) and Wolfgang Eckstein

IPP 9/65 May 1988

*)Université Libre de Bruxelles, CP 234, Bd du Triomphe,
B-1050 Brussels, Belgium

Die nachstehende Arbeit wurde im Rahmen des Vertrages zwischen dem Max-Planck-Institut für Plasmaphysik und der Europäischen Atomgemeinschaft über die Zusammenarbeit auf dem Gebiete der Plasmaphysik durchgeführt.

IPP 9/65

M. Hou
W. Eckstein

The anisotropy of momentum distributions in atomic collision cascades

Abstract

The distribution of particle momentum directions in atomic collision cascades are studied by means of computer simulation with the MARLOWE program. In contrast with the random model, the atomic collision cascade generation in single crystals is found to be highly anisotropic at every stage of the energy dissipation. It is entirely governed by the lattice crystallography. In addition to the well known one-dimensional focusing effects, two-dimensional transient focusing is found to play an important role in the cascade development. Unstable one-dimensional trajectory focusing also provides a large contribution to the momentum direction distributions at various stages of the cascade generation. Large thermal displacements of lattice atoms are not found to randomize the cascades. They may, however, induce anisotropy characteristics in momentum direction distributions different from those calculated for a static lattice. The anisotropy found in experimental and simulated angular distributions of sputtered particles is directly related to the anisotropy of the cascade development and is only poorly described by earlier interpretations.

I. Introduction

Analytical collision cascade theories usually make use of a Boltzmann gas model /1-3/. Strong assumptions are inherent to this model, which however allows useful predictions for dense materials, in particular, on the basis of linearized transport equations /4/.

One of the basic assumptions is that of isotropy, namely, that at each collision step, all possible collision events are equally probable. Atoms are then assumed to be randomly distributed in the material, within Poisson statistics. The assumption of isotropy is still used in quite recent work /5,6/. Its range of validity was however never properly investigated, in particular, in the case of collision cascades developing in single or poly-crystals, which most frequently represents the experimental situation.

Until now, the influence of the target structure on the atomic motion gave rise to the study of particular processes: the channeling of slowing down particles /7-9/ and focused collison sequences /9/. Channeling is usually distinguished from the cascade generation, although the possibility of its influence on the motion of recoiling atoms was recently pointed out /10/. Models for focusing chains were established /11-13/. Since their length is usually rather short, they were considered as having no major effect on many collision cascade characteristics. One exception is the angular distribution of sputtering from single crystals, which is known to display an anisotropic character /14/. This one was generally attributed to atomic ejection in low index crystallographic directions by nascent focusing /15/ or stable /13/ focused collision chains.

The relative contribution of such correlated events to sputtering in preferential directions was only evaluated recently.

Computer simulation methods however allow to avoid many assumptions required in order to develop an analytical theory and were already used to study the sputtering from single crystals /9/ and the spatial configuration of atomic displacements /10,16,17/. Limited aspects of momentum distributions in collision cascades were emphasized recently, which do not account for the effects of the lattice ordering /18,19/.

It is the purpose of the present work to investigate the strong anisotropy of momentum distributions in single crystal structures as well as their evolution as the energy dissipation evolves. This is done by computer simulation. It will be shown that isotropy has only little to do with the development of collision cascades in structured materials. The relation to sputtering angular distributions is not straightforward, but will be made on the basis of detailed analysis of the various contributing processes.

II. The Simulation Model

The MARLOWE computer simulation code /20/ was used for the present calculation. We used it already for sputtering calculations /21,22/ and the comparison with experiment allowed to adjust the model parameters reasonably well. The same parameters are thus used in the present calculations. The disucssion is based on the example of cascades generated in single gold crystals by neon or xenon energetic incident atoms.
The MARLOWE code is based on the binary collision approximation. The atomic collisions are governed by the pairwise Moliére potential /23/ with the screening length for gold suggested by Robinson /20/. Firsov screening

distances /24/ are assumed to be valid for rare gas atoms and these for heteronuclear pairs (Ne-Au, Xe-Au) are estimated as harmonic means of the screening lengths for the homonuclear pairs /25/.

Between collisions, particles are assumed to move at constant velocity along their asymptotic trajectories. Provision is made for an approximate treatment of quasi-simultaneous collisions. Exception made for the case of replacement sequences, a zero binding energy is used for the gold atoms to their lattice sites. A small binding energy is assumed for replacement collisions (0.2 eV) in order to correct for the many body nature of such events /9/. This approach was discussed in details on the basis of comparison with molecular dynamic calculations. The energy dissipation through binary collisions proceeds until the kinetic energy of the moving particles falls below a preset cut-off value, which is also used as an energy displacement threshold (3.78 eV). Inelastic energy loss is assumed to be shared between local and non local electron excitations, according to Oen and Robinson /26/ and Lindhard /27/ respectively. A surface of incidence is assumed and its effect on the atomic motion will be analyzed in details, in relation with the discussion of sputtering.

Time is not a directly available cascade characteristic in binary collision models. Therefore, the scheduling of the collision events has to be made on another basis. In the Marlowe code, after each collision step, the fastest atom is selected as the next projectile to be followed, until all cascade particles have their kinetic energy below the cut-off value. Some minor atom permutations may occur, that are typical of hashing algorithms as used here in order to speed up the cascade calculations. Since the energy dissipates as the time proceeds, the scheduling of the atomic displacements as performed in the present model may well be reasonable. The present work

focuses on the evolution of the angular distribution of atomic motion as the kinetic energy dissipates. Such angular distributions are recorded for all particles entering a pre-specified kinetic energy interval. Consecutive intervals are taken as $(E_0/2^n, E_0/2^{n+1})$ where E_0 is the primary energy, for increasing integer values of n, until the cut-off energy is reached.

III. Angular Distribution of the Atomic Motion

a) Scattering cross-section distributions

Statistical independence of collision events in a collision cascade is only possible if the path length between successive collisions is large with regard to the collision radius /28/. This is generally not the case in solids and the question is to identify how large the deviations from the random cascade model are.

A first approach may be done on the basis of total cross-section distributions. As simulated cascades are concerned, such distributions are easily obtained by scoring the collision frequency as a function of the impact parameter squared. This is shown in fig. 1 and the cases of amorphous, polycrystalline and crystalline gold targets are compared to the uniform distribution of a random cascade model. The computer results indicate that structures occur in the impact parameter distributions that correspond to head-on collisions like in focusing chains and the simultaneous interaction with rings of atoms in the {111}, {100} and {110} planes. The structures are identical in the single and polycrystal cases, showing that the influence of the incidence conditions on the collision

probability distribution in a cascade is negligeable. It should be noticed that the short range structure in the amorphous model material has a significant influence on the collision statistics. The sharp peaks observed for poly and single crystals at close to zero impact parameters and associated to 110 rings reflects the efficiency of assisted focusing in the 110 directions.

These impact parameter distributions may be energy dependent. On the other hand, since the impact parameter at a given energy is directly related to the scattering angle, the energy dependence of collision statistics and its evolution with energy dissipation can also be viewed in terms of momentum distibutions. These allow a rather detailed analysis of the cascade development, as it comes out of the next sections.

b) Angular distributions in the bulk

The distributions are represented in the form of contour line plots of equal fluxes. The number of contour lines is limited to 20. The highest level is associated to the highest flux.

In figs. 2 to 10, the angular distributions of motion are compared between gold targets irradiated with 2.5 keV neon and xenon atoms, respectively. When scanning from fig. 2 to fig. 10, the most striking feature is the strong anisotropy of the angular distributions and its evolution as the energy dissipates. The only exception is the fig. 2a, representing the highest energy distribution (close to half the primary energy) in the case of neon slowing down. These scattering energies are above the maximum transferable energy between an incident neon and a gold atom (837 eV). The distribution thus represents the angular distribution of moving neon atoms

only. In fig. 2b (xenon incident particles), the distribution is already dominated by moving gold atoms.

Another overall feature is that, at all energies, more cascade atoms move forward than backward. To a large extend, this is due to the occurrence of a surface of incidence through which atoms can escape. A similar, but depth resolved analysis might bring better details about forward to backward flux ratios. This was already done in /19/ with another code and will not be discussed here. However, the major anisotropies that are featured in the present work could not be detected in /19/ because the analysis was not performed with angular resolution.

The relation between anisotropy and crystal structure can be analyzed in details by a comparison of the contour plots with the low index crystallographic directions and the loci of the directions parallel to the major low index crystallographic planes. These are given in fig. 11a and an example of superimposition with a contour plot is given in fig. 11b. From this latter figure, the correlation between the directions of atomic motion and the lattice structure obviously appears to dominate the cascade development. It is also seen that one-dimensional focusing is not sufficient to account for all the anisotropies. Two-dimensional focusing parallel to {110} planes has a significant contribution in this figure as well. The analysis of figs. 2 to 10 allows the following description:

Figure 2 represents the direction distributions of moving atoms after the first collision at which their energy falls below $E_0/2$. The rather isotropic distribution in fig. 2a was already assigned to neon atoms and reflects the large differential cross-section for large scattering angle of light particles by heavy target atoms. The distribution in the xenon case (fig. 2b) displays a major focusing direction parallel to 100 atomic

rows. The apparent steering along {110} planes is not real. The scale in the abscissa is not linear and the spots are roughly circularly shaped, with a full width at half maximum of about 30 degrees. Focusing along <111> and close to <221> directions also occurs, with less intensity. These represent open directions up to the third and fourth neighbour distance respectively. When the energy dissipates further and gets lower than $E_0/2^2$ (fig. 3), the distributions in the neon and the xenon cases display clear similarities. In addition to the focusing directions found in fig. 2b, momentum starts to turn back toward the surface of incidence. <111> spots are reinforced with regard to <100>. This is not the case for focusing close to the <221> direction. <100> focusing starts toward the surface, which is clear in the neon case and nascent for xenon. No <111> focusing occurs yet toward the surface in the neon case. Figure 3b displays a significant steering between <111> and <110> directions, which represents 2-D focusing parallel to {110} planes. When the energy gets lower than $E_0/2^3$, the distributions gain in complexity, although remaining strongly anisotropic in the case of xenon (fig. 4b). The anisotropic features appearing in fig. 3a are reinforced in fig. 4a. The addition features appearing in fig. 4b have two different origins: one is the greater focusing efficiency in <100> directions toward the surface, the other is the strong increase in the number of trajectories fed toward the <221> directions.

The occurrence of nascent spots in the forward <110> directions can be seen as well. When the energy still dissipates further (below $E_0/2^4$), the situation starts clarifying. It can be seen by comparison between fig. 5a and 5b, that the distributions become quite similar, whatever the projectiles are, although (fig. 12) the number of moving atoms is more than

a factor of two smaller in cascades generated by neon than by xenon. It can be noticed also that the kinetic energy of moving atoms becomes close to the replacement threshold, which comes out to be about 120 eV in the present calculations. The focusing in {110} planes in directions close to parallel to the surface is striking as well as the strong spots in the <110> directions toward the surface. The relative intensity of the <100> spots decreases. When the energy still decreases, focusing in the <110> directions becomes clearly dominant and a weak focusing in directions parallel to {111} planes is seen in fig. 6a and 6b. It can be associated with the flux enhancement in the <112> directions as seen in those that are the closest to the surface normal. This situation is most enhanced for particles whose energy get below $E_0/2^6$ (39 eV), as seen in fig. 7. the 1-D focusing occuring at higher energy is most enhanced. In addition, spots due to focusing in short range open directions emerge again. The <100> spots have almost disappeared. When the energy still dissipates further (fig. 8), the complexity increases again, because of the relative enhancement of focusing in short range directions, coupled with 2-D focusing parallel to {111} and {110} planes. As shown in fig. 9, planar focusing decreases with regard to 1-D focusing in both low index close packed (<110> and <112>) and short distance open directions (<221>) when the energy dissipation proceeds below $E_0/2^8$ (9.77 eV). The stronger intensity close to <221> than in the <110> directions toward the surface can be noticed in fig. 9b, giving rise, among other, to the six fold symmetric pattern with the spots in the <112> directions.

It turns out from this rather extensive description that the all collision cascade development can be interpreted in terms of crystallographic

effects. Both close packed rows and more open directions play an important role. Planar focusing is unstable and contribute to feed the sequences of particle trajectories from short range open directions (<221>) to <110> directions. <100> focusing plays an important role at high energy and its effect disappears rather fast as the energy dissipates. The same happens with focusing in the <111> directions, but to a smaller extent. The evolution of the patterns described above is governed by the different efficiencies of the various kinds of focusing effects as the energy dissipates. Finally, the rather long memory of th projectile can be noticed. Indeed, it is only when the energy per moving atom gets below about 160 eV (fig. 5) that qualitative differences between cascades generated by heavy and light primaries becomes insignificant. As shown in fig. 12, the number of colliding atoms increases differently as the energy dissipates, when the cascades are initiated by light and by heavy projectiles. They become similar, and the memory of the projectile is thus completely lost only when the kinetic energy of the moving atoms becomes smaller than 40 eV.

Further evidence for the progressive loss of memory of the incendent conditions is found in the comparison of flux angular distributions for different primary energies. In figs. 13 to 17, flux distributions are compared for moving atoms with similar energies, but the xenon incendent energies are 0.6 keV (figs. 13-17a) and 2.5 keV (figs. 13-17b) respectively. It should be noticed, by comparing fig. 1b with fig. 14a that the starting of the cascade generations are very much alike. Both are dominated by peaks in the <100> forward directions and a minor preferentiality for the <221> open directions. No peak appears in the <111> forward directions in the low incidence energy case. This is a consequence

of the fact that at such low interaction energies, the large angle recoil cross-section is still rather small and the angular distribution is still dominated by primary recoils. The distribution in fig. 13a is quite different from that at the same energy in cascades generated by 2.5 keV xenon atoms. The similarities increase however as the energy dissipates and become almost identical at energies getting below about 37 eV (fig. 15 to 18). The only differences in fig. 18 concern the relative amount of atoms moving toward the surface, which is smaller in the low energy case. The relative intensities in the two families of spots displaying a six-fold symmetry close to the backward normal at the surface are completely different. This is not the case in the forward direction. It thus can only be related to the distance from the surface at which the cascades develop. Replacement sequences of course have a signifcant contribution to the anisotropy, especially in the low energy part of the cascade development. This contribution can be studied by comparison of the distributions in cascades in which they are truncated and in which they are not. The results are compared in figs. 19 to 24, from energies just above the replacement energy threshold (fig. 19) down to the cohesive energy (fig. 24). As expected, the patterns displayed in fig. 19a and 19b are similar since the kinetic energies are above the replacement threshold. The minor differences are due to statistical fluctuations. It is only at lower energies that significant differences take place. It clearly comes out in the figs. 20 to 24 that even when the replacement sequences are truncated, the distributions of momentum directions remain strongly anisotropic and the collison cascades essentially develop through 1-D and 2-D processes. A comparison between figs. 20a and b, with regard to fig. 11a indicates the contribution of replacement sequences to <110> peaks. Those corresponding

to the other families of close packed directions have similar profiles in both figs. 20a and 21a. This focusing process is achieved when the energy gets lower than 39 eV, as found by a comparison between fig. 22a and 22b. A strong focusing effect thus appears in the cascades, which is not due to replacement sequences. At this stage of the cascade development, it represents about half the contribution to focusing in <110> directions. This can be attributed to low energy channeling in directions parallel to replacement sequences. This low energy channeling is however unstable, as it comes out by a comparison between the peak profiles in fig. 22a and 23a. Indeed, in the latter, the <110> peaks are found to split again in directions parallel to {110} planes. In fig. 24a, they are found again, together with peaks close to the <221> directions. This situation correspond to kinetic energies just above the value of the cohesive energy. To this point, a static lattice is assumed. Thermal displacements of the atoms from their lattice sites may result in a disorganization of the patterns described above and of course the question arises to know whether they can lead to a randomization of the cascades. In order to investigate this problem, the simulations were repeated, assuming a temperature of 600 ^{o}K and uncorrelated thermal displacements, according to the Debye-Waller model /29/. Since thermal vibrations in a crystal are known to be correlated, the procedure is expected to overestimate the thermal effects on the cascade development. The results are given in the figs. 25 to 32 at successive steps of the energy dissipation. For clarity, the loci of directions parallel to {111} planes are superimposed to some contour plots. Focusing effects are not as pronounced as in the case of a static lattice, but the anisotropy of the flux distributions remains quite strong. The peaks associated to <111> directions at high energies do not occur as in

the static case. Although less intense, the same <100> spots remain. At lower energies, the structure of the direction distributions becomes more anisotropic but are quite different than in the case of a static lattice. The strong influence of {111} planes rather than {110} clearly appears. The peaks in the <110> directions are found to be produced as a consequence of the 2-D focusing in {111} planes (fig. 28), which becomes dominant as the energy dissipates further (fig. 29 and 30). This 2-D focusing is unstable and at low energies, typically below 20 eV (fig. 31 and 32) the patterns are dominated by focusing in <100> and <111> directions, as well as in the <221> short range open directions. Notice that the latter displays a six-fold symmetric pattern close to the backward normal at the surface, which is typical of sputtering patterns, as discussed below.

b) The origin of sputtering

The angular distributions analyzed above are not depth resolved. Since about 90 percent of the sputtering originates from the surface plane, its understanding requires the knowledge of the atomic flux distribution in the close vicinity of the surface. This is however not sufficient since once crossing the surface plane toward the vacuum, particles in the process of sputtering still have to undergo surface scattering from some of its close neighbours. In addition, they have to overcome surface binding forces that induce a further deflection of the outgoing trajectories toward the surface plane.

In order to follow the sputtering process, the atomic flux distributions in the close vicinity of the surface plane are compared at successive steps of the ejection process as a function of the kinetic energy. Three situations

are compared. The first is the flux distribution of atoms moving in the vicinity of the surface plane in the half space including the vacuum and limited at a distance of half a planar spacing beneath the surface. In the second, distributions are constructed as in the first situation but the flux of atoms moving in the vacuum is limited to the contribution of those that satisfy the sputtering criterium. In the third situation, the refraction of the trajectories in the vacuum is taken into account. In such a way, the sputtering angular distribution of atoms ejected with different kinetic energies is displayed. As expected, the lowest energy distributions (fig. 37c and 38c) feature similar angular distributions as obtained previously /22/. In fig. 33, no significant difference is to be seen between the different situations since the energies are still high enough that momentum is all directed forward. Momentum starts to turn toward the surface at a somewhat lower energy, as shown in fig. 34a. However, trajectories toward the vacuum are still directed rather close to the surface and surface scattering is not sufficient to help to overcome the surface energy barrier. At energies below 75 eV, a large fraction of momentum is turned back toward the surface (fig. 35). This however only concerns atoms coming from the bulk, located just beneath the surface plane and that do not retain enough energy after crossing the surface in order to be sputtered. Sputtering starts to be significant at lower energy, and a substantial contribution is found in fig. 36 (37 eV). Figure 36b shows that surface recoil prevents the ejection of atoms in directions close to the surface. The effect of the surface binding is to expand the direction distribution a little and to move the three fold spot pattern toward the surface. The structure of the spots is not seen in fig. 36a where a six-fold pattern occur. The structure in the sputtering distribution (fig. 36b

and c) are due to atoms fed into open directions. The major spots close to the backward surface normal in fig. 36a are <221>, those in fig. 28b and c are centered on <124> directions.

At lower energy, the pattern is dominated by <112> and <221> ejection (figs. 37b and c). The additional contribution of <124> ejection is noticed in the profile of the <221> spots. The peaks observed in the more oblique <124> directions in fig. 37a do not give rise to sputtering. The six-fold pattern observed in the sputtering distribution is associated to <110> and <221> directions. As the energy dissipates further (fig. 38), a minor contribution of <124> motion to sputtering is observed, displaying an additional six-fold pattern. This one was not detected experimentally /30/, and it was not significant enough to be emphasized in the related sputtering simulations /22/. The major six-fold pattern in the flux distribution of fig. 38a, giving rise to sputtering is here the result of a combination of <112> and <221> focusing processes.

At the lowest energies considered (fig. 39), the whole sputtering pattern is dominated by the major six-fold pattern resulting, as in fig. 38, from <112> and <221> focusing. The other features in the flux distribution toward the surface disappear, as a consequence of the surface energy barrier.

It thus turns out that the interpretation of the anisotropy in sputtering angular distributions is rather complex since, depending on the ejection energy, the origin of the contributions to the same spots is different. Insofar sputtering is dominated by low energy ejection, the major contribution to the spot pattern originates from <112> and <221> short range focusing. The contribution of <110> replacement sequences is small. At this point, it can be anticipated that energy and angular resolved

experiments might confirm the contribution of the other focusing processes predicted here.

IV. Conclusion

The present work clearly shows that collision cascades in single crystals are strongly anisotropic. This conclusion obviously applies to polycrystals as well since the spatial extend of collision cascades is generally smaller than the size of the crystal grains. The cascades are not found to randomize when the kinetic energy gets small and random thermal displacements of the atoms from their lattice sites do not randomize the cascades. Except as replacement sequences are concerned, the evolution of the anisotropy is governed by unstable one- and two-dimensional short range focusing processes. These also dominate the sputtering angular distributions which, in the present case study, cannot be associated to a major contribution of focusing chains.

The interatomic potential used was found in /22/ to provide the best prediction of sputtering yields and angular distributions. Therefore, it can reasonably be considered that the calculated low energy flux distributions are reasonable, although significant discrepancies in the relative sputtering intensities in the spots were found /22/ between experiment and simulation. These can be due both to a slight inaccuracy of the potential as well as to the increasing dynamical nature of the atomic interactions as the energy decreases. It also cannot be ruled out that some of the discrepancies originate from the experimental Au(111) surface which is known to have a complex structure. It is striking that the binary

collison approximation used in the present work and earlier sputtering studies /21,22/ still leads to reasonable predictions for processes dominated by low energy large impact parameter interactions, as the preferential sputtering in <221> and <112> directions.

References

/1/ J. Lindhard, Kgl. Dansk. Vid. Selsk. Mat.-Fys. Medd. 33, 10 (1968)

/2/ K.B. Winterbon, P. Sigmund and J.B. Sanders, Kgl. Dansk. Vid. Selsk. Mat.-Fys. Medd. 37, 14 (1970)

/3/ D.K. Brice and K.B. Winterbon, "Ion Implanted Ranges and Energy Deposition Distributions", Plenum Publishing Corporation (New York, Washington, London, 1975)

/4/ P. Sigmund, Phys. Rev. 184 (1969) 383

/5/ Y.T. Cheng, M. Nicolet and W.L. Johnson, Phys. Rev. Lett. 58 (1987) 2083

/6/ K.B. Winterbon, H.M. Urbassek, P. Sigmund and A. Gras-Marti, Phys. Scripta 36 (1987) 689

/7/ D. Onderdelinden, Can. J. Phys. 46 (1968) 739

/8/ J.B. Gibson, A.N. Goland, M. Milgram and G.H. Vineyard, Phys. Rev. 120 (1960) 1229

/9/ M.T. Robinson, in "Sputtering by Particle Bombardment, Physics and Applications", ed. R. Behrisch, Topics in Appl. Phys. (Springer, Berlin, Heidelberg, New York, 1981)

/10/ M. Hou, Phys. Rev. B 31 (1985) 4178

/11/ R.H. Silsbee, J. Appl. Phys. 28 (1957) 1246

/12/ G. Leibfried, J. Appl. Phys. 30 (1959) 1388

/13/ R.S. Nelson, M.W. Thompson and H. Montgomery, Phil. Mag. 7 (1962) 1385

/14/ G.K. Wehner, J. Appl. Phys. 26 (1955) 1056
G.K. Wehner, Phys. Rev. 102 (1956) 690

/15/ C. Lehmann and P. Sigmund, Phys. Stat. Sol. 16 (1966) 507

/16/ L. Heinisch, J. Nucl. Mater. 103/104 (1981) 1325

/17/ R. Dierckx, J. Nucl. Mater. 144 (1987) 214

/18/ W. Eckstein and W. Möller, Nucl. Instr. and Methods B 7/8 (1985) 727

/19/ H.J. Whitlow and M. Hautala, Nucl. Instr. and Methods B 18 (1987) 370

/20/ M.T. Robinson and I. Torrens, Phys. Rev. B 9 (1974) 5008

/21/ M. Hou and W. Eckstein, Nucl. Instr. and Methods B 13 (1986) 324

/22/ W. Eckstein and M. Hou, Nucl. Instr. and Methods, in press

/23/ G. Moliére, Z. Naturforsch. 2a (1947) 133

/24/ O.B. Firsov, Sov. Phys. JETP 6 (1958) 534

/25/ F. Smith, Phys. Rev. A 5 (1972) 1708

/26/ O.S.Oen and M.T. Robinson, Nucl. Instr. and Methods 132 (1976) 647

/27/ J. Lindhard, M. Scharff and H.E. Schiott, Kgl. Dansk. Vid. Selsk. Mat.-Fys. Medd. 40,5 (1978)

/28/ see e.g. P. Sigmund, Kgl. Dansk. Vid. Selsk. Mat.-Fys. Medd. 40,5 (1978)

/29/ Ch. Kittel, "Introduction to Solid State Physics", 3rd ed. (Wiley, New York, London, Sydney, 1968) p70
M. Blackman, "Handbuch der Physik", vol. VII, part 1 (Springer, Berlin, 1955) p377

/30/ W. Szymczak, Thesis, GSF-report 18/85, München (1985)

Figure Titles

Figure 1

Impact parameter squared distributions for collision cascades generated by 2.5 keV neon atoms at normal incidence on a gold target. The results obtained by simulation in the case of a single crystal with a (111) surface, of a polycrystal and of an amorphous target are compared with the uniform distribution associated with a random target model. The arrows indicate the impact parameter squared for the simultaneous interaction between a projectile and a ring of lattice atoms in {111}, {110} and {100} planes, when the trajectories passes through the center.

Figure 2 to 10

Contour line plots representing the angular distributions of atoms moving in the cascades generated by 2.5 keV Ne atoms (fig. 2 to 10a) and by 2.5 keV Xe atoms (fig. 2 to 10b) incident on a Au(111) surface. The abscissae represent the cosine of the polar angle, with respect to the inward surface normal and the ordinates represent the azimuth, with respect to a <110> surface direction. The plots are drawn for all particles whose kinetic energy get lower than $E_0/2^n$ but remains higher than $E_0/2^{n+1}$, with n increasing from n=1 in fig. 2 to n=9 in fig. 10. E_0 is the incident energy.

Figure 11

a) Loci of the directions parallel to the most compact crystallographic planes. Their intersections represent the close packed directions in the lattice, that are labelled in the figure. ΔΔΔ: loci of directions parallel to {100} planes, ooo: loci of directions parallel to {110} planes, +++: loci of the directions parallel to the {111} planes, ■ : <100> directions, ● : <110> directions, ◆ <111> directions, ▲ : <112> directions and ▼ : <221> directions.

b) Figure 11a is superimposed to a contour plot in order to illustrate how the latter can be analyzed in details. The focusing in close packed directions can be noticed, as well as in open directions. These are easily identified as close to <221> directions. The two-dimensional focusing parallel to {110} planes is visible too.

Figure 12

Ratio of the number of moving recoil atoms generated by 2.5 keV Ne and Xe atoms as a function of the motion energy. Each channel in the histogram concerns atoms whose energy gets lower than $E_0/2^n$ but remains larger than $E_0/2^{n+1}$, where E_0 = 2.5 kev is the projectile energy. Owing to the difference in the inelastic energy lost by Ne and Xe atoms, the ratios of energy available for damage is 0.79, which is quite close to the ratio of the number of moving atoms with energies lower than 39 eV (n=6).

Figures 13 to 18

Contour line plots representing the direction distributions of moving atoms in the cascades generated by 600 eV (fig. 13 to 18a) and 2.5 keV (fig. 13 to 18b) Xe atoms. The comparison is made at different steps of the energy dissipation, for cascade atoms moving with similar energies.

Figures 19 to 24

Contour line spots representing the direction distributions of moving atoms in cascades generated by 2.5 keV Xe atoms. In fig. 19 to 24a, replacement sequences are truncated, they are included in fig. 19 to 24b. The plots are drawn for energies just above the replacement threshold (fig. 19) down to the cohesive energy for gold (fig. 24).

Figures 25 to 32

Contour line plots representing the direction distributions of moving atoms in cascades generated by 2.5 keV Xe atoms. 600 ^{o}K uncorrelated thermal displacements of gold atoms are included in the simulations. The results are shown at different steps of the energy dissipation. The loci of the directions parallel to {111} planes are shown in each figure in order to guide the eyes when looking to the planar focusing effect.

Figures 33 to 39

Contour line plots representing the direction distributions of moving atoms in cascades generated by 600 eV Xe atoms. The plots are drawn for atoms whose kinetic energy get lower than $E_0/2^n$ but greater than $E_0/2^{n+1}$, with n increasing from n=1 in fig. 25 to n=7 in fig. 31. Three different situations are compared:

a) Direction distributions in the half space including the vacuum and limited to half the interplanar spacing,

b) Same as in a), but the distributions for atoms moving in the vacuum is limited to those that fulfil the conditions to get sputtered,

c) Same as in b), but the refraction effect by the surface binding forces is included.

Figure 1

Impact parameter squared distributions for collision cascades generated by 2.5 keV neon atoms at normal incidence on a gold target. The results obtained by simulation in the case of a single crystal with a (111) surface, of a polycrystal and of an amorphous target are compared with the uniform distribution associated with a random target model. The arrows indicate the impact parameter squared for the simultaneous interaction between a projectile and a ring of lattice atoms in {111}, {110} and {100} planes, when the trajectories passes through the center.

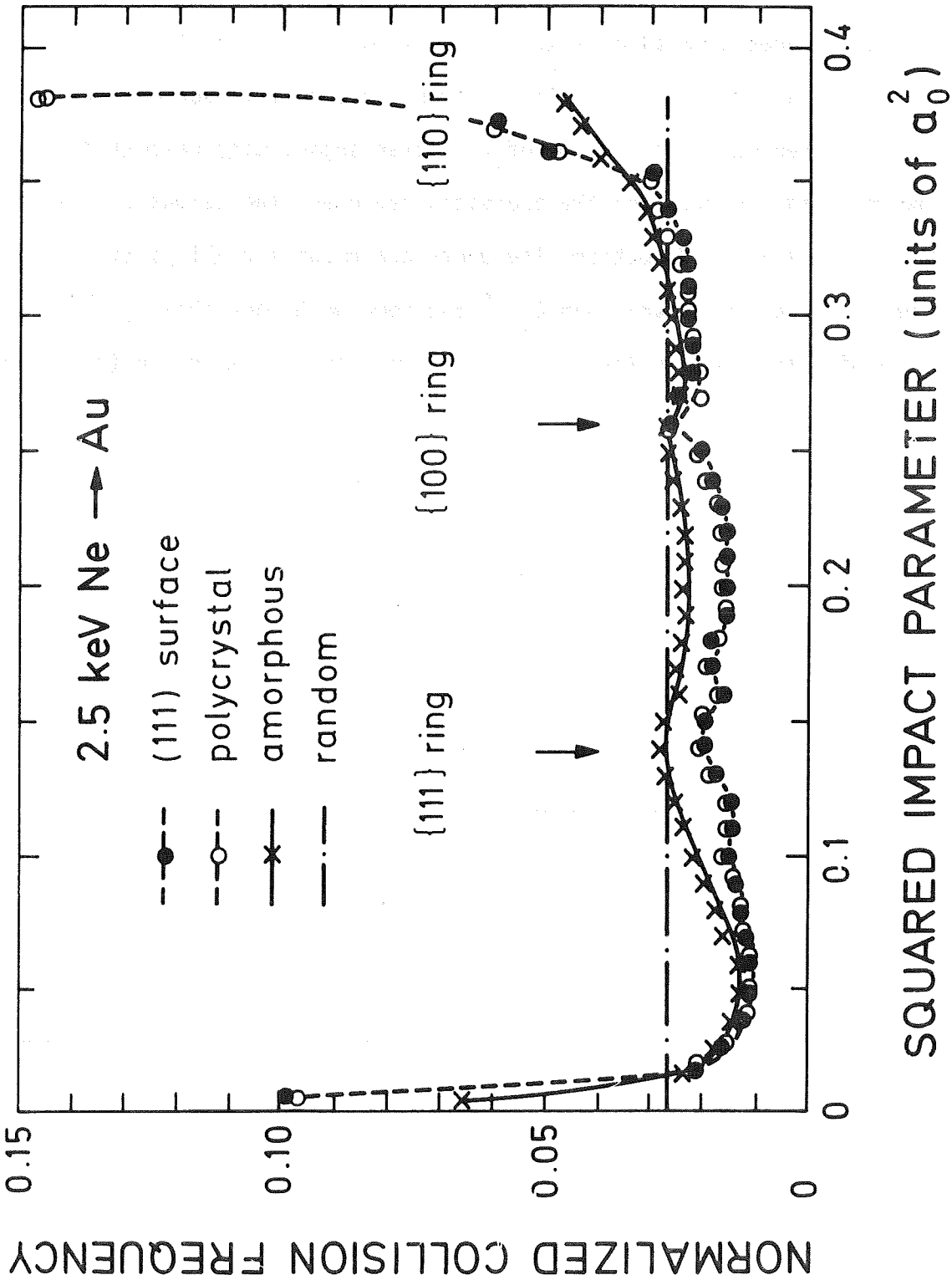
2.5 keV Ne → Au
(111) surface
polycrystal
amorphous
random
{111} ring
{100} ring
{110} ring
NORMALIZED COLLISION FREQUENCY
SQUARED IMPACT PARAMETER (units of a_0^2)
0
0.05
0.10
0.15
0.1
0.2
0.3
0.4

Fig. 1

Figure 2 to 10

Contour line plots representing the angular distributions of atoms moving in the cascades generated by 2.5 keV Ne atoms (fig. 2 to 10a) and by 2.5 keV Xe atoms (fig. 2 to 10b) incident on a Au(111) surface. The abscissae represent the cosine of the polar angle, with respect to the inward surface normal and the ordinates represent the azimuth, with respect to a <110> surface direction. The plots are drawn for all particles whose kinetic energy get lower than $E_0/2^n$ but remains higher than $E_0/2^{n+1}$, with n increasing from n=1 in fig. 2 to n=9 in fig. 10. E_0 is the incident energy.

PLNE1HA LIN , C2=0.73

a) 2.5 KEV NE -> AU (111) AT NORMAL INCIDENCE. E0/2 > E1 > E0/4.

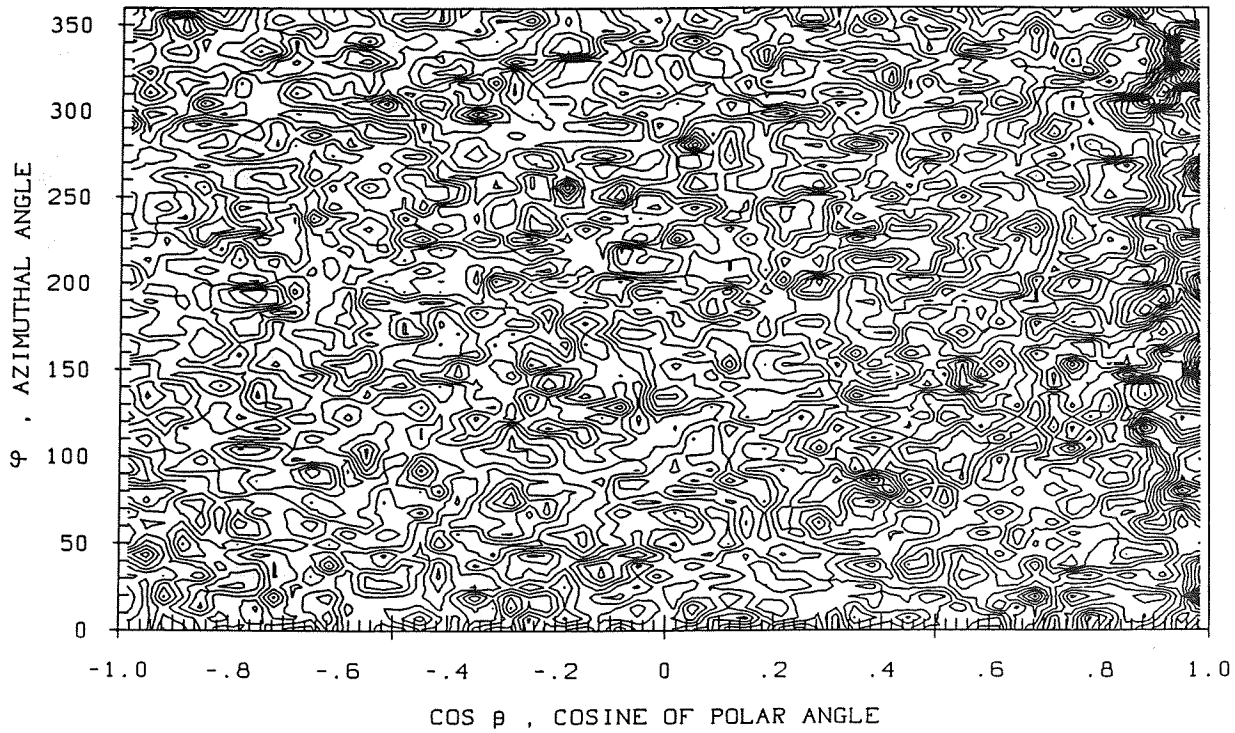

PLAU1HA LIN , C2=10.55

b) 2.5 KEV XE -> AU (111) AT NORMAL INCIDENCE. E0/2 > E1 > E0/4.

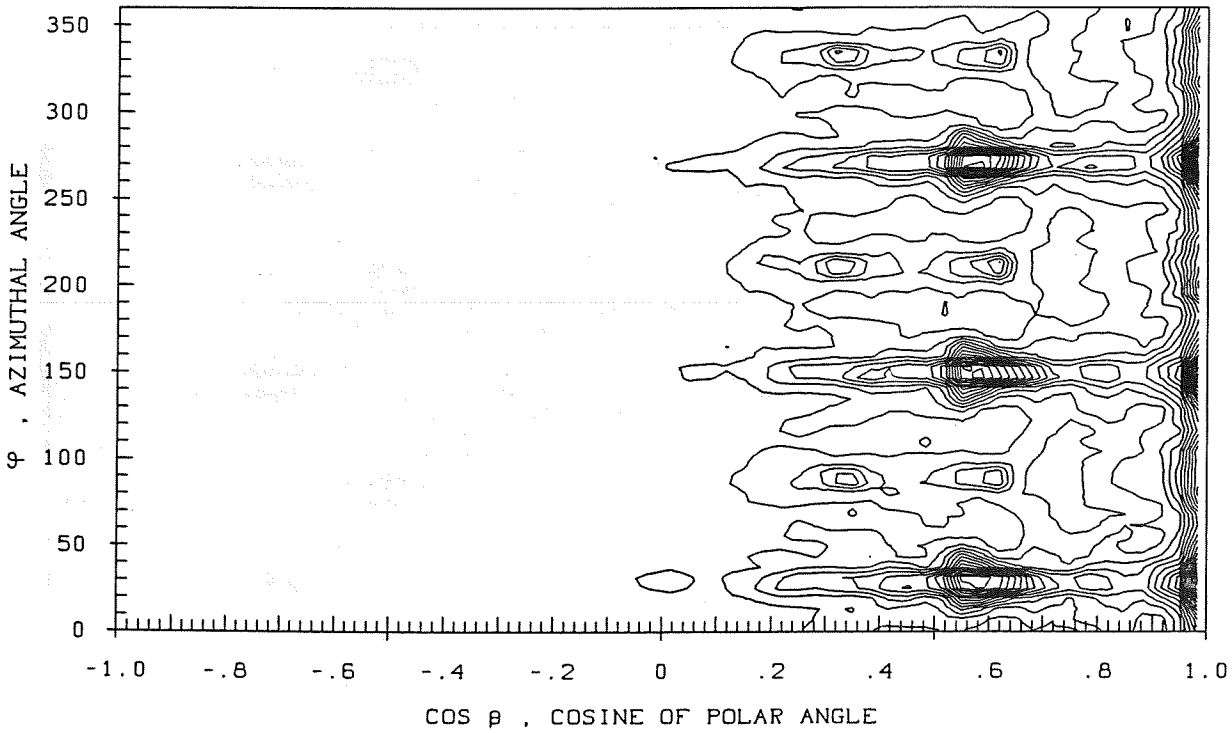

Fig. 2a,b

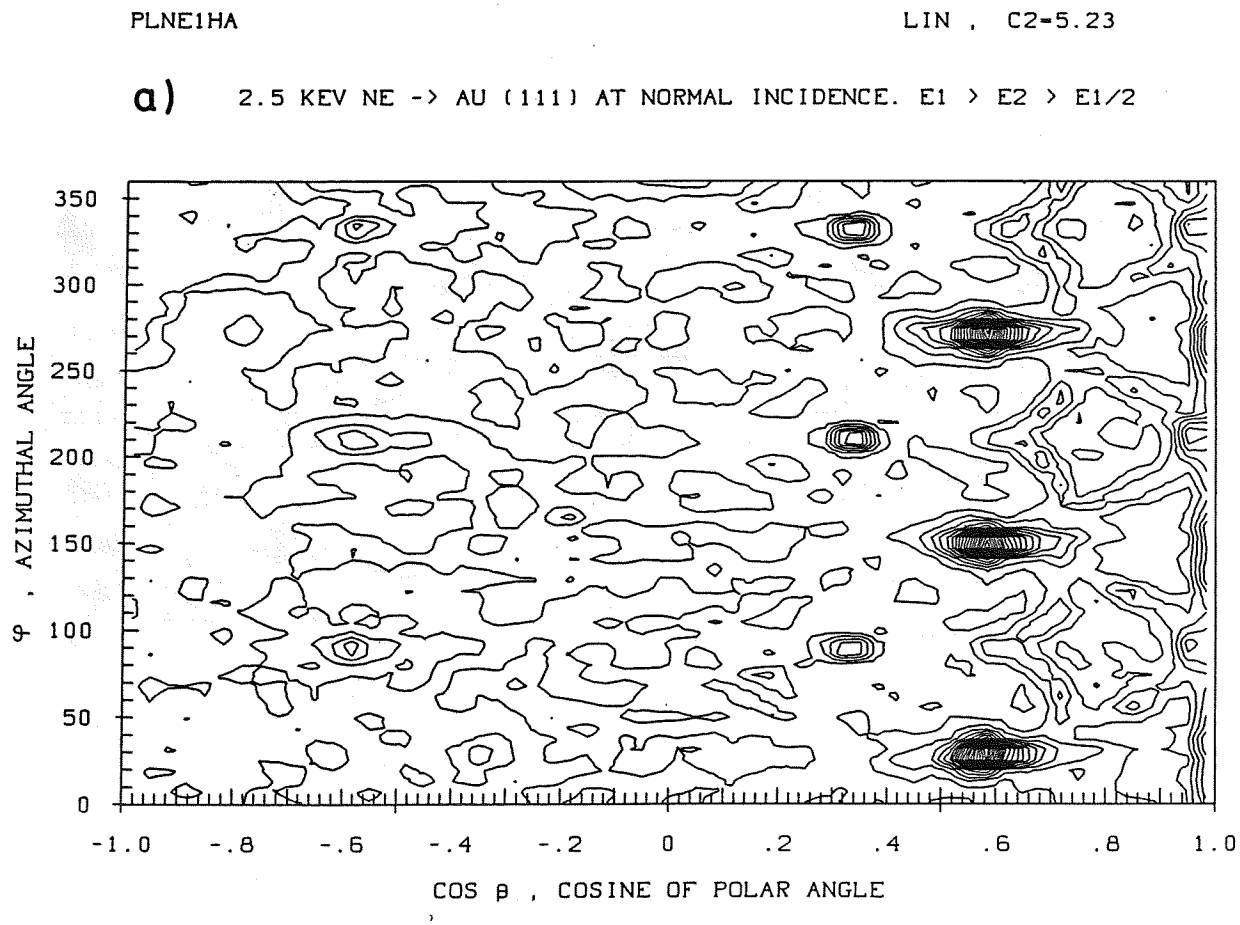
PLNE1HA
LIN , C2=5.23
a) 2.5 KEV NE -> AU (111) AT NORMAL INCIDENCE. E1 > E2 > E1/2
φ , AZIMUTHAL ANGLE
350
300
250
200
150
100
50
0
-1.0
-.8
-.6
-.4
-.2
0
.2
.4
.6
.8
1.0
COS β , COSINE OF POLAR ANGLE

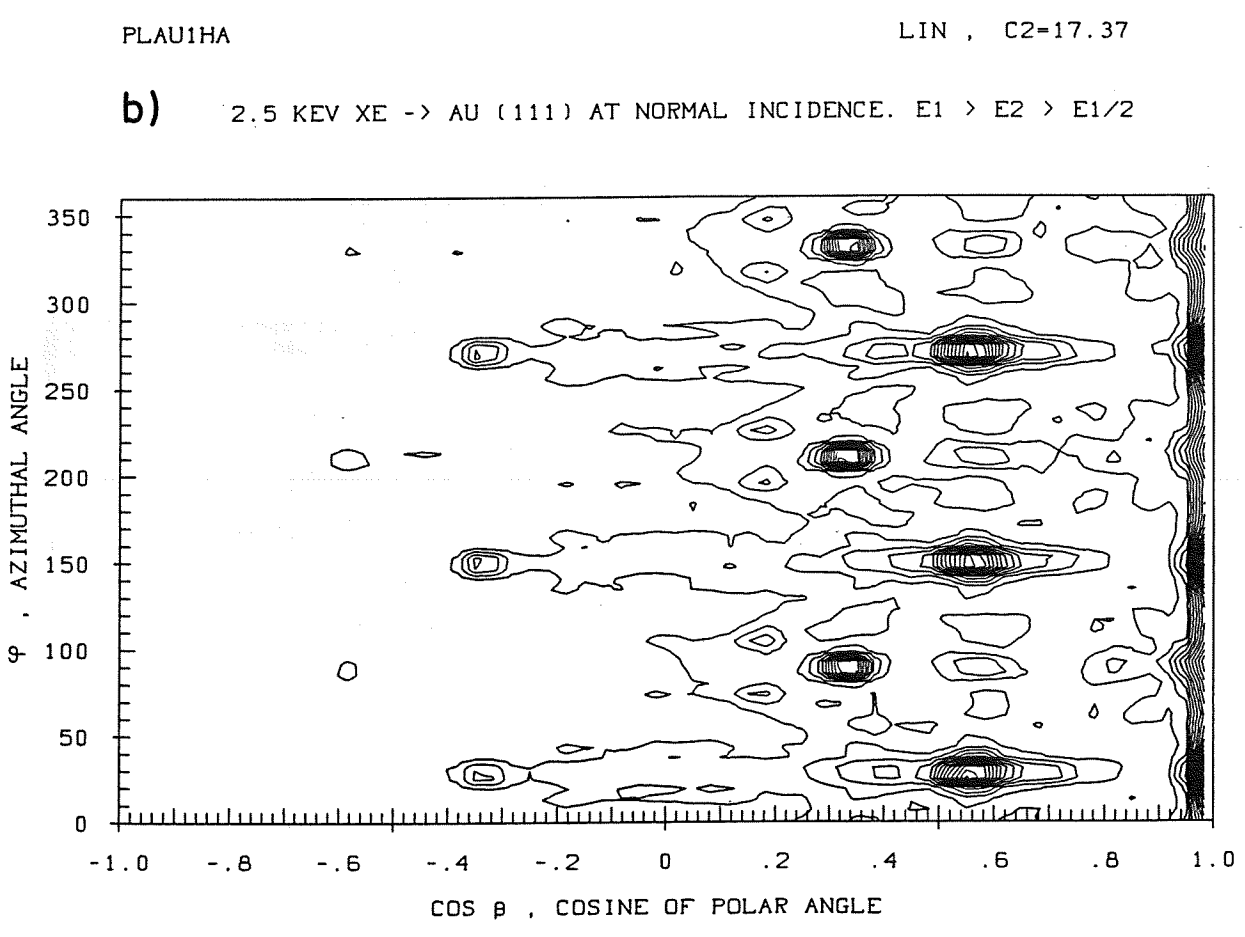
PLAU1HA
LIN , C2=17.37
b) 2.5 KEV XE -> AU (111) AT NORMAL INCIDENCE. E1 > E2 > E1/2
φ , AZIMUTHAL ANGLE
350
300
250
200
150
100
50
0
-1.0
-.8
-.6
-.4
-.2
0
.2
.4
.6
.8
1.0
COS β , COSINE OF POLAR ANGLE

Fig. 3a,b

PLNE1HA LIN , C2=15.21

a) 2.5 KEV NE -> AU (111) AT NORMAL INCIDENCE. E2 > E3 > E2/2

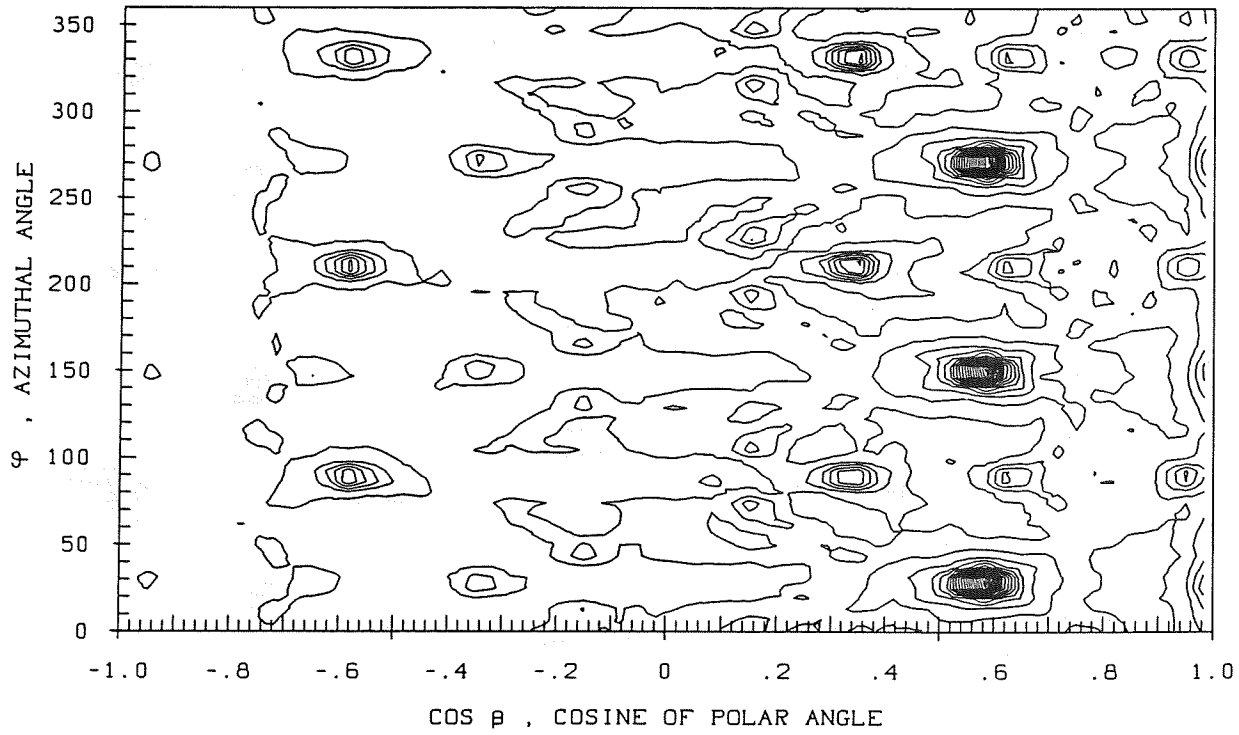

PLAU1HA LIN , C2=18.44

b) 2.5 KEV XE -> AU (111) AT NORMAL INCIDENCE. E2 > E3 > E2/2

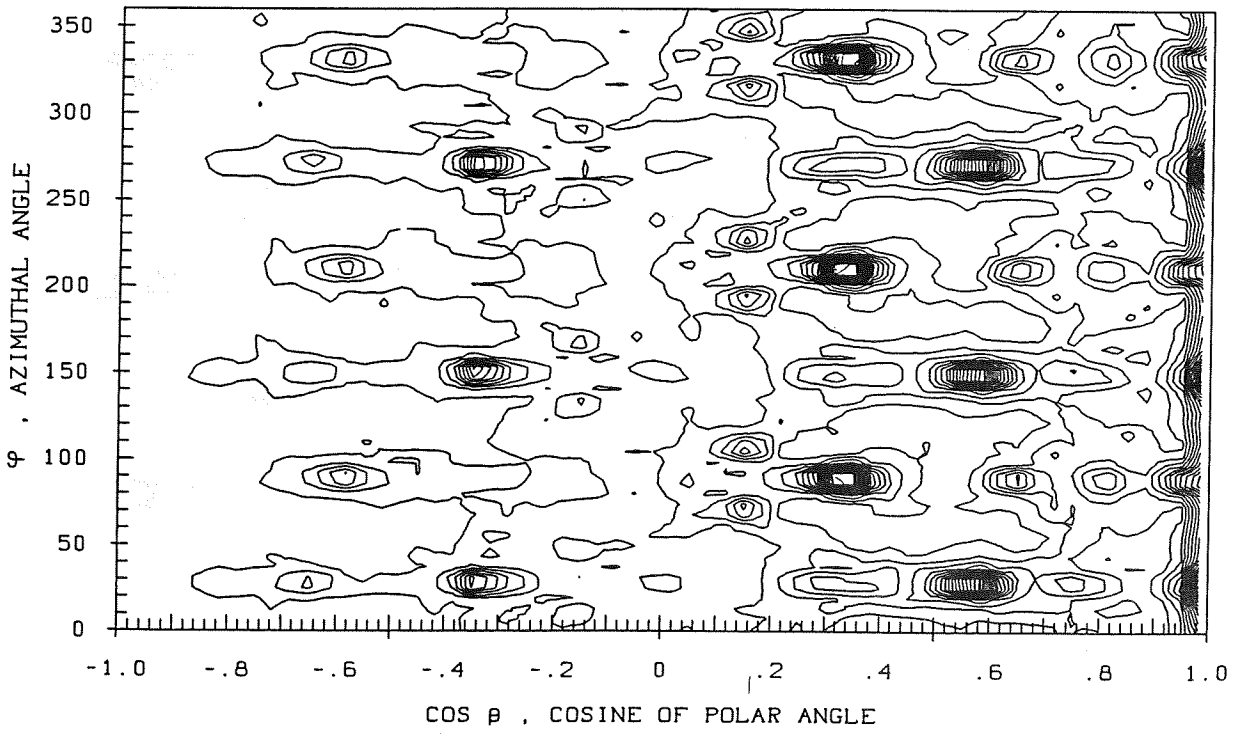

Fig. 4a,b

PLNE1HA LIN , C2=19.07

a) 2.5 KEV NE -> AU (111) AT NORMAL INCIDENCE. E3 > E4 > E3/2

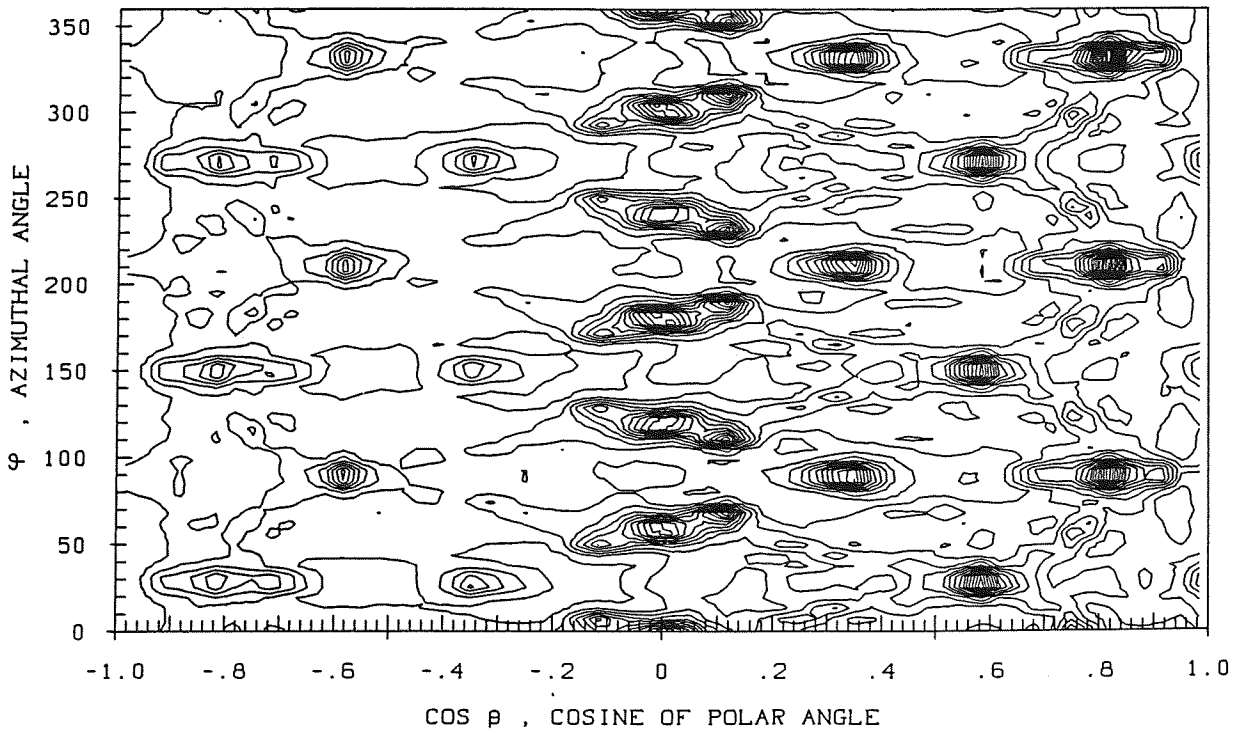

PLAU1HA LIN , C2=46.59

b) 2.5 KEV XE -> AU (111) AT NORMAL INCIDENCE. E3 > E4 > E3/2

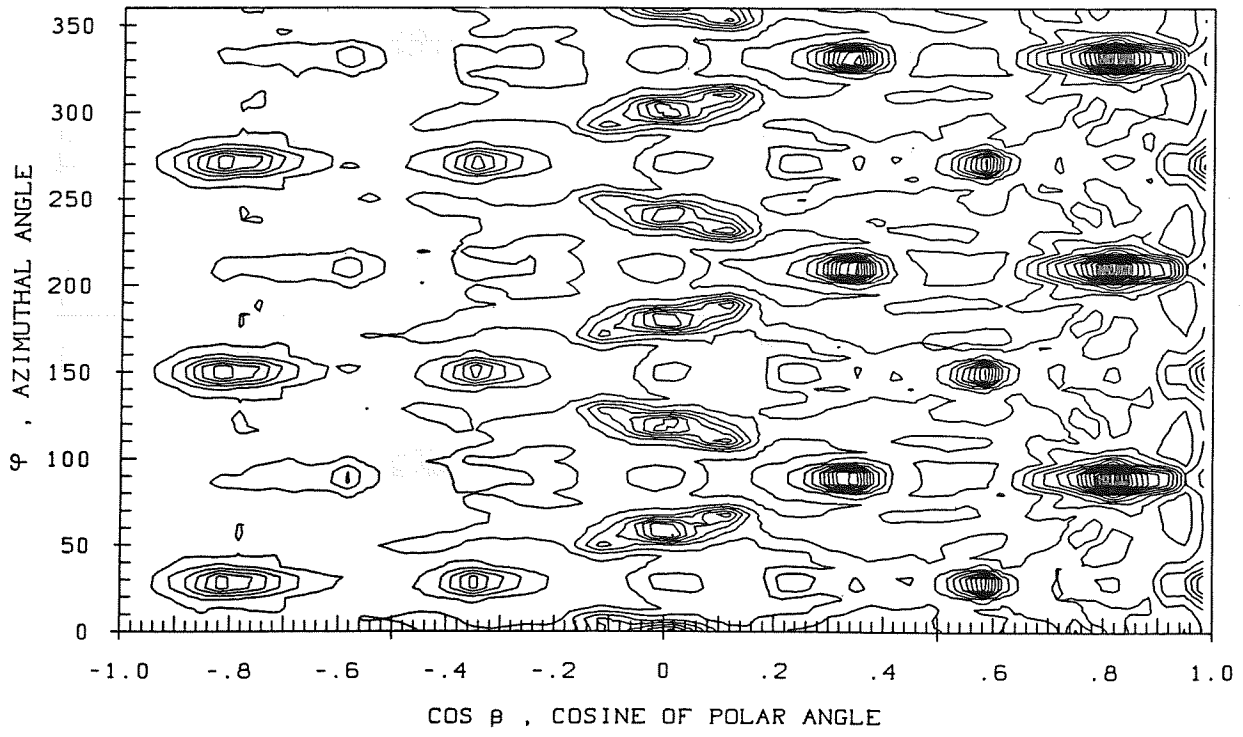

Fig. 5a,b

PLNE1HA LIN , C2=70.18

a) 2.5 KEV NE -> AU (111) AT NORMAL INCIDENCE. E4 > E5 > E4/2

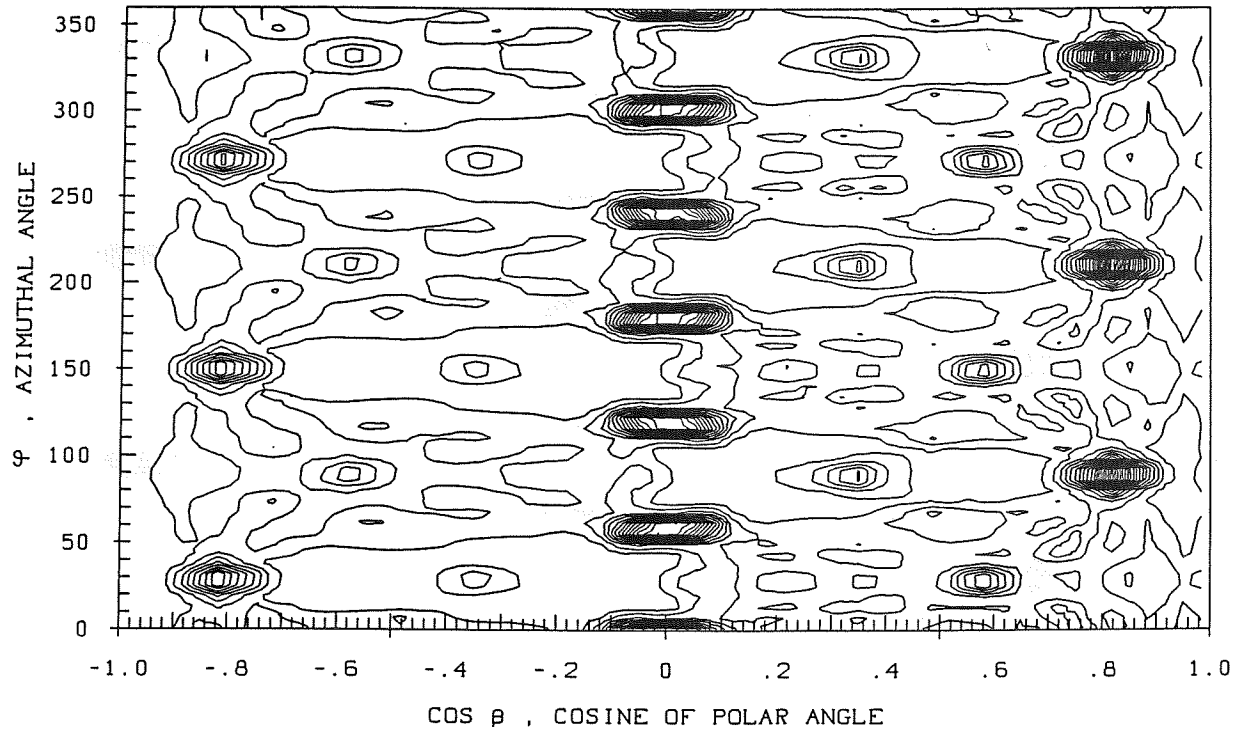

PLAU1HA LIN , C2=88.65

b) 2.5 KEV XE -> AU (111) AT NORMAL INCIDENCE. E4 > E5 > E4/2

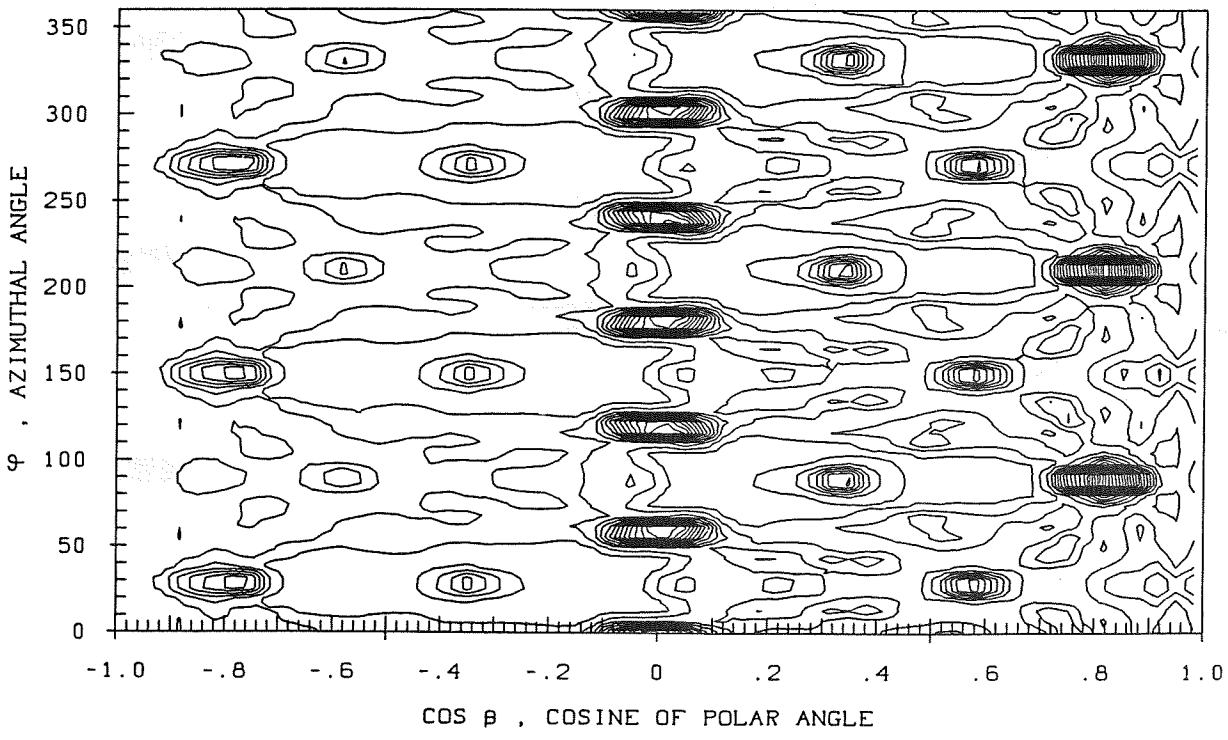

Fig. 6a,b

PLNE1HA LIN , C2=216.35

a) 2.5 KEV NE -> AU (111) AT NORMAL INCIDENCE. E5 > E6 > E5/2

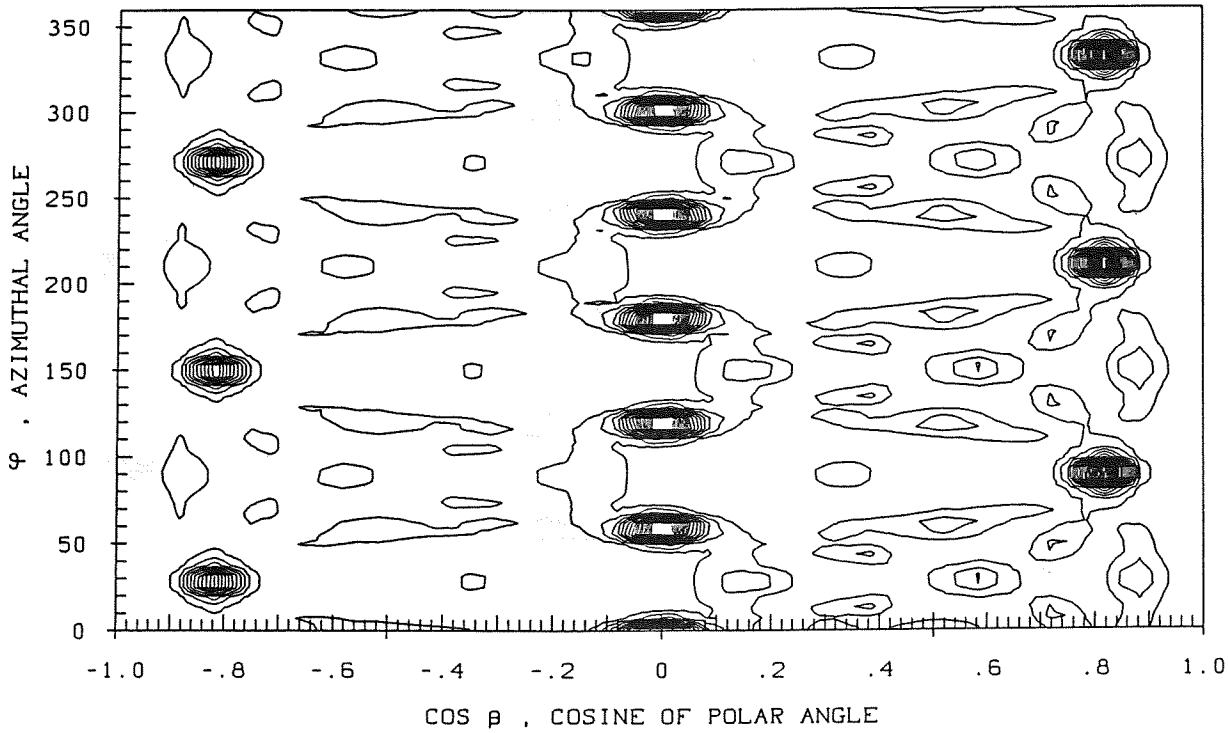

PLAU1HA LIN , C2=237.93

b) 2.5 KEV XE -> AU (111) AT NORMAL INCIDENCE. E5 > E6 > E5/2

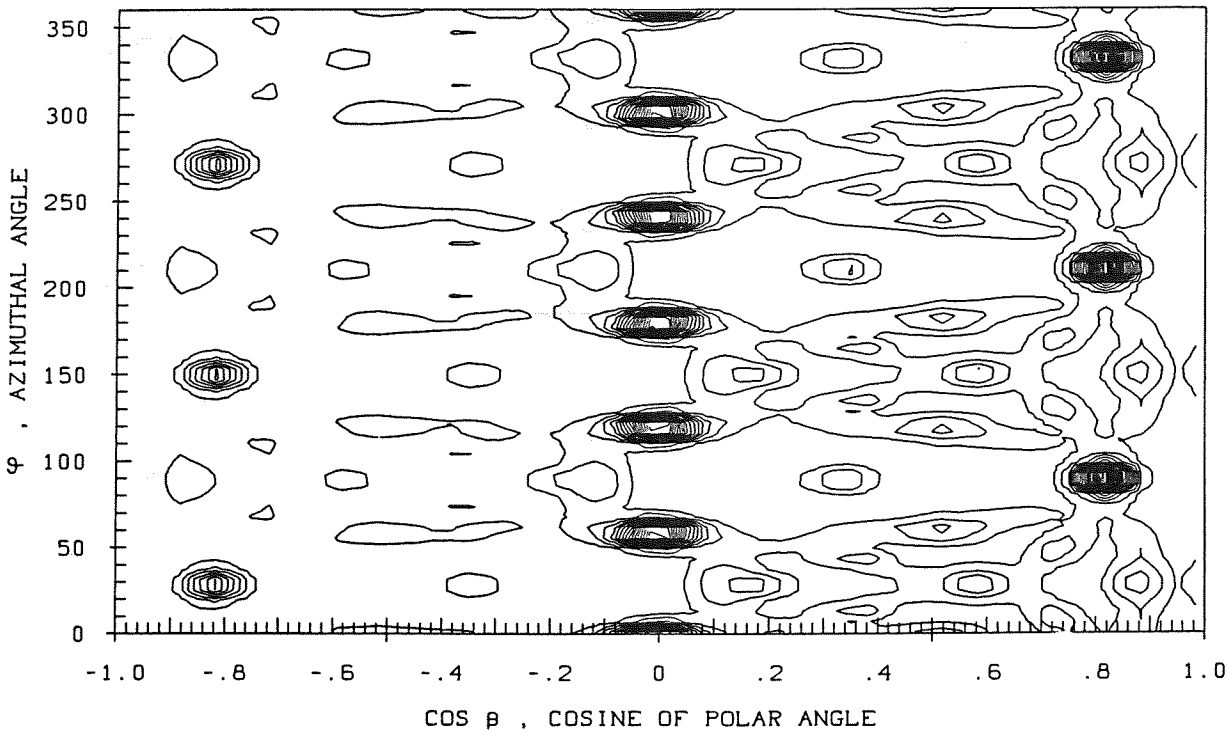

Fig. 7a,b

PLNE1HA LIN , C2=297.26

a) 2.5 KEV NE -> AU (111) AT NORMAL INCIDENCE. E6 > E7 > E6/2

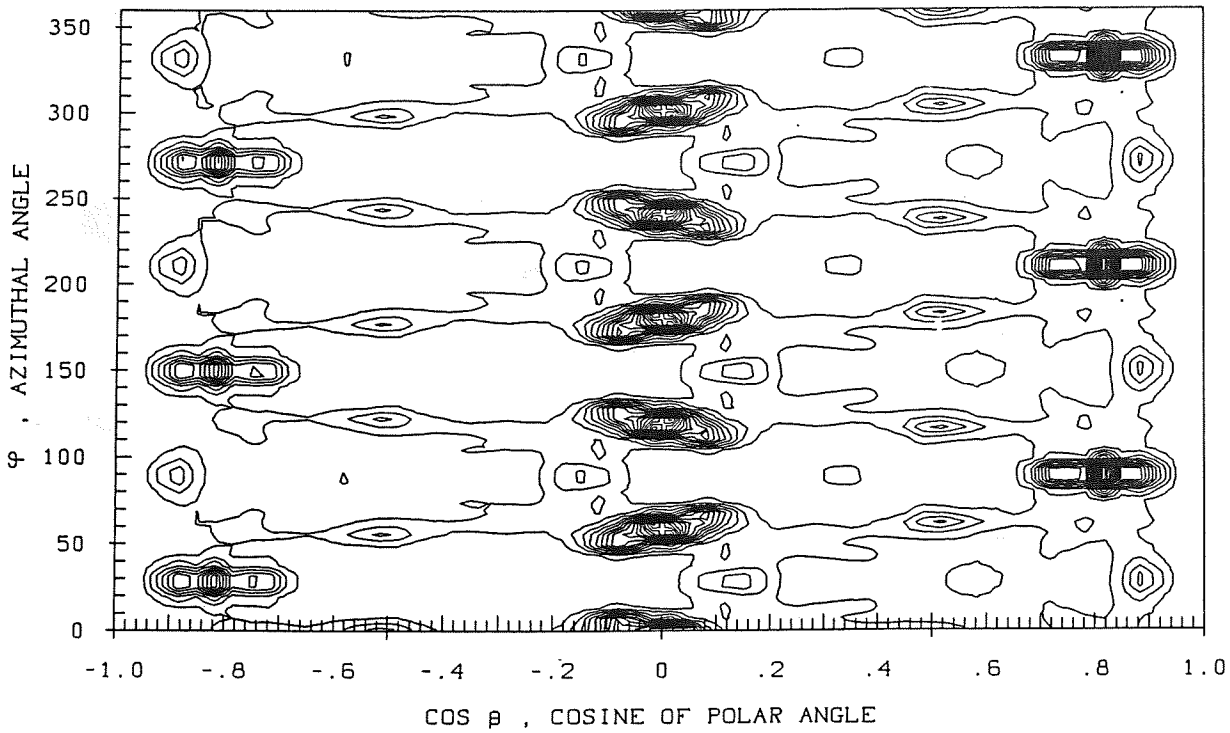

PLAU1HA LIN , C2=262.21

b) 2.5 KEV XE -> AU (111) AT NORMAL INCIDENCE. E6 > E7 > E6/2

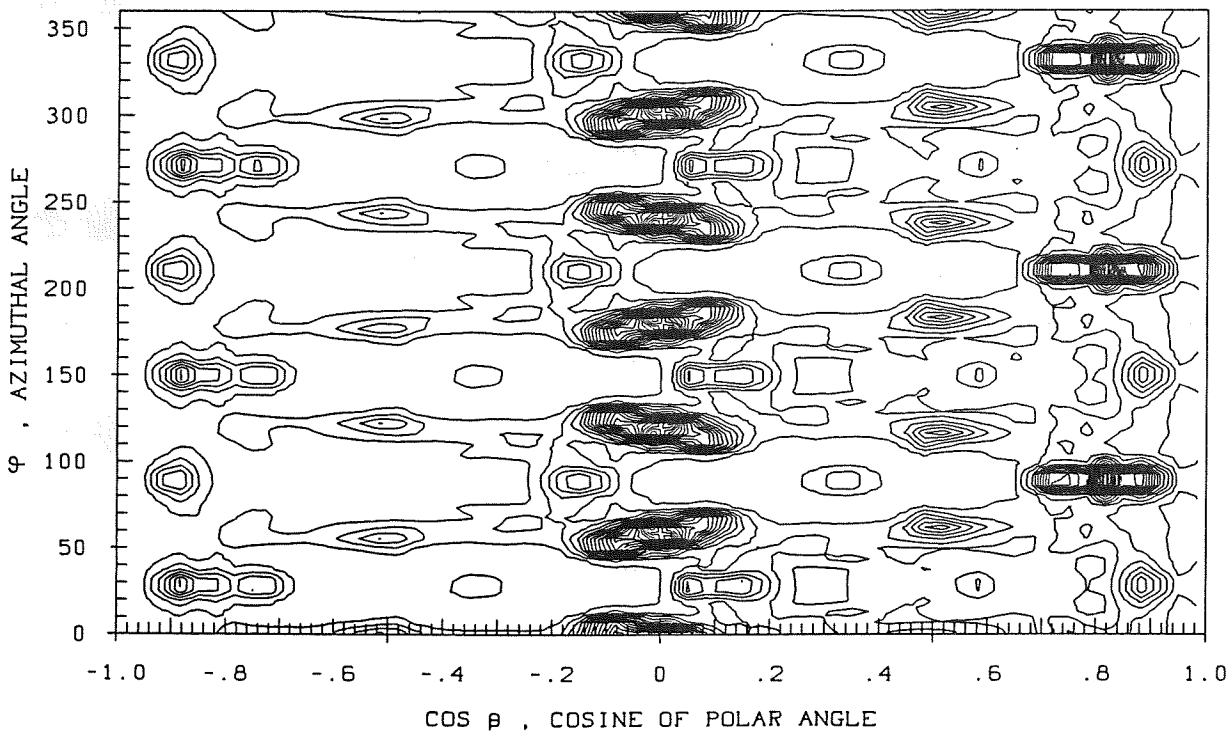

Fig. 3a,b

PLNE1HA LIN , C2=419.80

a) 2.5 KEV NE -> AU (111) AT NORMAL INCIDENCE. E7 > E8 > E7/2

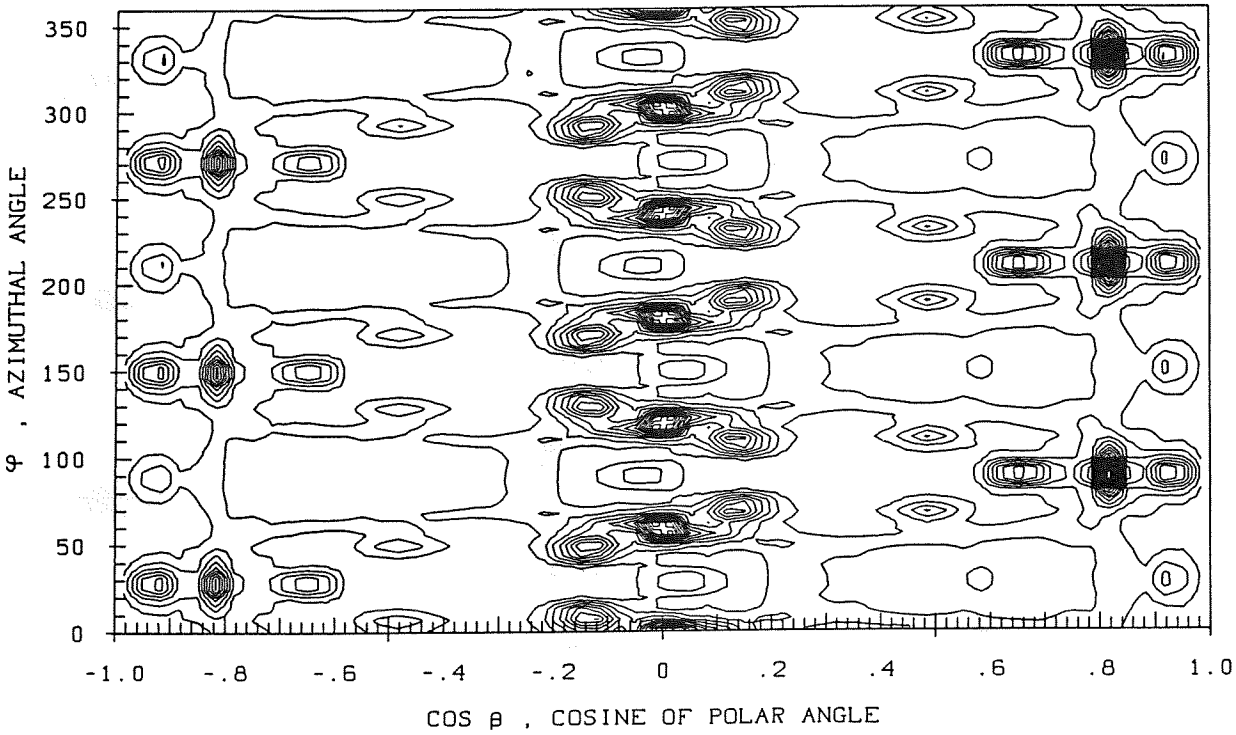

PLAU1HA LIN , C2=412.04

b) 2.5 KEV XE -> AU (111) AT NORMAL INCIDENCE. E7 > E8 > E7/2

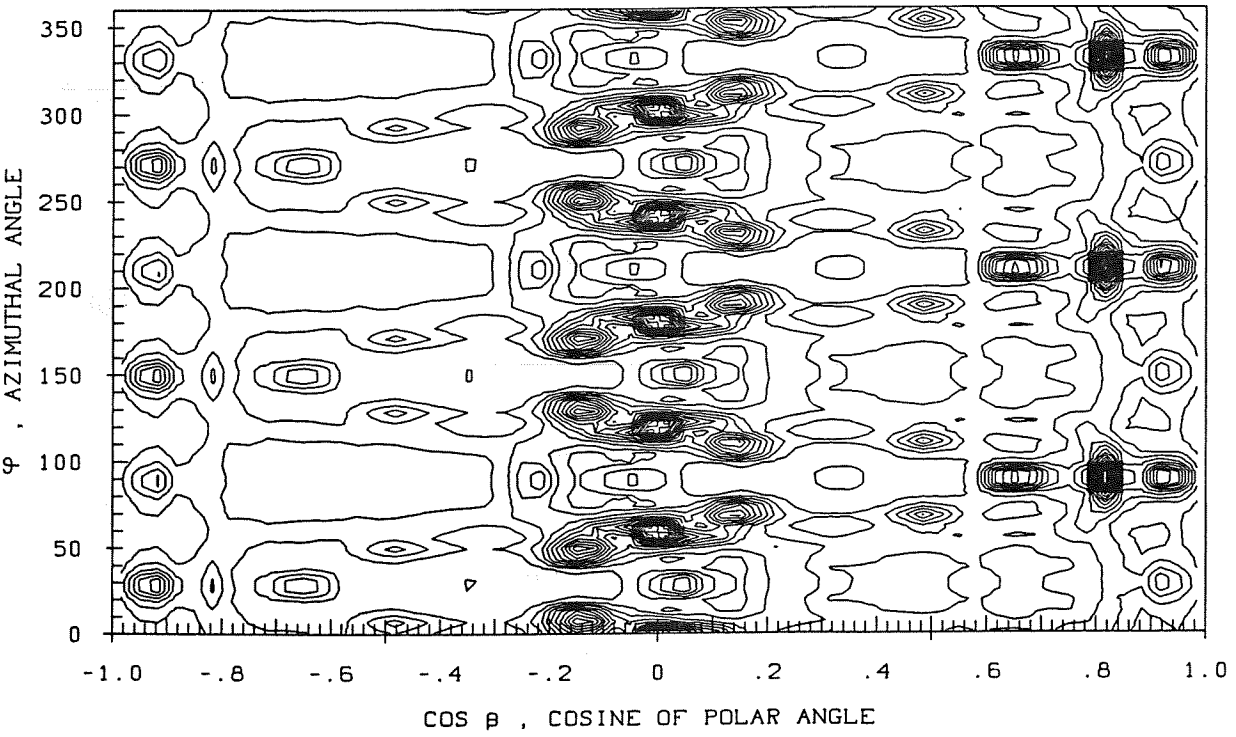

Fig. 9a,b

PLNE1HA LIN , C2=324.27

a) 2.5 KEV NE -> AU (111) AT NORMAL INCIDENCE. E8 > E9 > E8/2

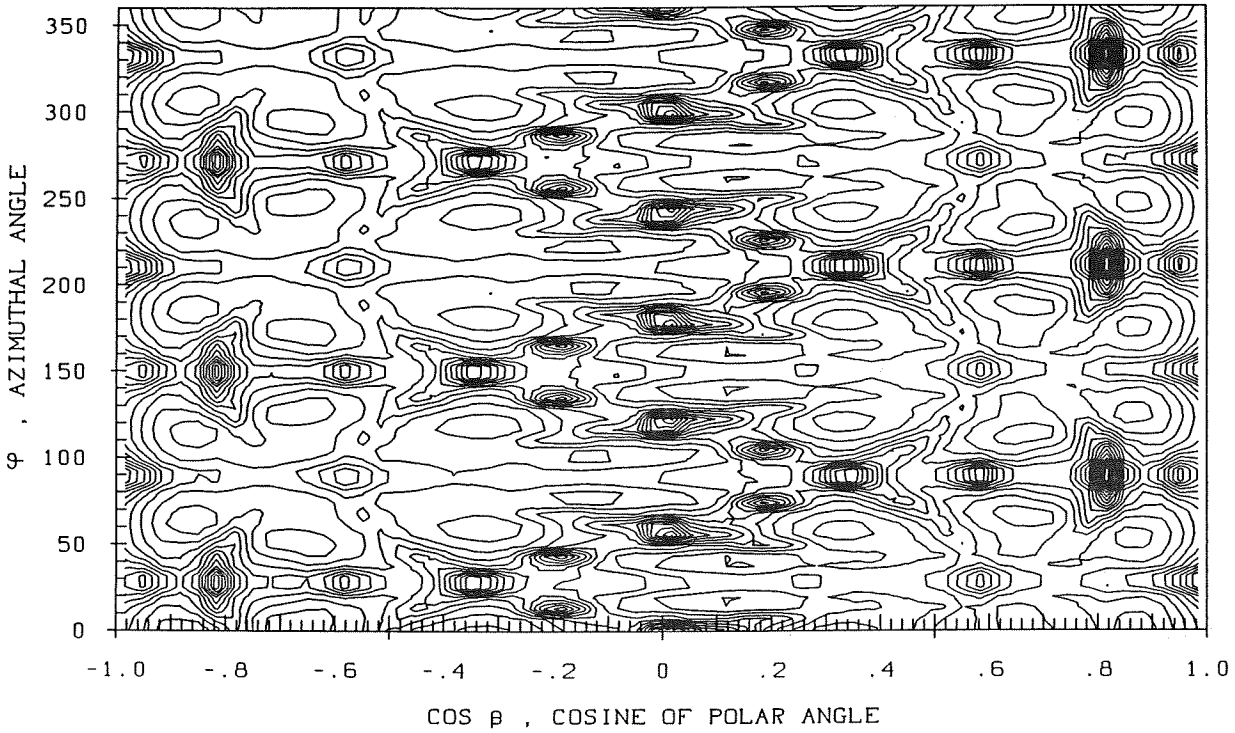

PLAU1HA LIN , C2=354.47

b) 2.5 KEV XE -> AU (111) AT NORMAL INCIDENCE. E8 > E9 > E8/2

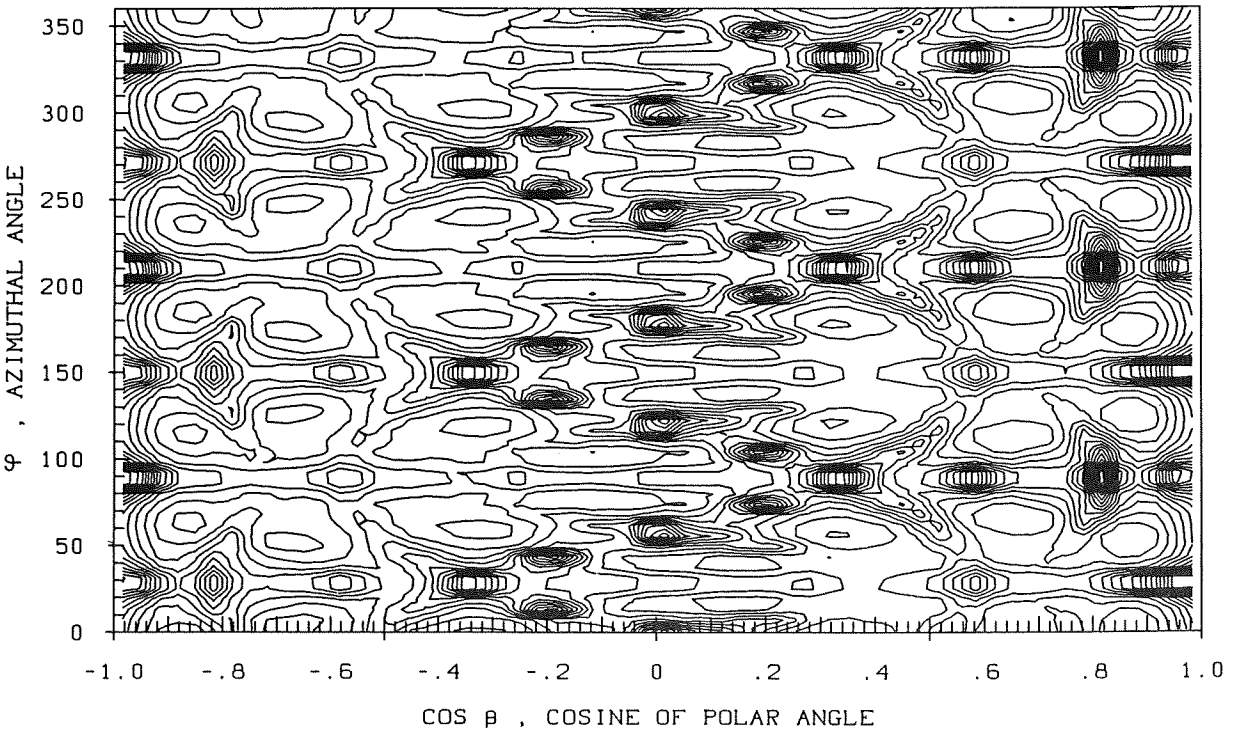

Fig. 10a,b

Figure 11

a) Loci of the directions parallel to the most compact crystallographic planes. Their intersections represent the close packed directions in the lattice, that are labelled in the figure. ΔΔΔ: loci of directions parallel to {100} planes, ooo: loci of directions parallel to {110} planes, +++: loci of the directions parallel to the {111} planes, ■ : <100> directions, ●: <110> directions, ◆ <111> directions, ▲: <112> directions and ▼: <221> directions.

b) Figure 11a is superimposed to a contour plot in order to illustrate how the latter can be analyzed in details. The focusing in close packed directions can be noticed, as well as in open directions. These are easily identified as close to <221> directions. The two-dimensional focusing parallel to {110} planes is visible too.

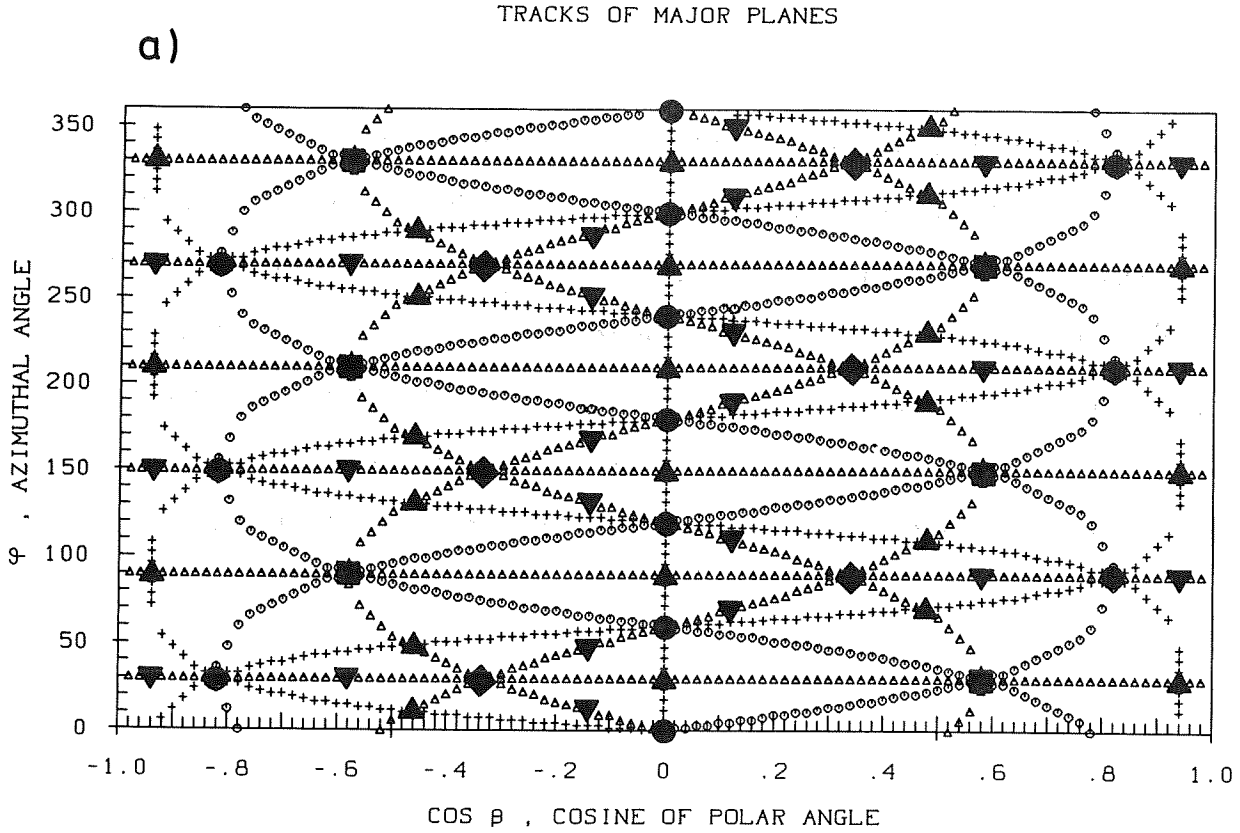

PLNE1HA TRACKS OF MAJOR PLANES LIN , C2-419.80

2.5 KEV XE -> AU (111) AT NORMAL INCIDENCE. E7 > E8 > E7/2

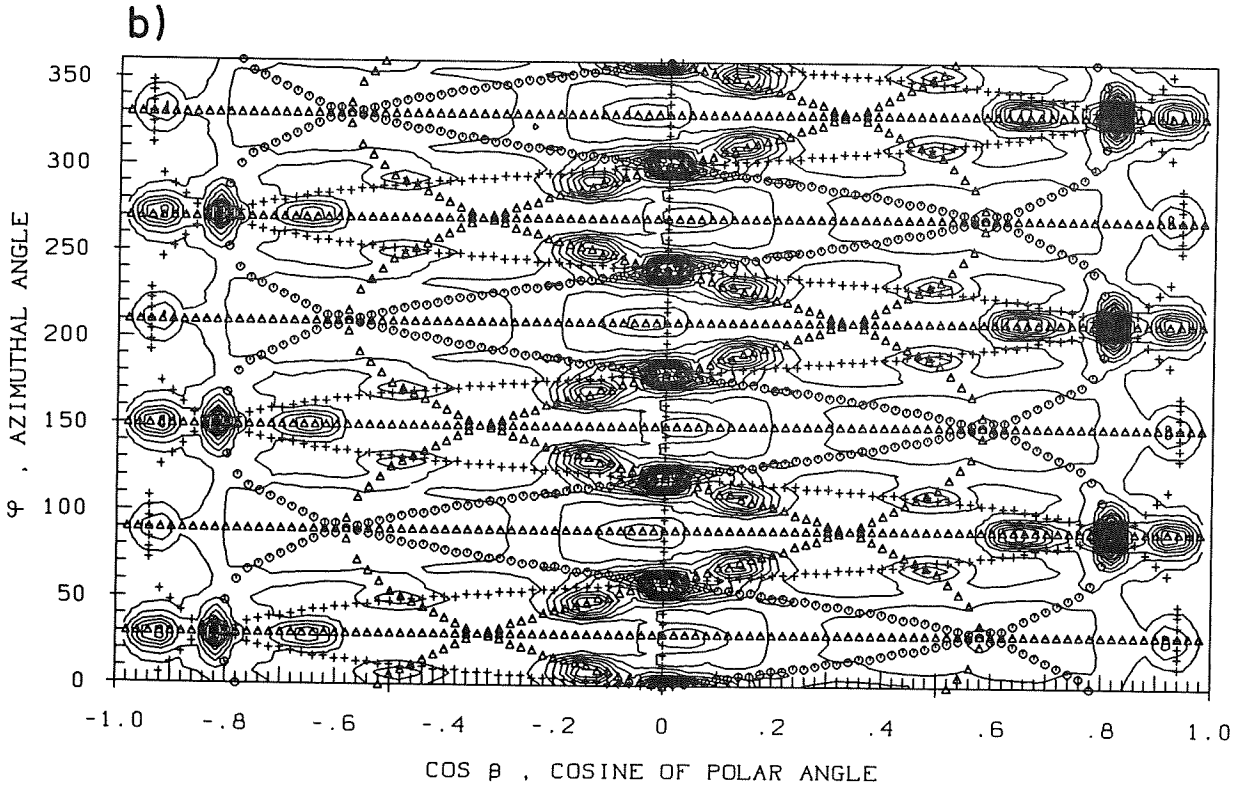

Fig. 11a,b

Figure 12

Ratio of the number of moving recoil atoms generated by 2.5 keV Ne and Xe atoms as a function of the motion energy. Each channel in the histogram concerns atoms whose energy gets lower than $E_0/2^n$ but remains larger than $E_0/2^{n+1}$, where E_0 = 2.5 kev is the projectile energy. Owing to the difference in the inelastic energy lost by Ne and Xe atoms, the ratios of energy available for damage is 0.79, which is quite close to the ratio of the number of moving atoms with energies lower than 39 eV (n=6).

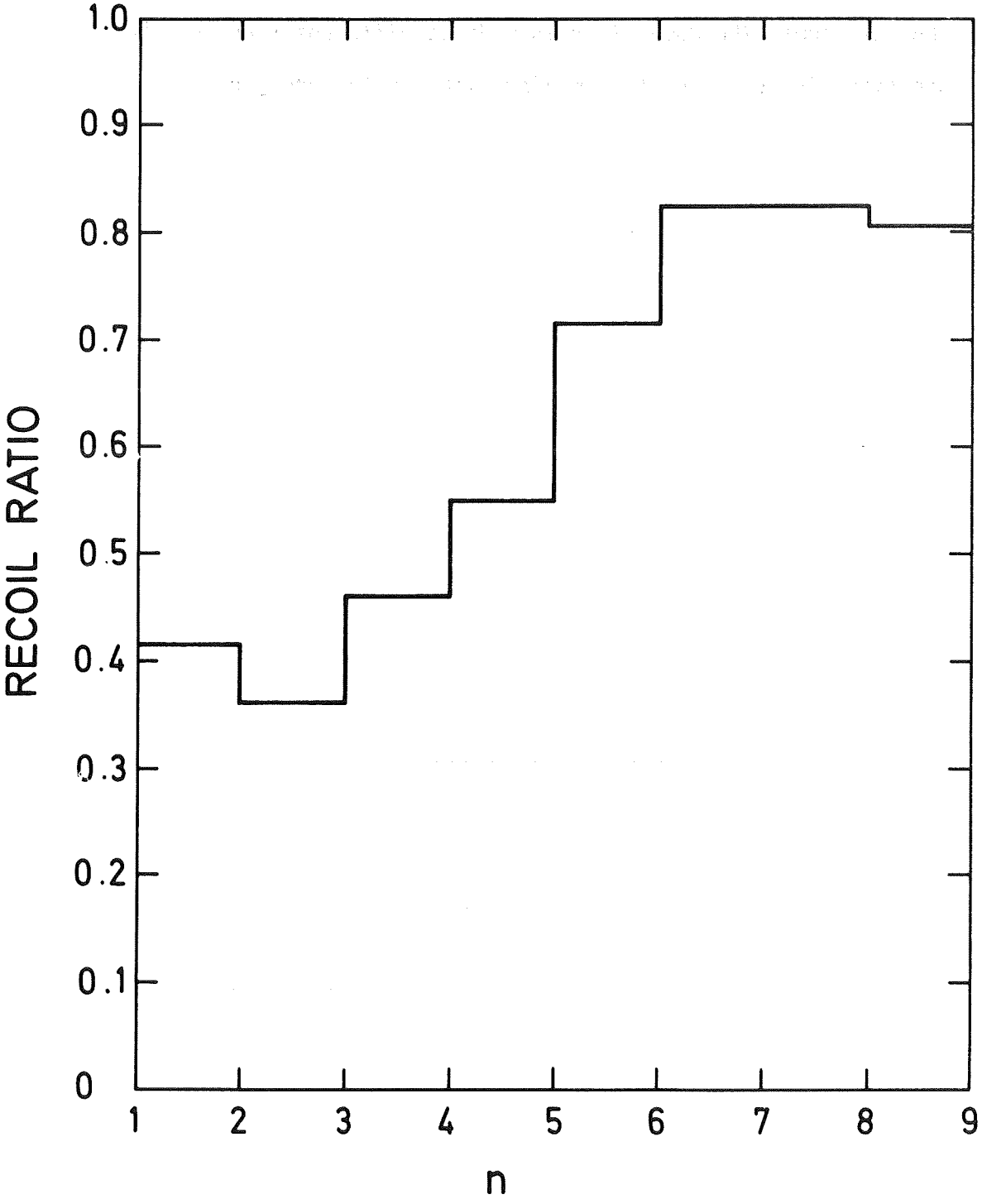

Fig. 12

Figures 13 to 18

Contour line plots representing the direction distributions of moving atoms in the cascades generated by 600 eV (fig. 13 to 18a) and 2.5 keV (fig. 13 to 18b) Xe atoms. The comparison is made at different steps of the energy dissipation, for cascade atoms moving with similar energies.

PLFL111 LIN , C2=40.33

a) 600 EV XE -> AU (111) AT NORMAL INCIDENCE. E0/2 > E1 > E0/4.

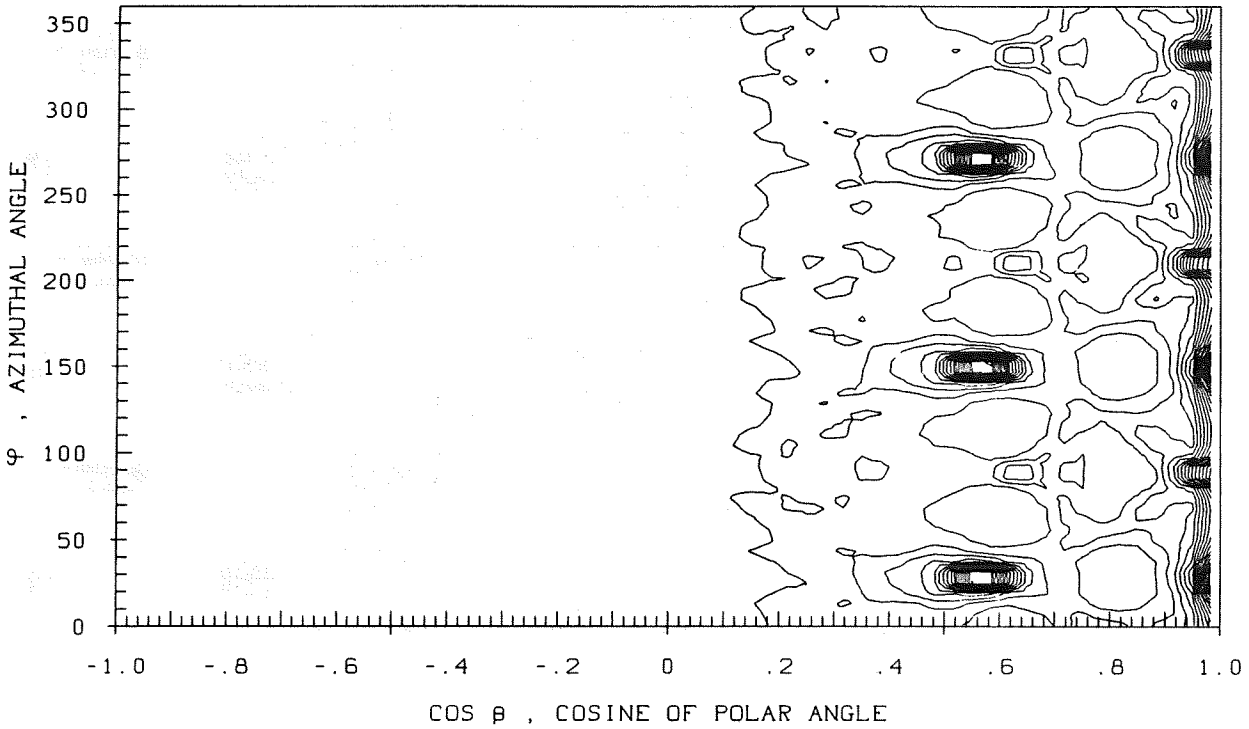

PLAU1HA LIN , C2=18.44

b) 2.5 KEV XE -> AU (111) AT NORMAL INCIDENCE. E2 > E3 > E2/2

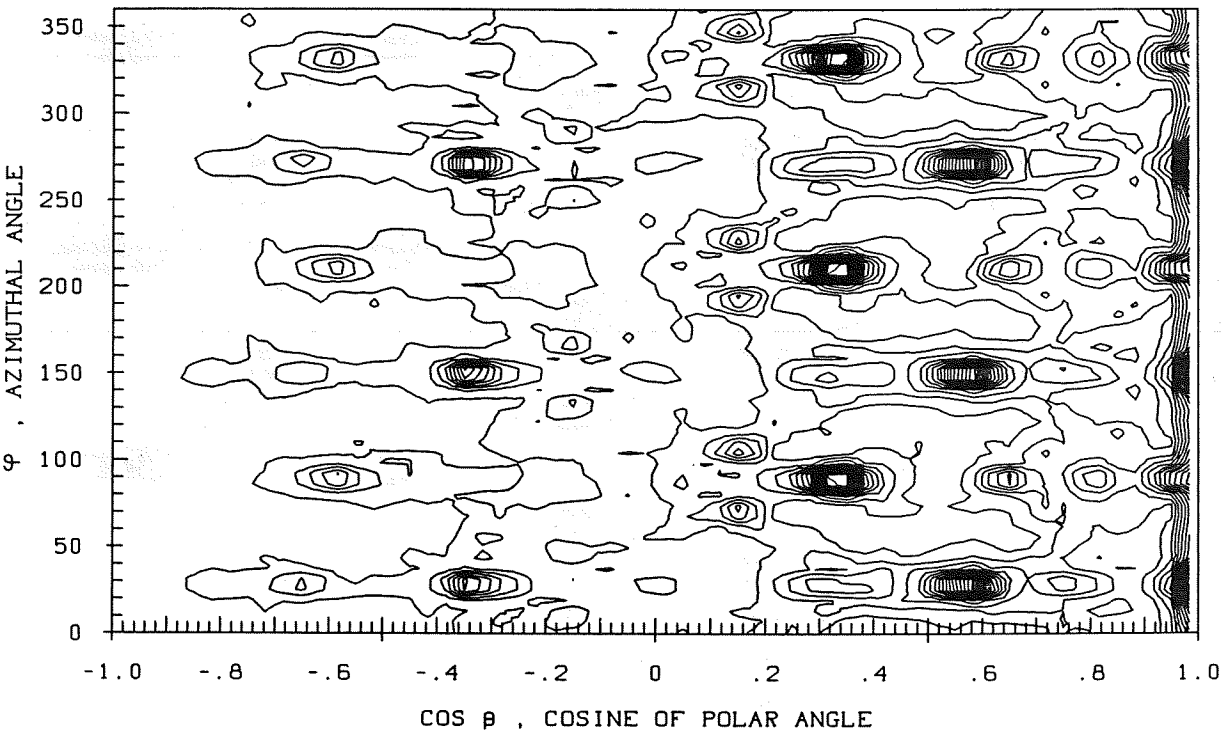

Fig. 13a,b

PLFL111 LIN , C2=47.26

a) 600 EV XE -> AU (111) AT NORMAL INCIDENCE. E1 > E2 > E1/2

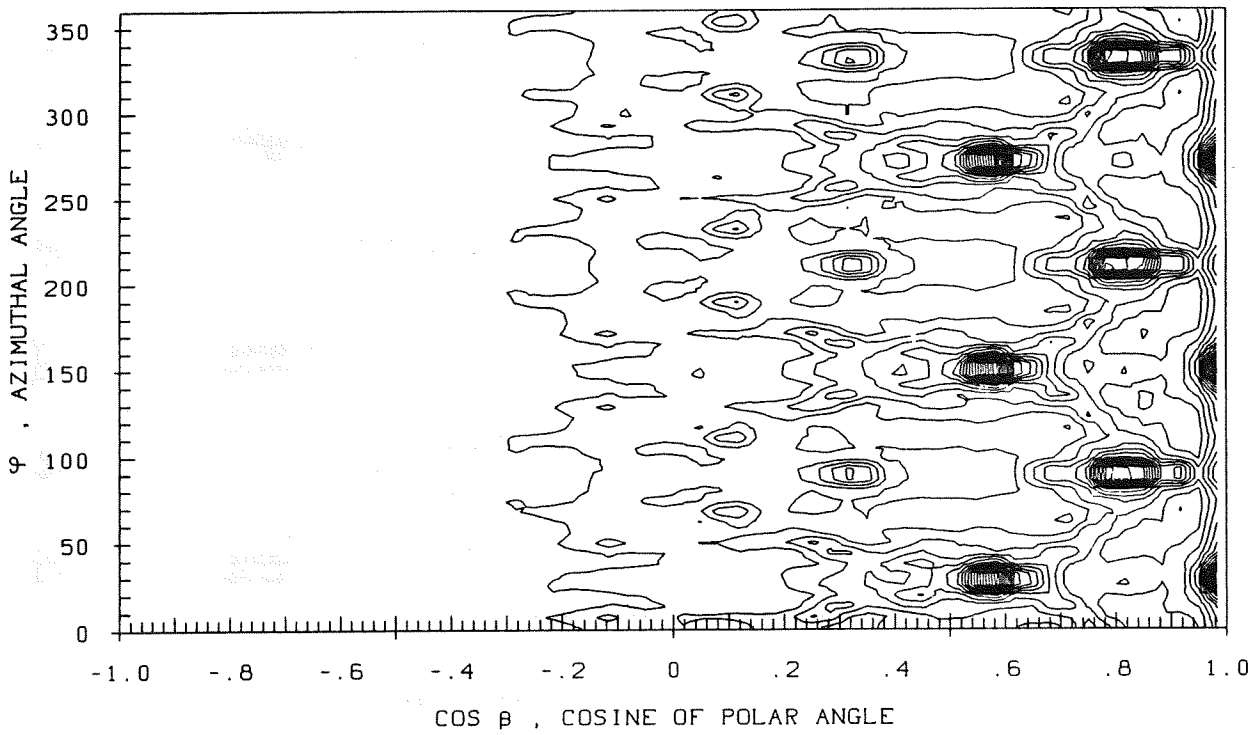

PLAU1HA LIN , C2=46.59

b) 2.5 KEV XE -> AU (111) AT NORMAL INCIDENCE. E3 > E4 > E3/2

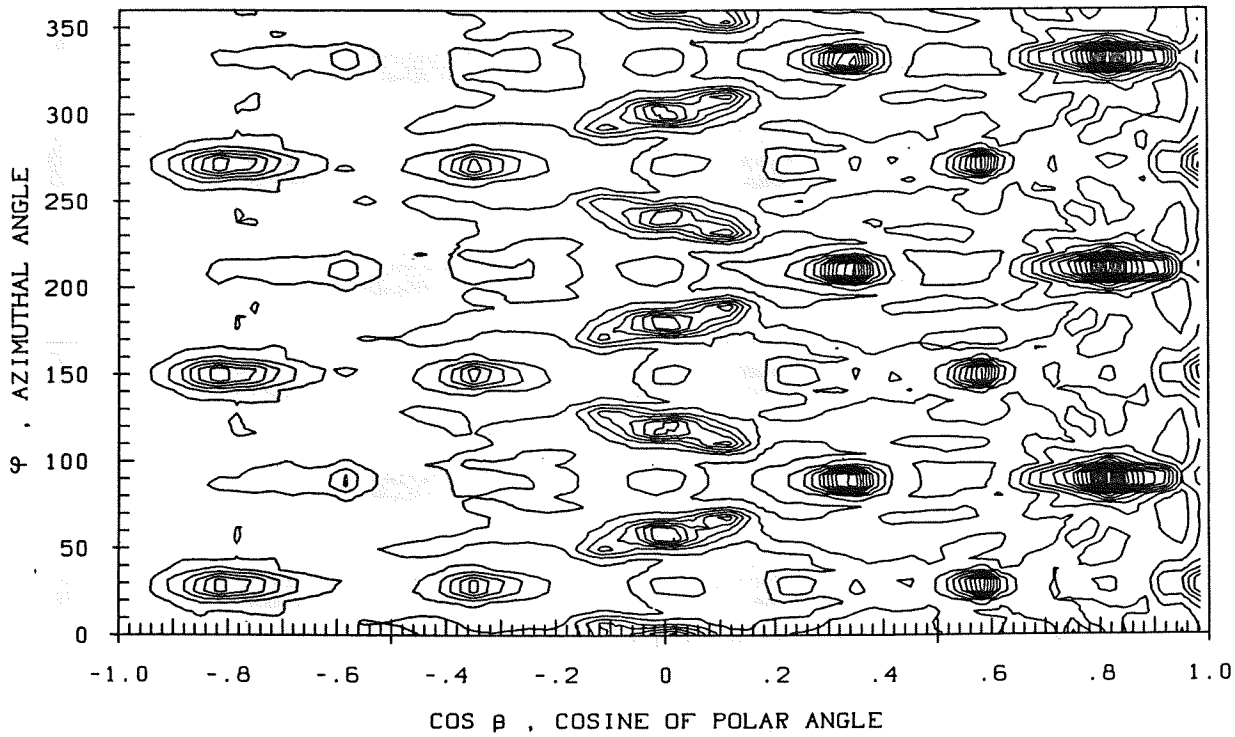

Fig. 14a,b

PLFL111 LIN , C2=68.07

a) 600 EV XE -> AU (111) AT NORMAL INCIDENCE. E2 > E3 > E2/2

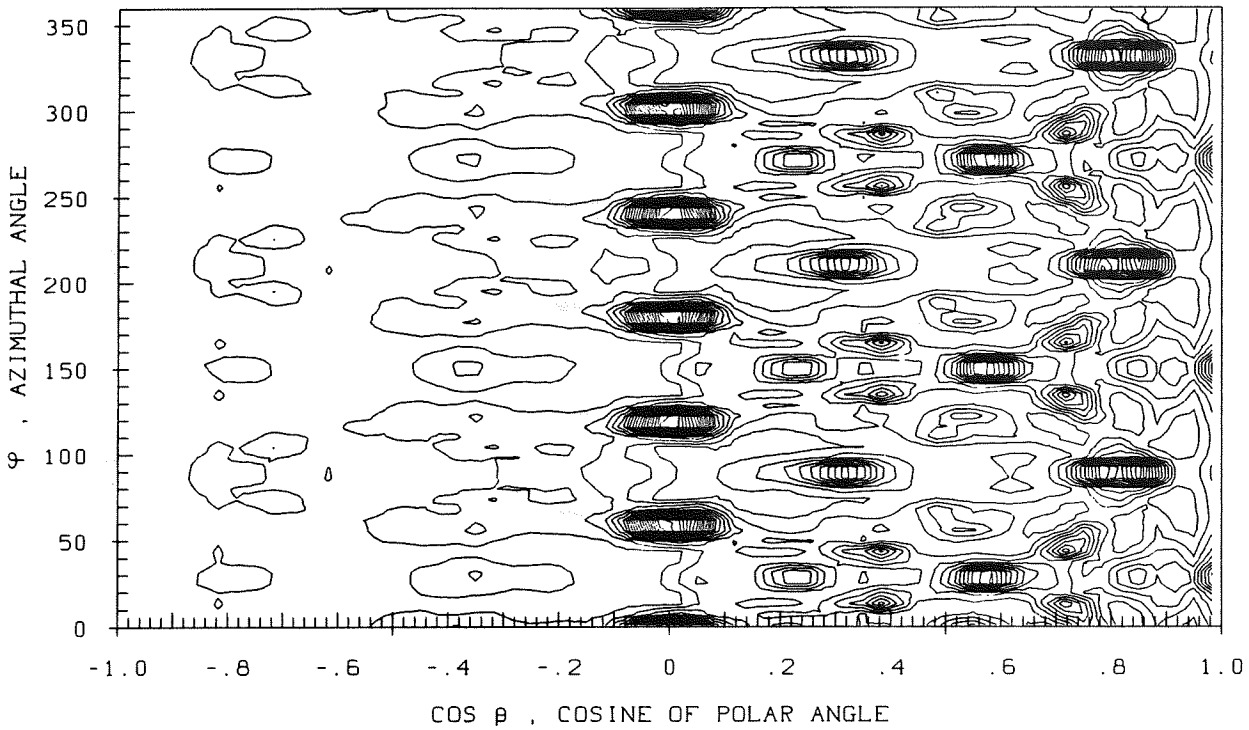

PLAU1HA LIN , C2=88.65

b) 2.5 KEV XE -> AU (111) AT NORMAL INCIDENCE. E4 > E5 > E4/2

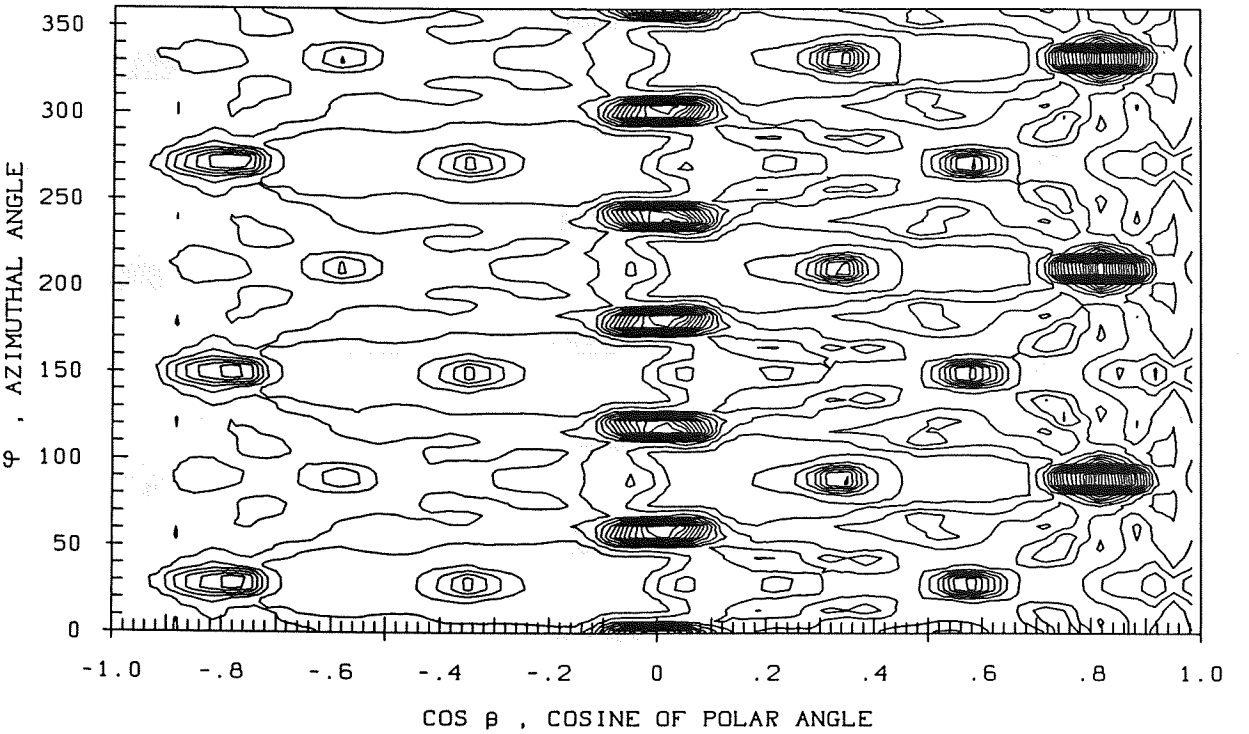

Fig. 15a,b

PLFL111 LIN , C2=232.12

a) 600 EV XE -> AU (111) AT NORMAL INCIDENCE. E3 > E4 > E3/2

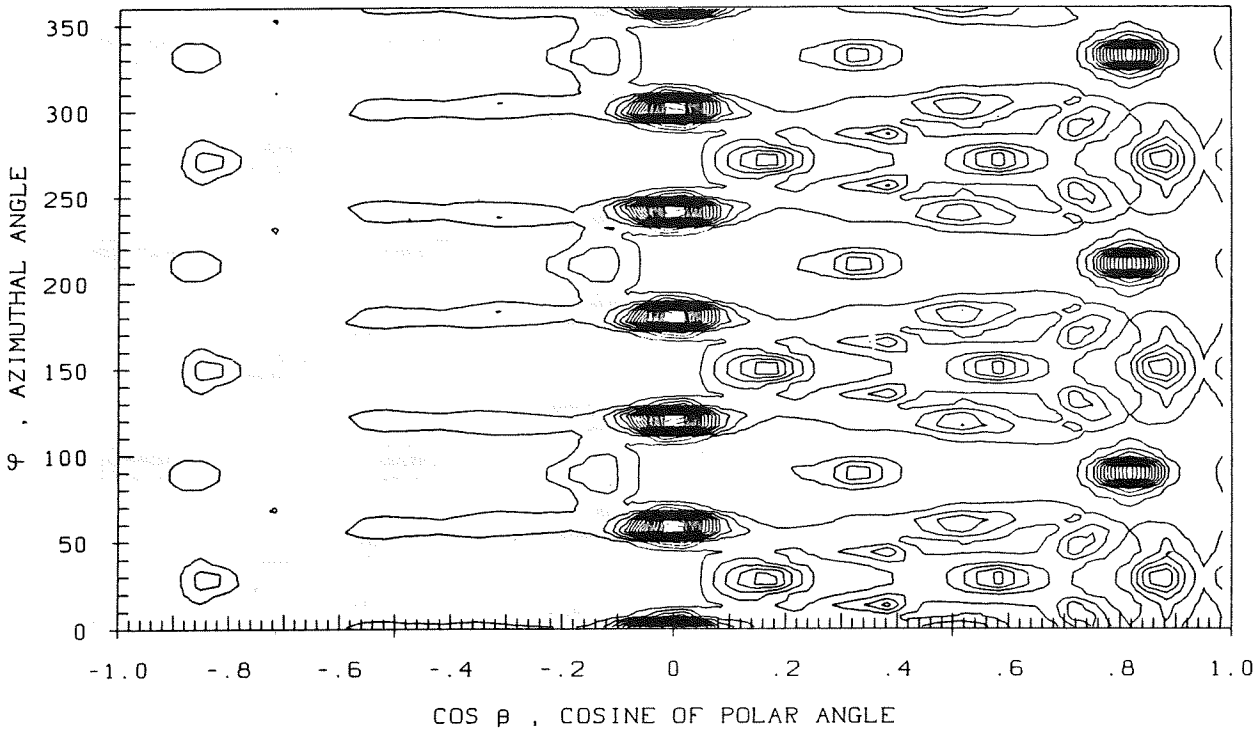

PLAU1HA LIN , C2=237.93

b) 2.5 KEV XE -> AU (111) AT NORMAL INCIDENCE. E5 > E6 > E5/2

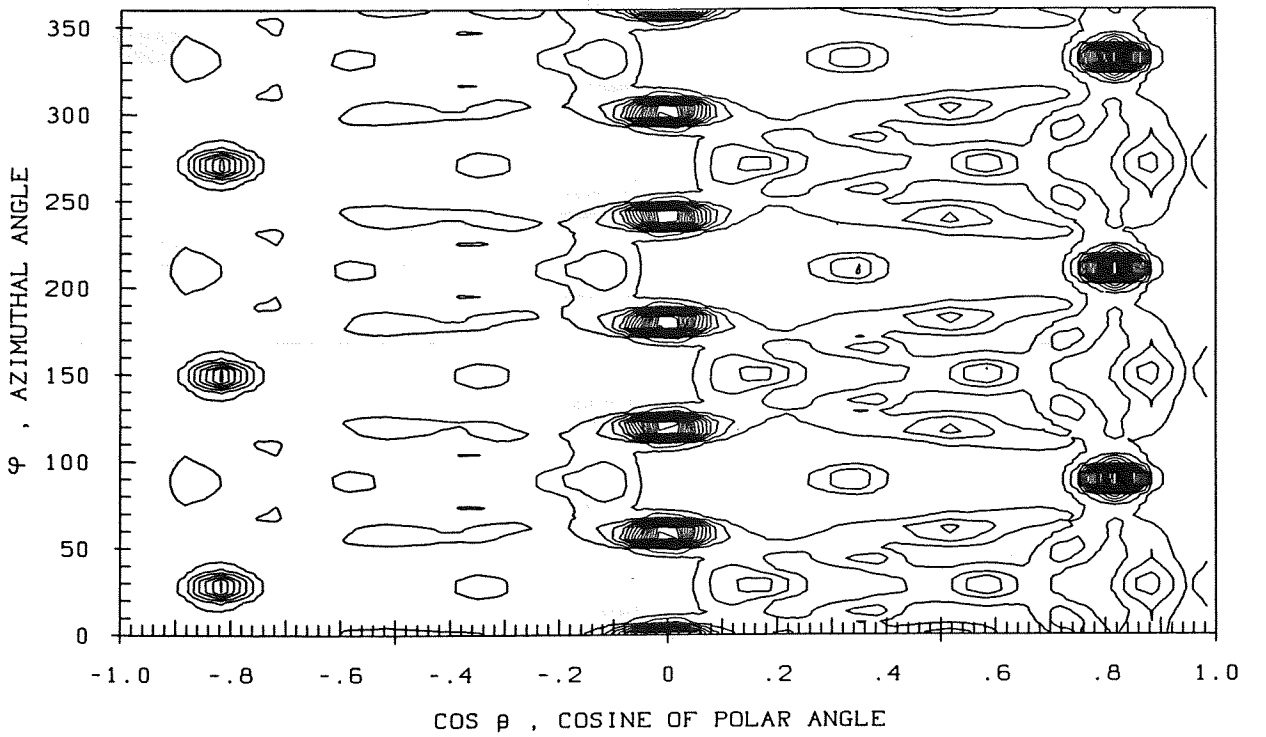

Fig. 16a,b

PLFL111 LIN , C2=311.86

a) 600 EV XE -> AU (111) AT NORMAL INCIDENCE. E4 > E5 > E4/2

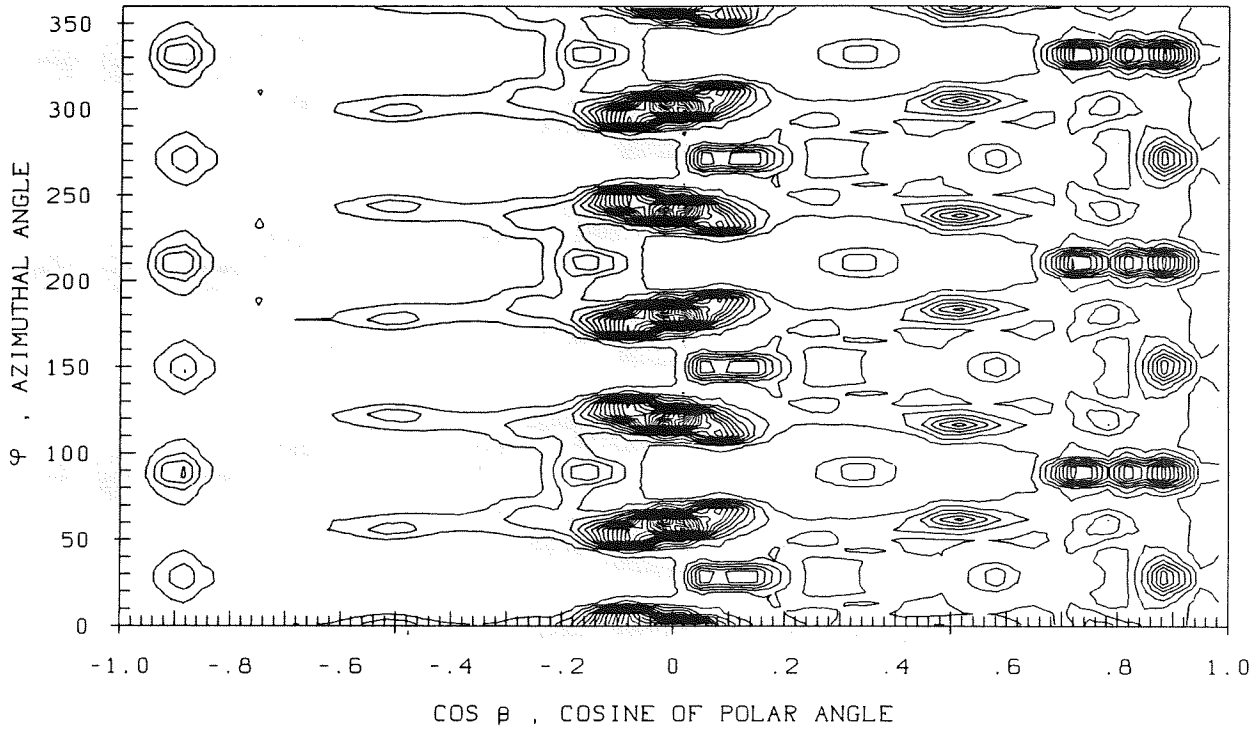

PLAU1HA LIN , C2=262.21

b) 2.5 KEV XE -> AU (111) AT NORMAL INCIDENCE. E6 > E7 > E6/2

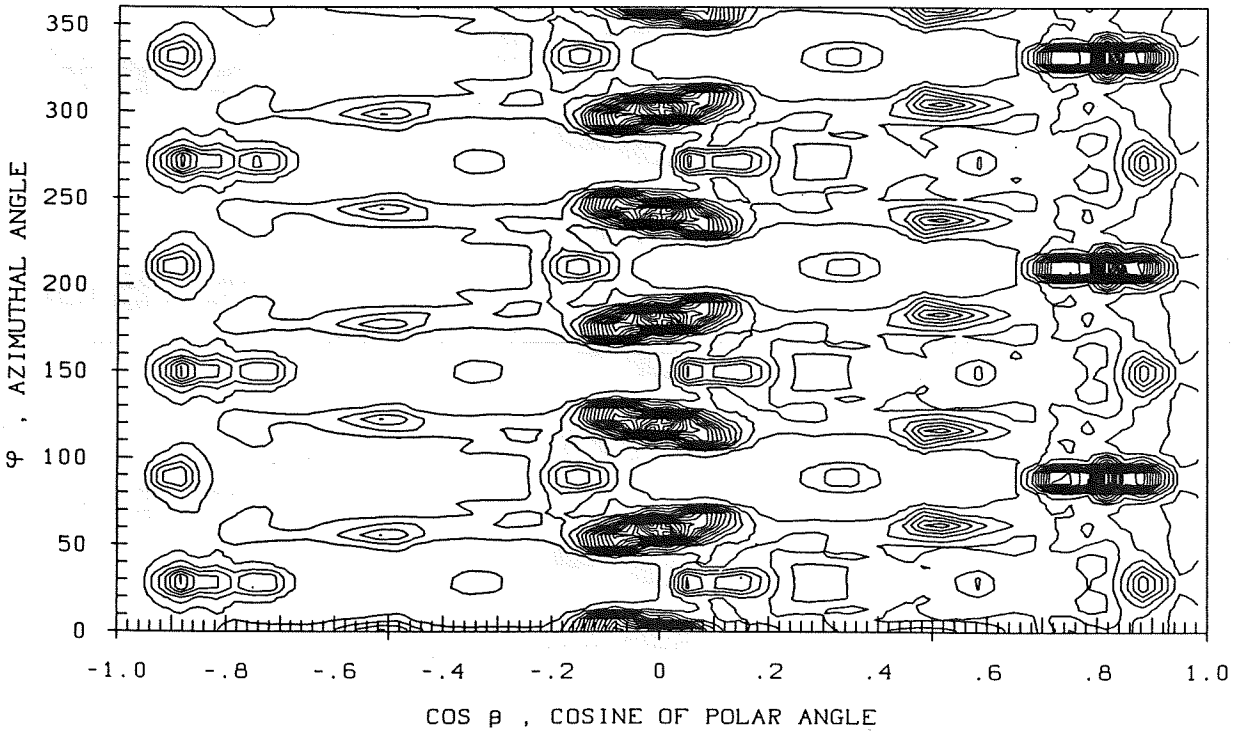

Fig. 17a,b

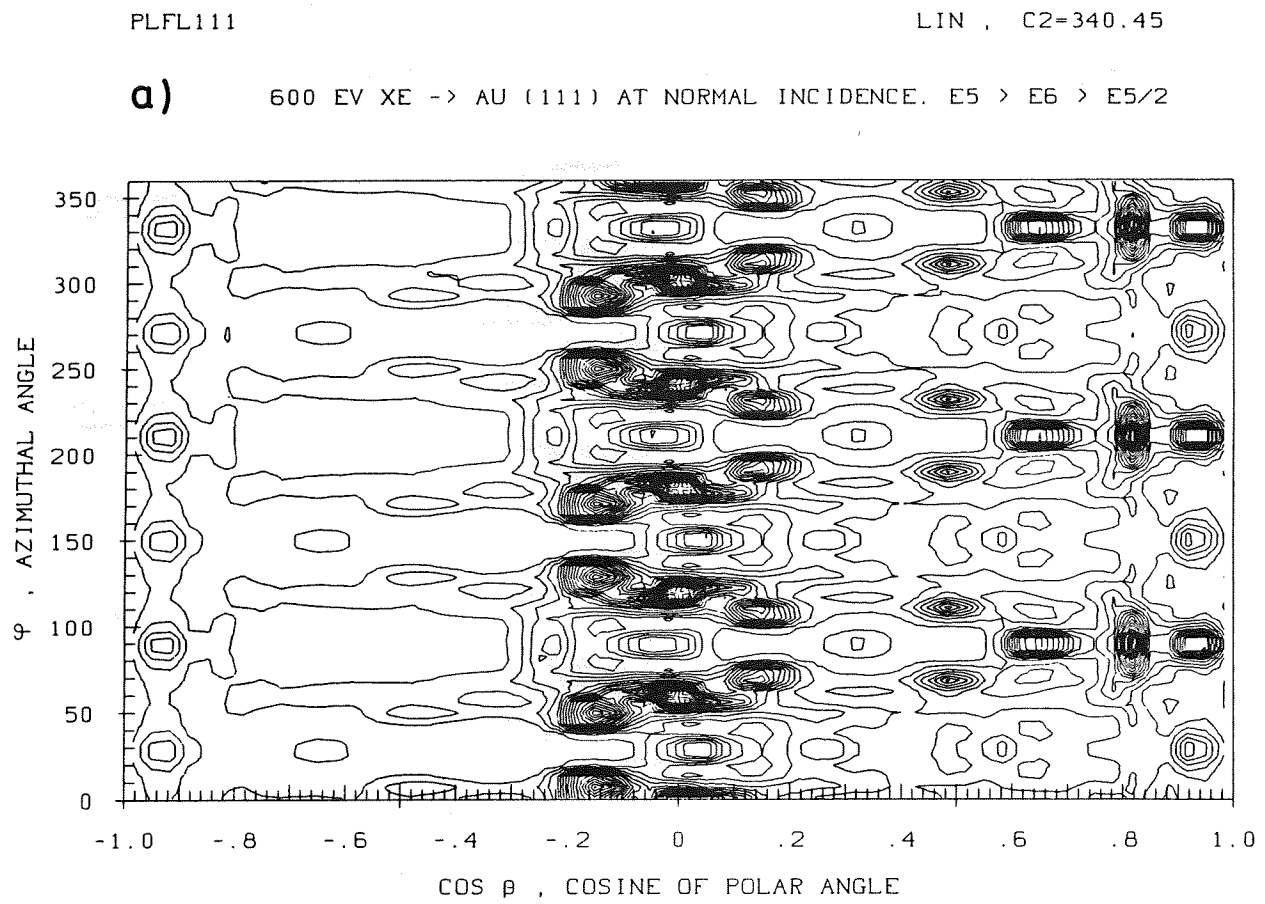
PLFL111
LIN , C2=340.45
a) 600 EV XE -> AU (111) AT NORMAL INCIDENCE. E5 > E6 > E5/2
350
300
250
200
150
100
50
0
φ , AZIMUTHAL ANGLE
-1.0
-.8
-.6
-.4
-.2
0
.2
.4
.6
.8
1.0
COS β , COSINE OF POLAR ANGLE

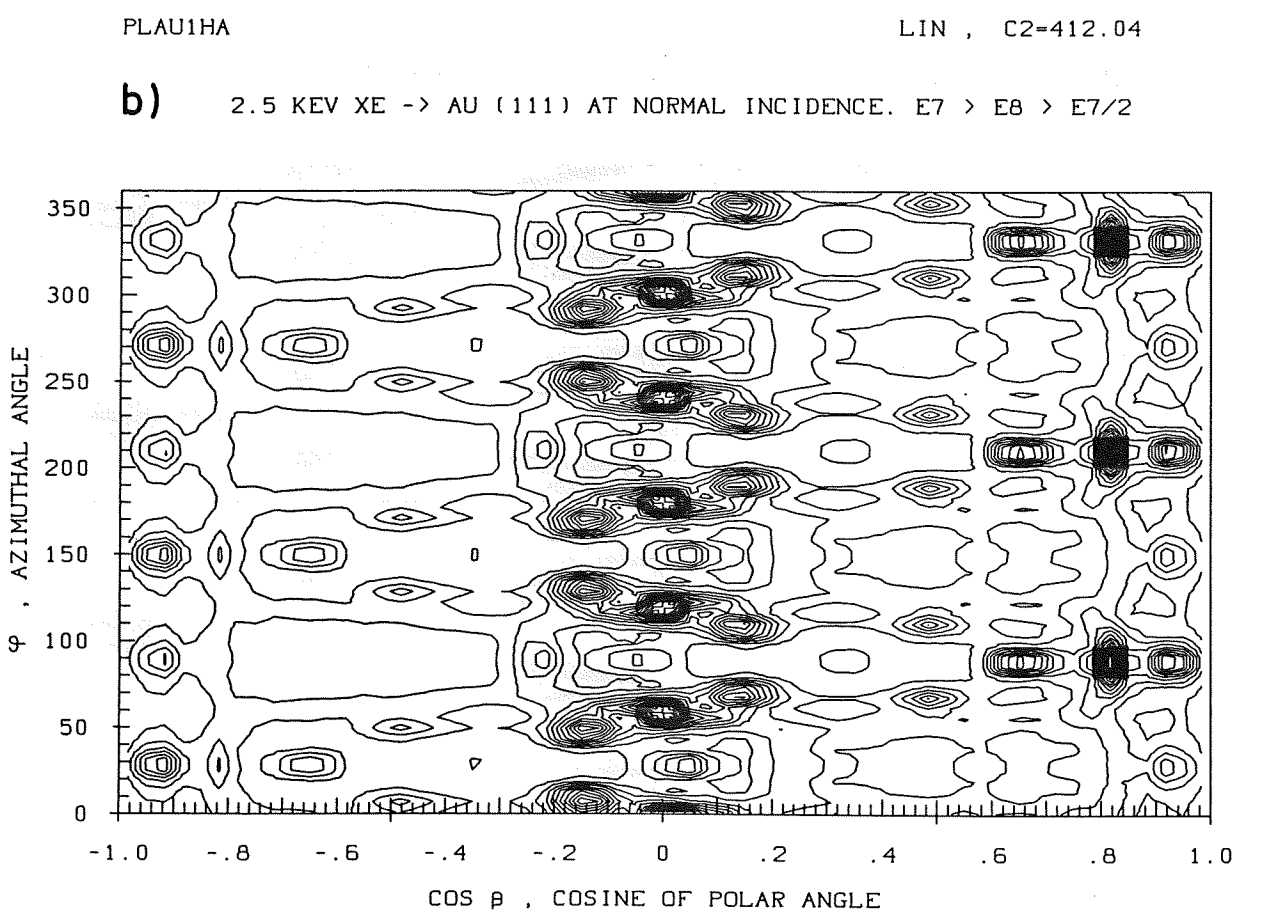
PLAU1HA
LIN , C2=412.04
b) 2.5 KEV XE -> AU (111) AT NORMAL INCIDENCE. E7 > E8 > E7/2
350
300
250
200
150
100
50
0
φ , AZIMUTHAL ANGLE
-1.0
-.8
-.6
-.4
-.2
0
.2
.4
.6
.8
1.0
COS β , COSINE OF POLAR ANGLE

Fig. 18a,b

Figures 19 to 24

Contour line spots representing the direction distributions of moving atoms in cascades generated by 2.5 keV Xe atoms. In fig. 19 to 24a, replacement sequences are truncated, they are included in fig. 19 to 24b. The plots are drawn for energies just above the replacement threshold (fig. 19) down to the cohesive energy for gold (fig. 24).

PLXE1N1 LIN , C2=15.62

a) 2.5 KEV XE -> AU (111) AT NORMAL INCIDENCE. E2 > E3 > E2/2

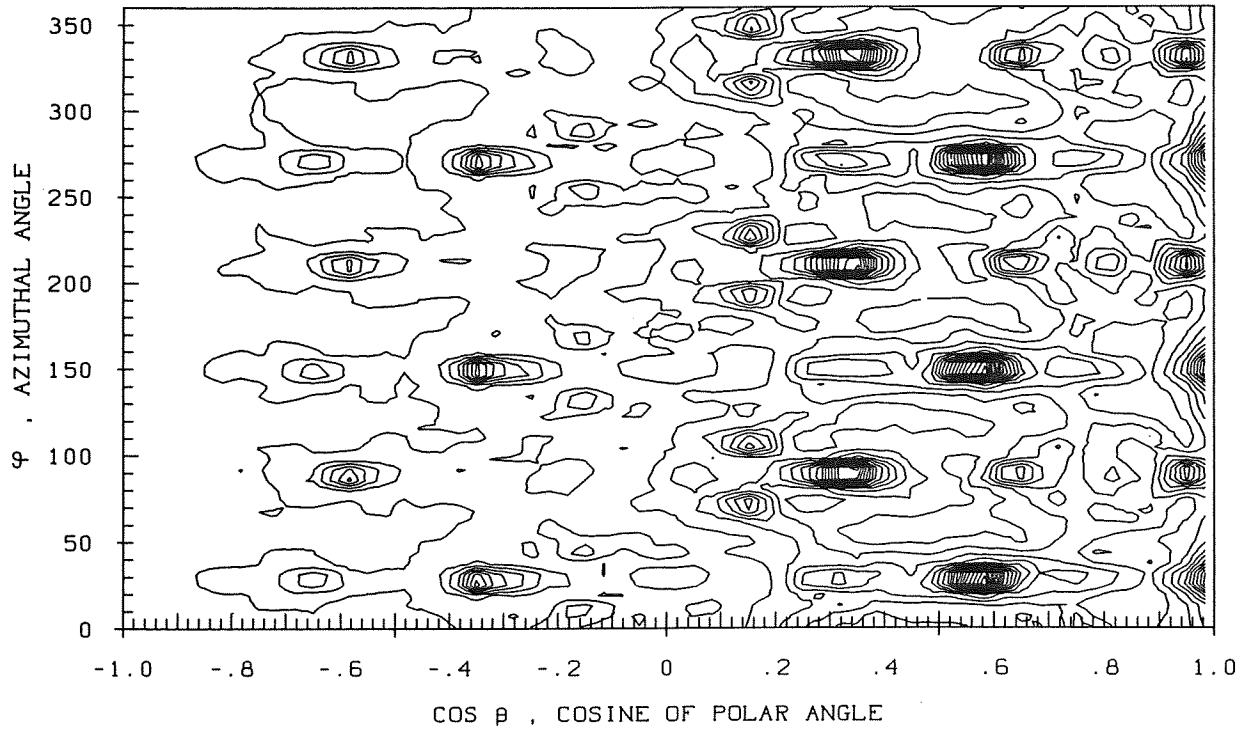

PLAU1HA LIN , C2=18.44

b) 2.5 KEV XE -> AU (111) AT NORMAL INCIDENCE. E2 > E3 > E2/2

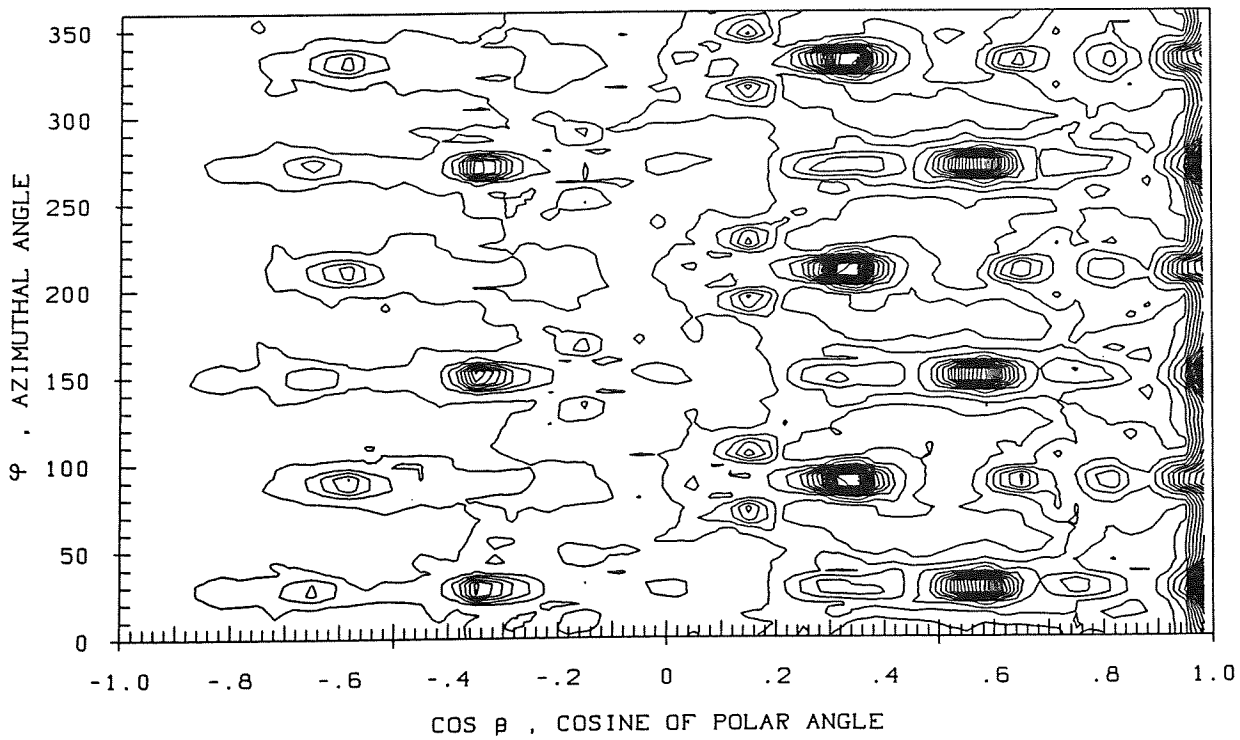

Fig. 19a,b

PLXE1N1 LIN , C2=18.41

a) 2.5 KEV XE -> AU (111) AT NORMAL INCIDENCE. E3 > E4 > E3/2

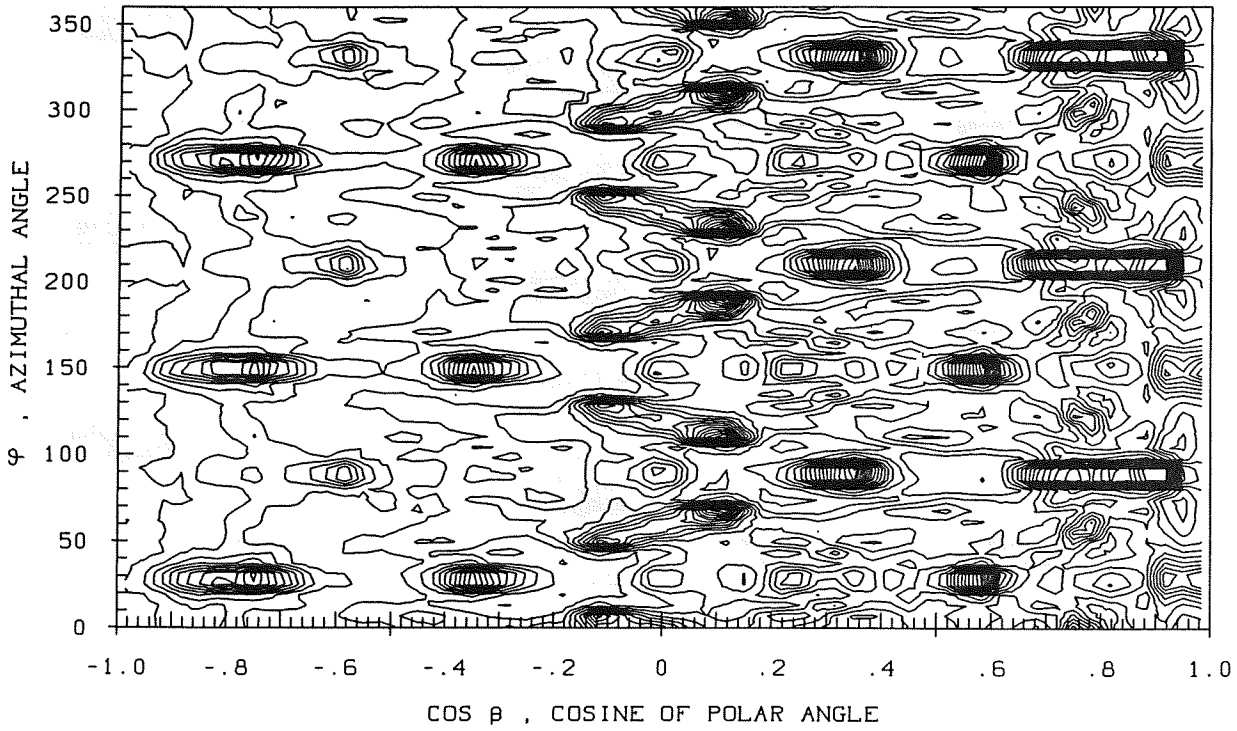

PLAU1HA LIN , C2=46.59

b) 2.5 KEV XE -> AU (111) AT NORMAL INCIDENCE. E3 > E4 > E3/2

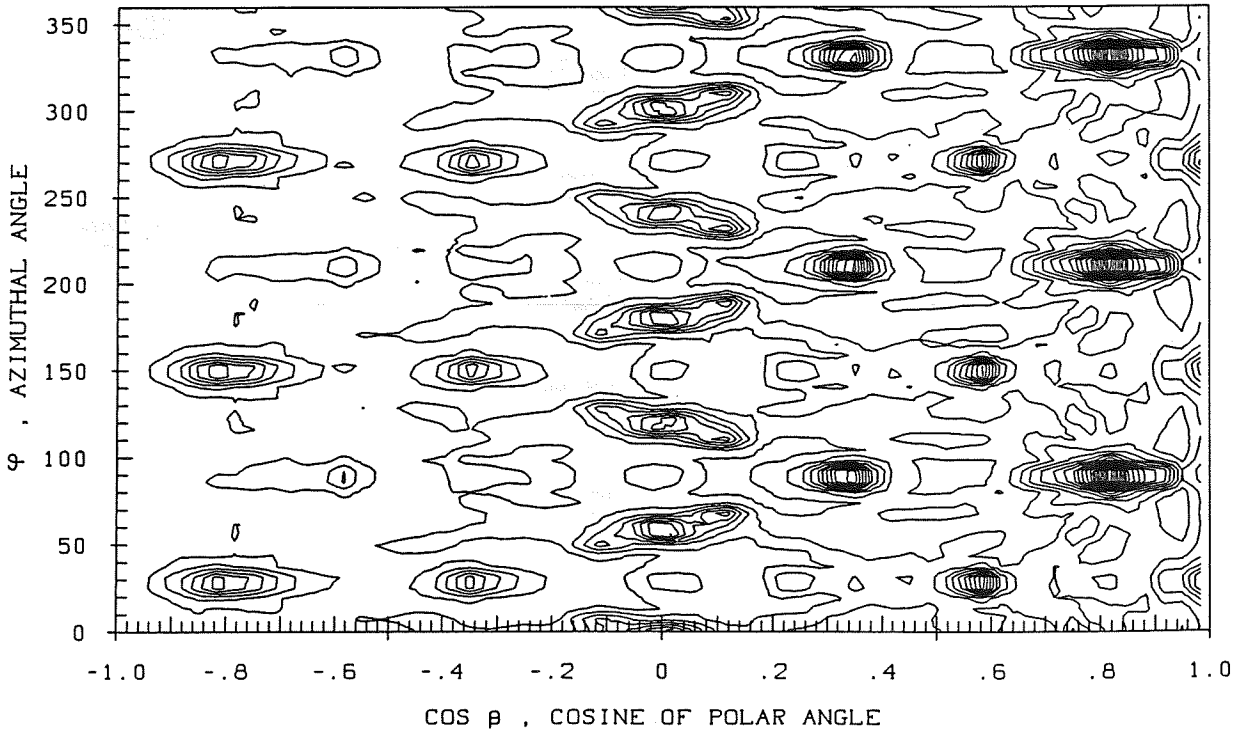

Fig. 20a,b

PLXE1N1 LIN , C2=40.40

a) 2.5 KEV XE -> AU (111) AT NORMAL INCIDENCE. E4 > E5 > E4/2

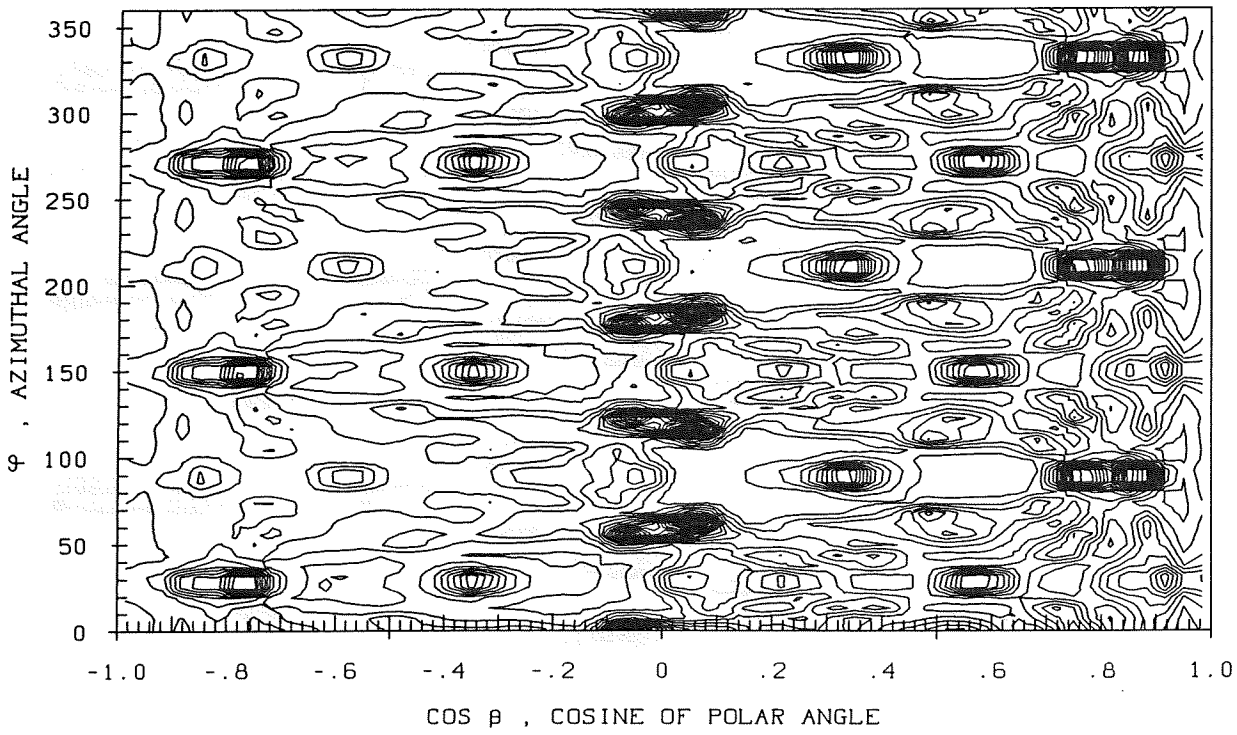

PLAU1HA LIN , C2=88.65

b) 2.5 KEV XE -> AU (111) AT NORMAL INCIDENCE. E4 > E5 > E4/2

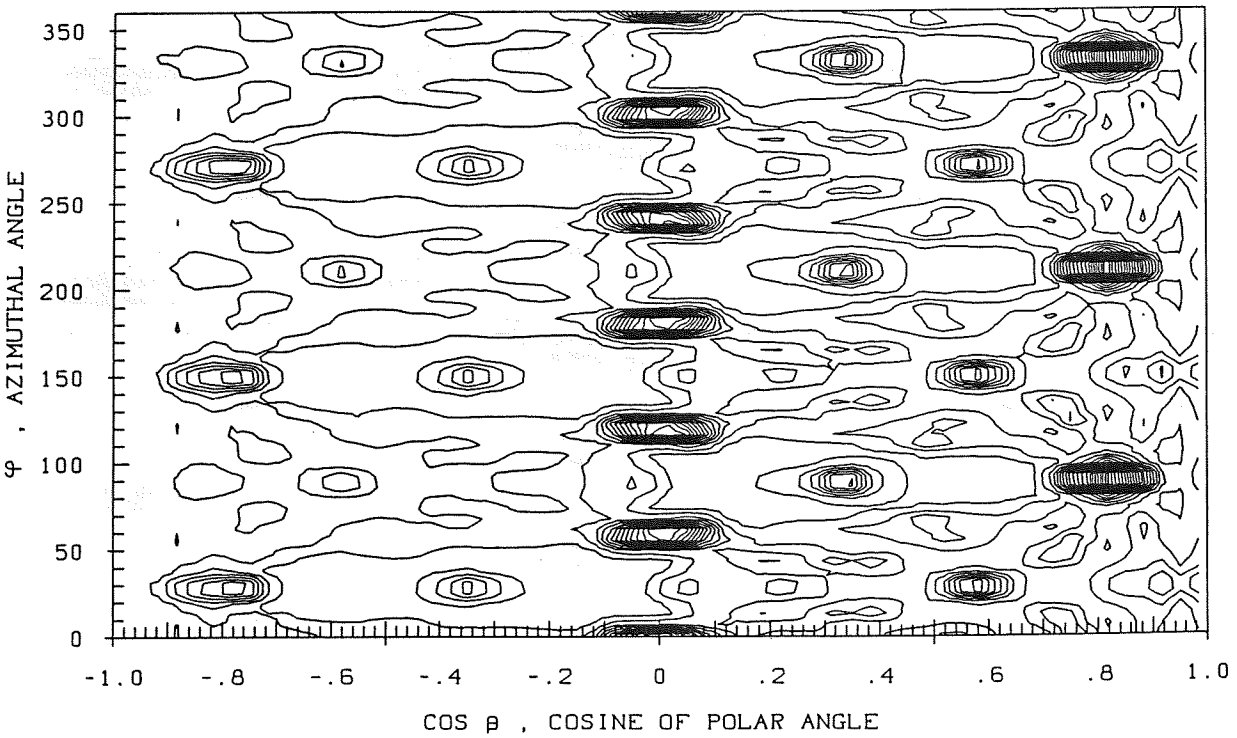

Fig. 21a,b

PLXE1N1 LIN , C2=101.52

a) 2.5 KEV XE -> AU (111) AT NORMAL INCIDENCE. E5 > E6 > E5/2

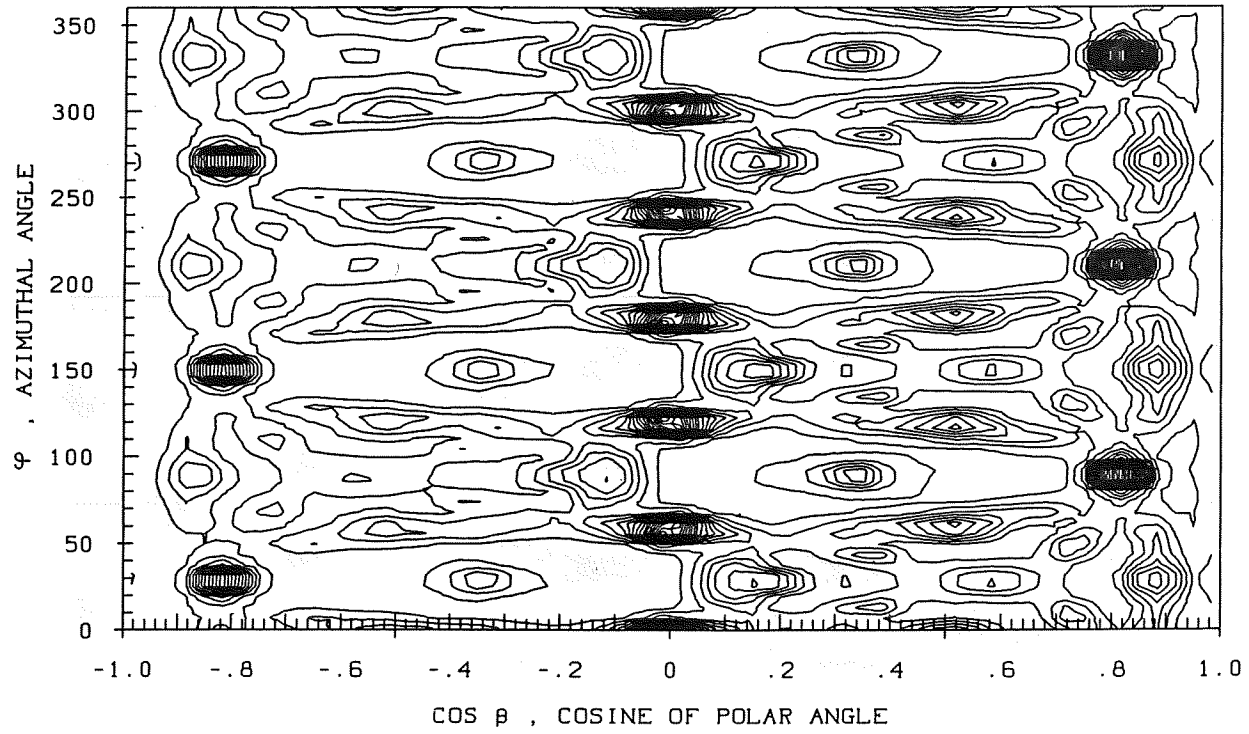

PLAU1HA LIN , C2=237.93

b) 2.5 KEV XE -> AU (111) AT NORMAL INCIDENCE. E5 > E6 > E5/2

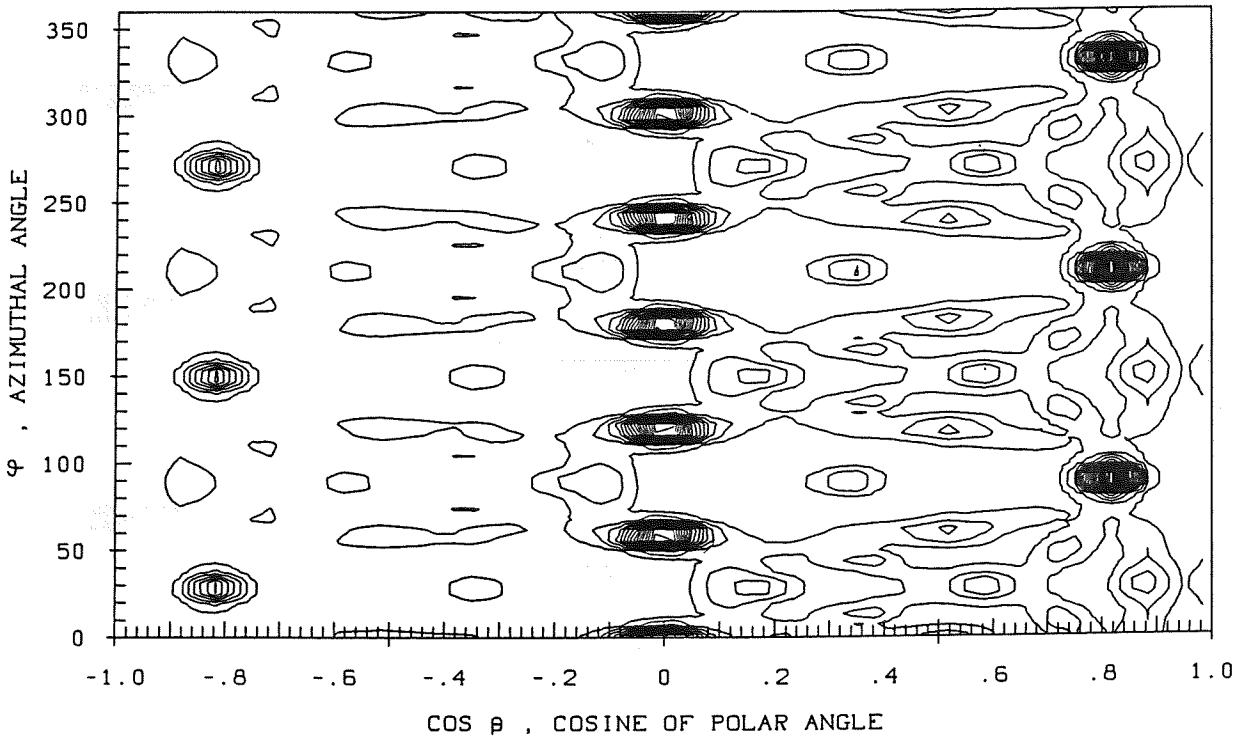

Fig. 22a,b

PLXE1N1 LIN , C2=81.48

a) 2.5 KEV XE -> AU (111) AT NORMAL INCIDENCE. E6 > E7 > E6/2

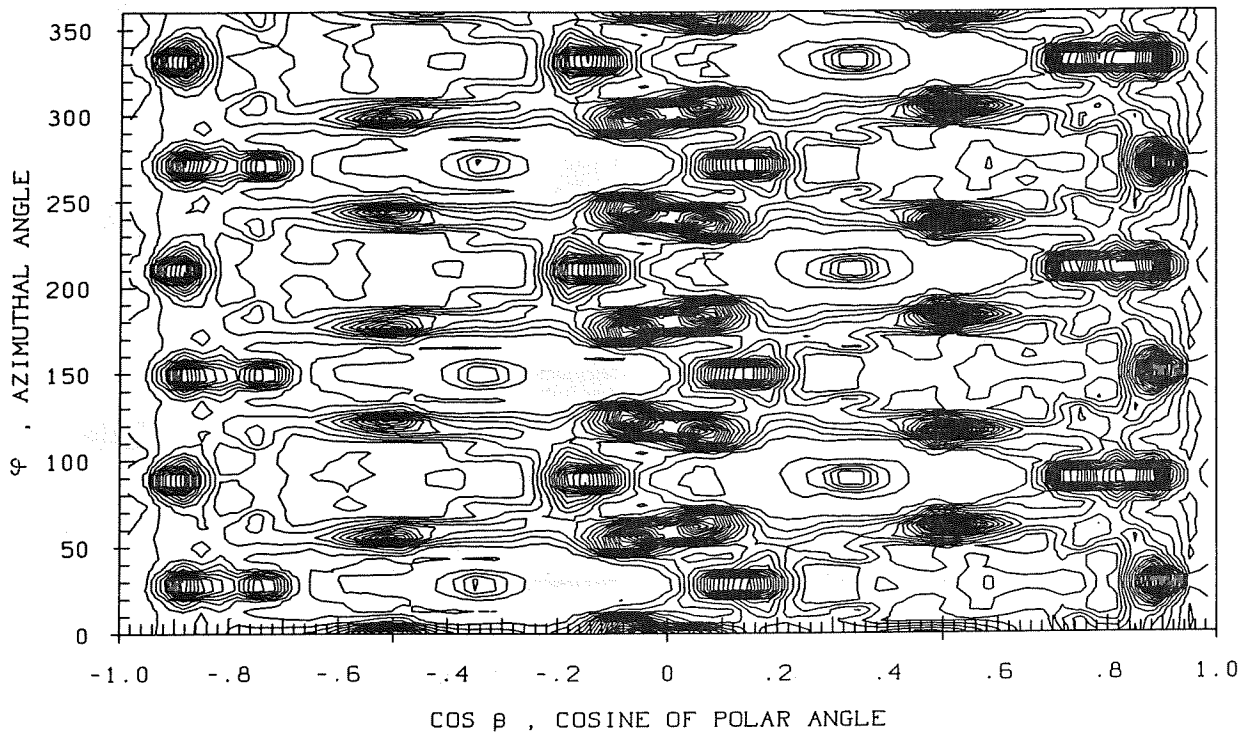

PLAU1HA LIN , C2=262.21

b) 2.5 KEV XE -> AU (111) AT NORMAL INCIDENCE. E6 > E7 > E6/2

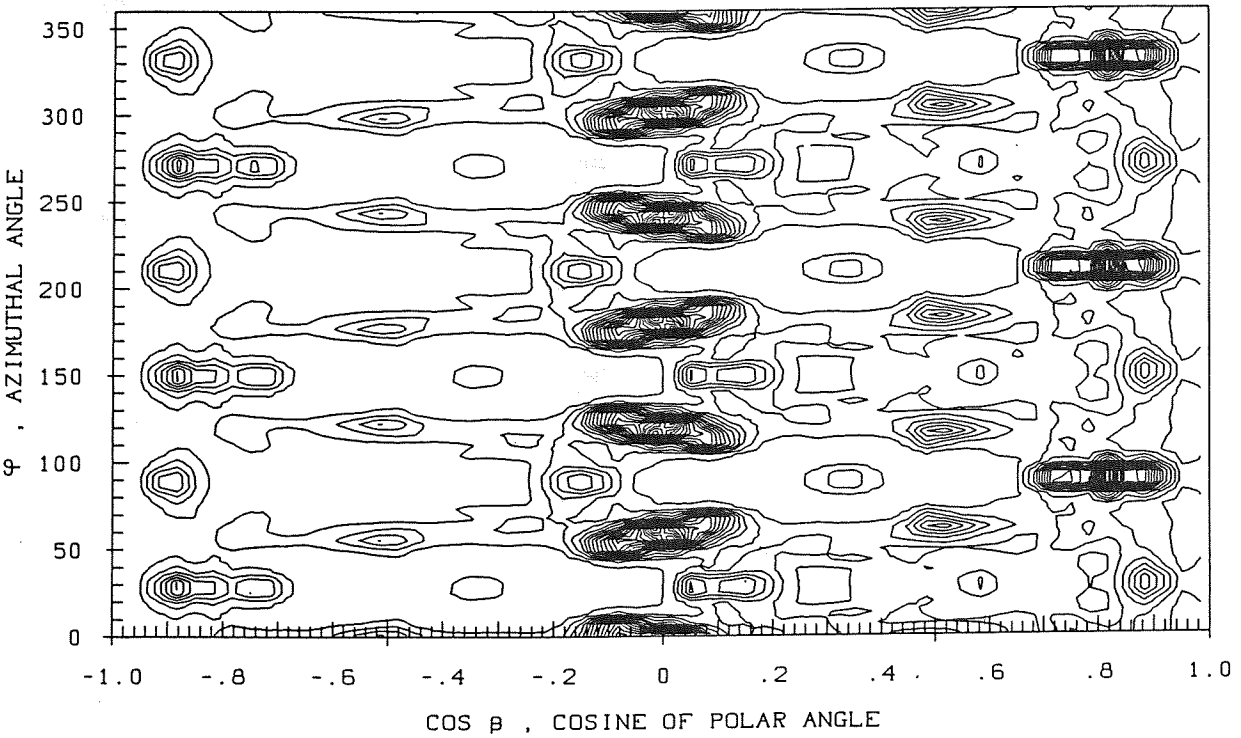

Fig. 23a,b

PLXE1N1 LIN , C2=106.12

a) 2.5 KEV XE -> AU (111) AT NORMAL INCIDENCE. E7 > E8 > E7/2

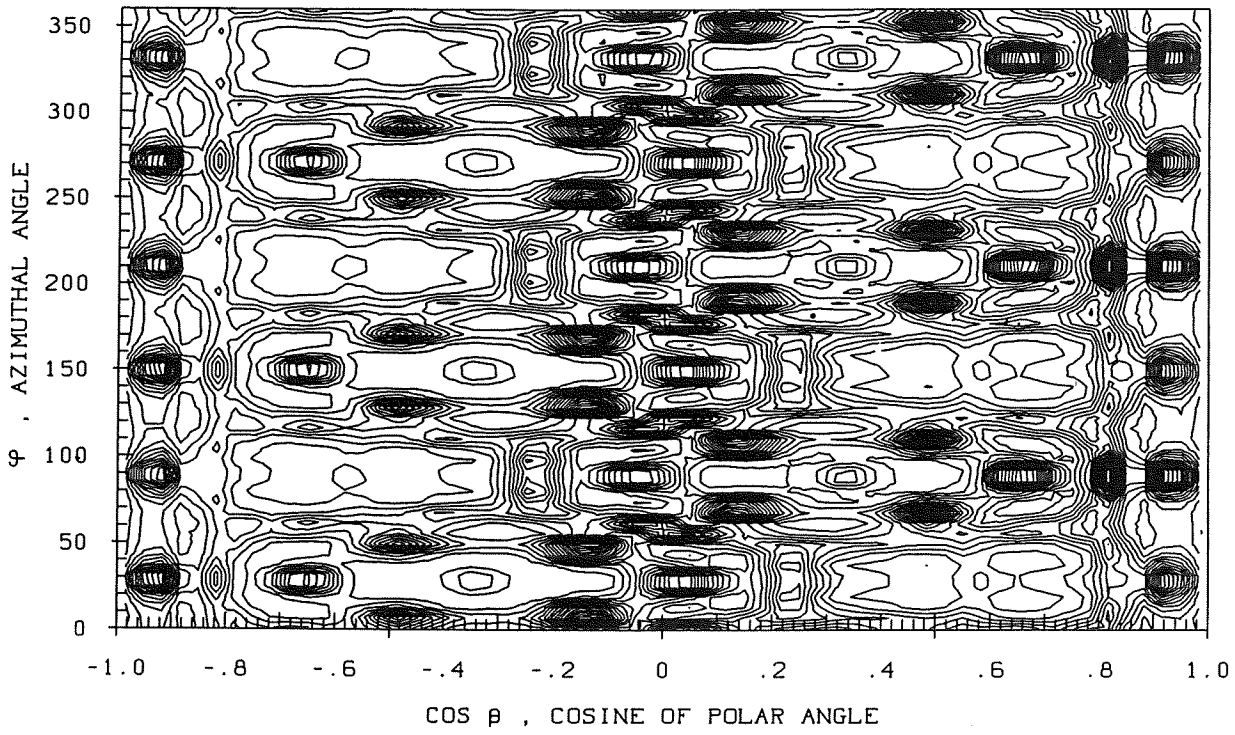

PLAU1HA LIN , C2=412.04

b) 2.5 KEV XE -> AU (111) AT NORMAL INCIDENCE. E7 > E8 > E7/2

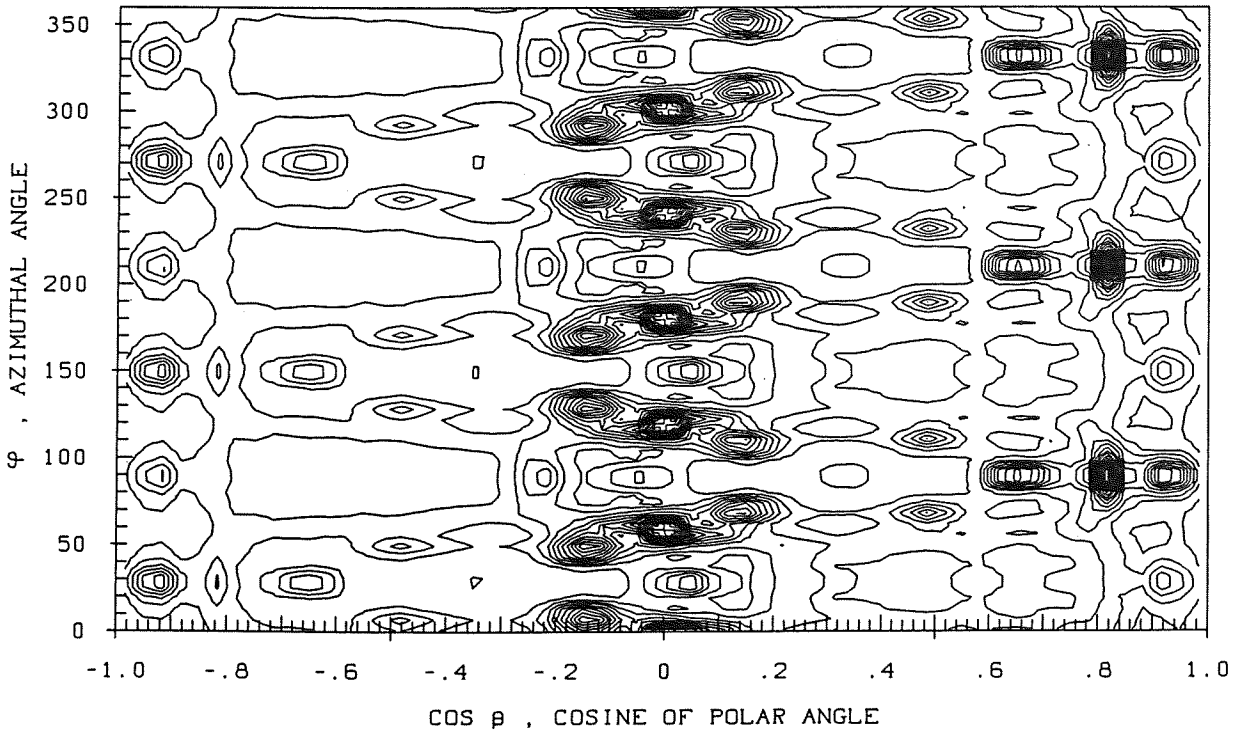

Fig. 24a,b

Figures 25 to 32

Contour line plots representing the direction distributions of moving atoms in cascades generated by 2.5 keV Xe atoms. 600 ^{o}K uncorrelated thermal displacements of gold atoms are included in the simulations. The results are shown at different steps of the energy dissipation. The loci of the directions parallel to {111} planes are shown in each figure in order to guide the eyes when looking to the planar focusing effect.

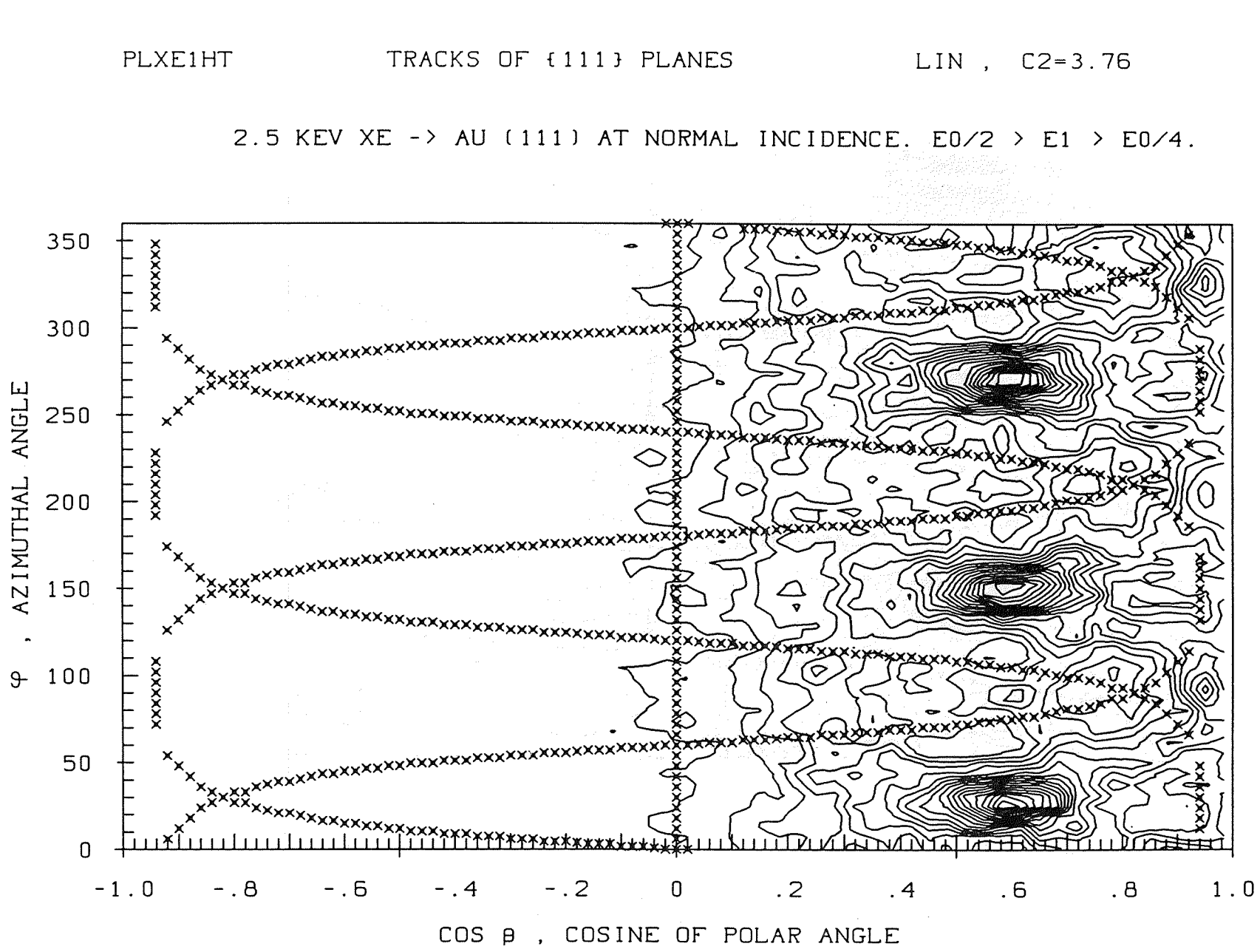
PLXE1HT
TRACKS OF {111} PLANES
LIN , C2=3.76
2.5 KEV XE -> AU (111) AT NORMAL INCIDENCE. E0/2 > E1 > E0/4.
350
300
250
200
150
100
50
0
φ , AZIMUTHAL ANGLE
-1.0
-.8
-.6
-.4
-.2
0
.2
.4
.6
.8
1.0
COS β , COSINE OF POLAR ANGLE

Fig. 25

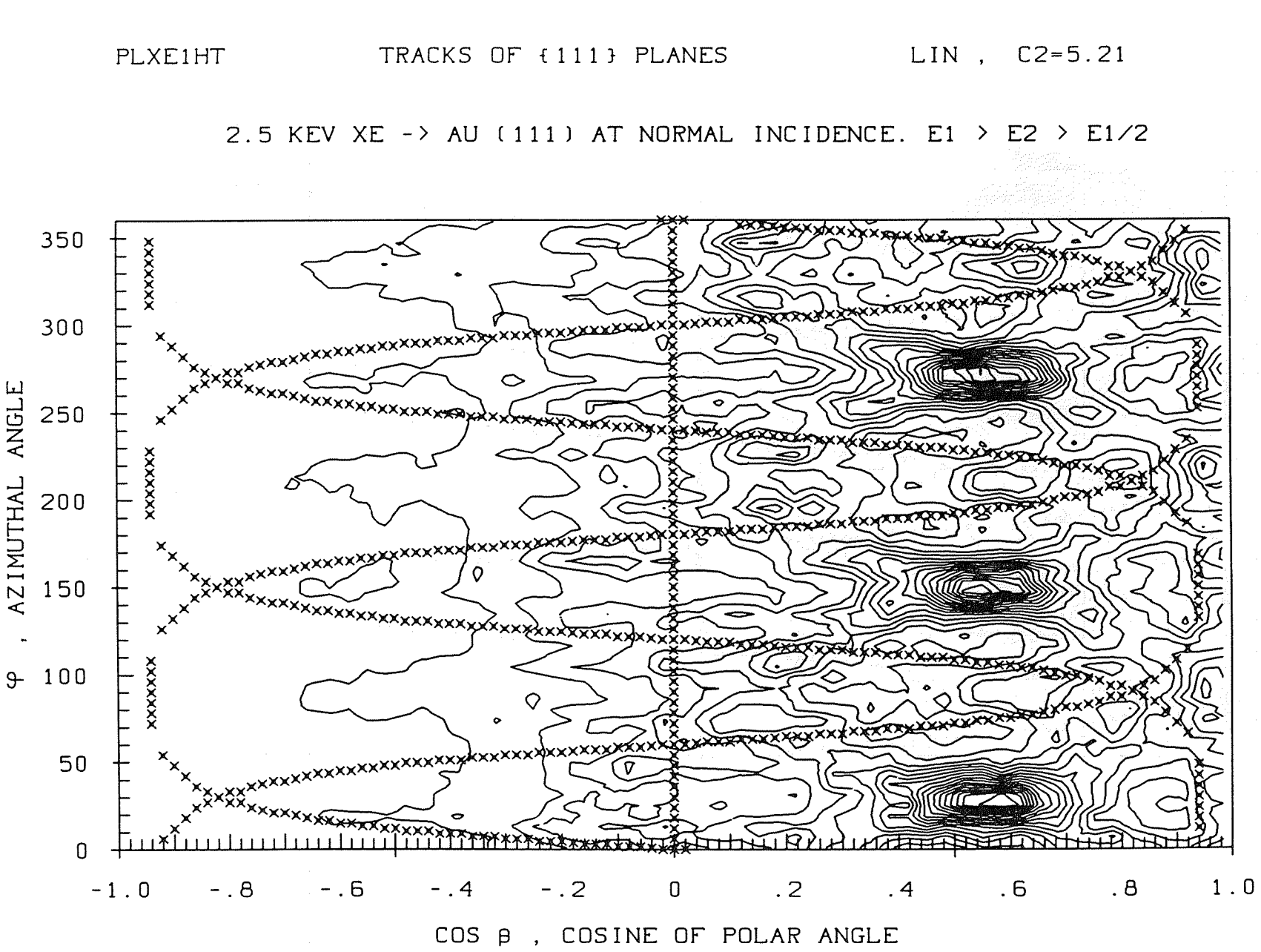
PLXE1HT
TRACKS OF {111} PLANES
LIN , C2=5.21
2.5 KEV XE -> AU (111) AT NORMAL INCIDENCE. E1 > E2 > E1/2
350
300
250
200
150
100
50
0
φ , AZIMUTHAL ANGLE
-1.0
-.8
-.6
-.4
-.2
0
.2
.4
.6
.8
1.0
COS β , COSINE OF POLAR ANGLE

Fig. 26

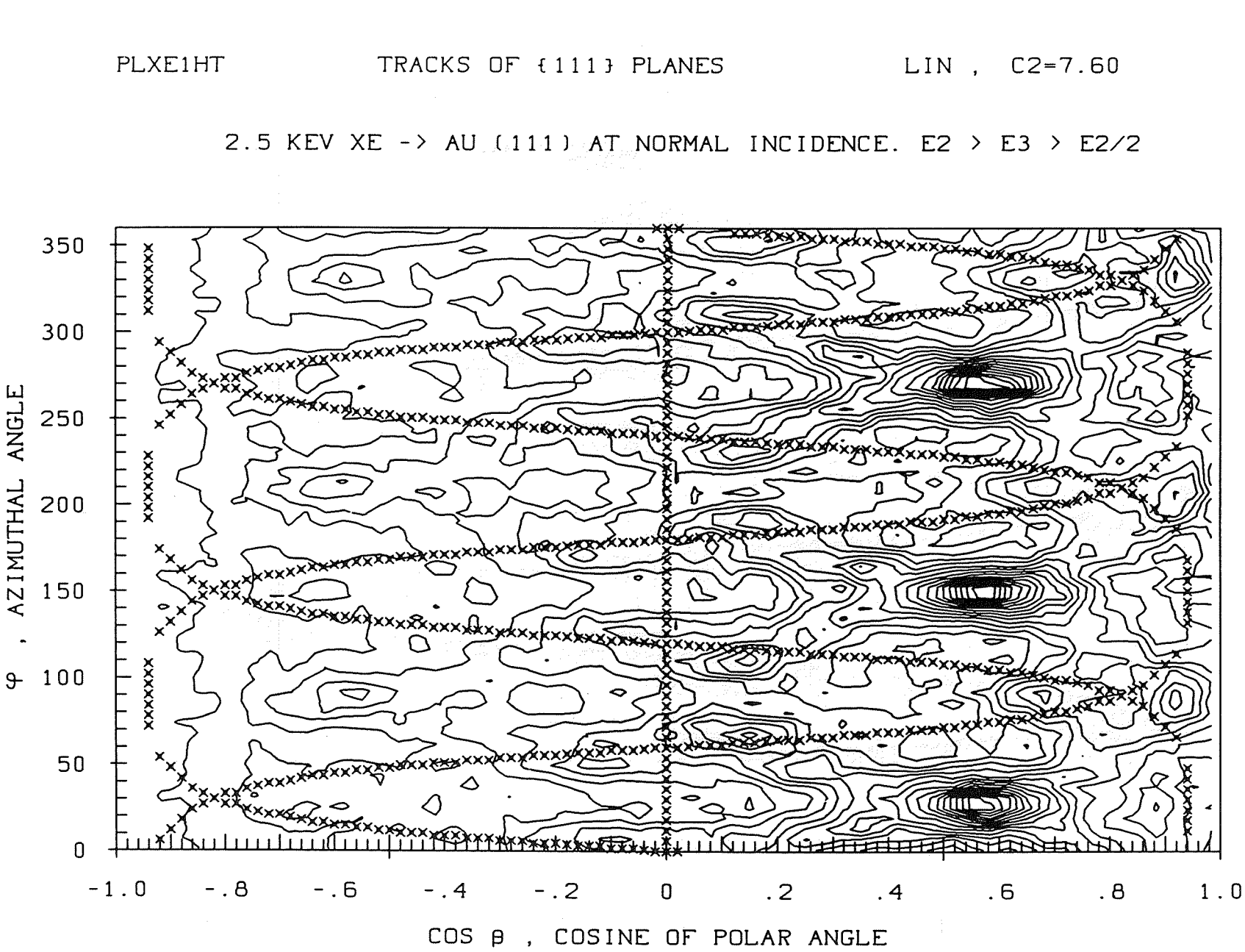
PLXE1HT
TRACKS OF {111} PLANES
LIN , C2=7.60
2.5 KEV XE -> AU (111) AT NORMAL INCIDENCE. E2 > E3 > E2/2
φ , AZIMUTHAL ANGLE
350
300
250
200
150
100
50
0
-1.0
-.8
-.6
-.4
-.2
0
.2
.4
.6
.8
1.0
COS β , COSINE OF POLAR ANGLE

Fig. 27

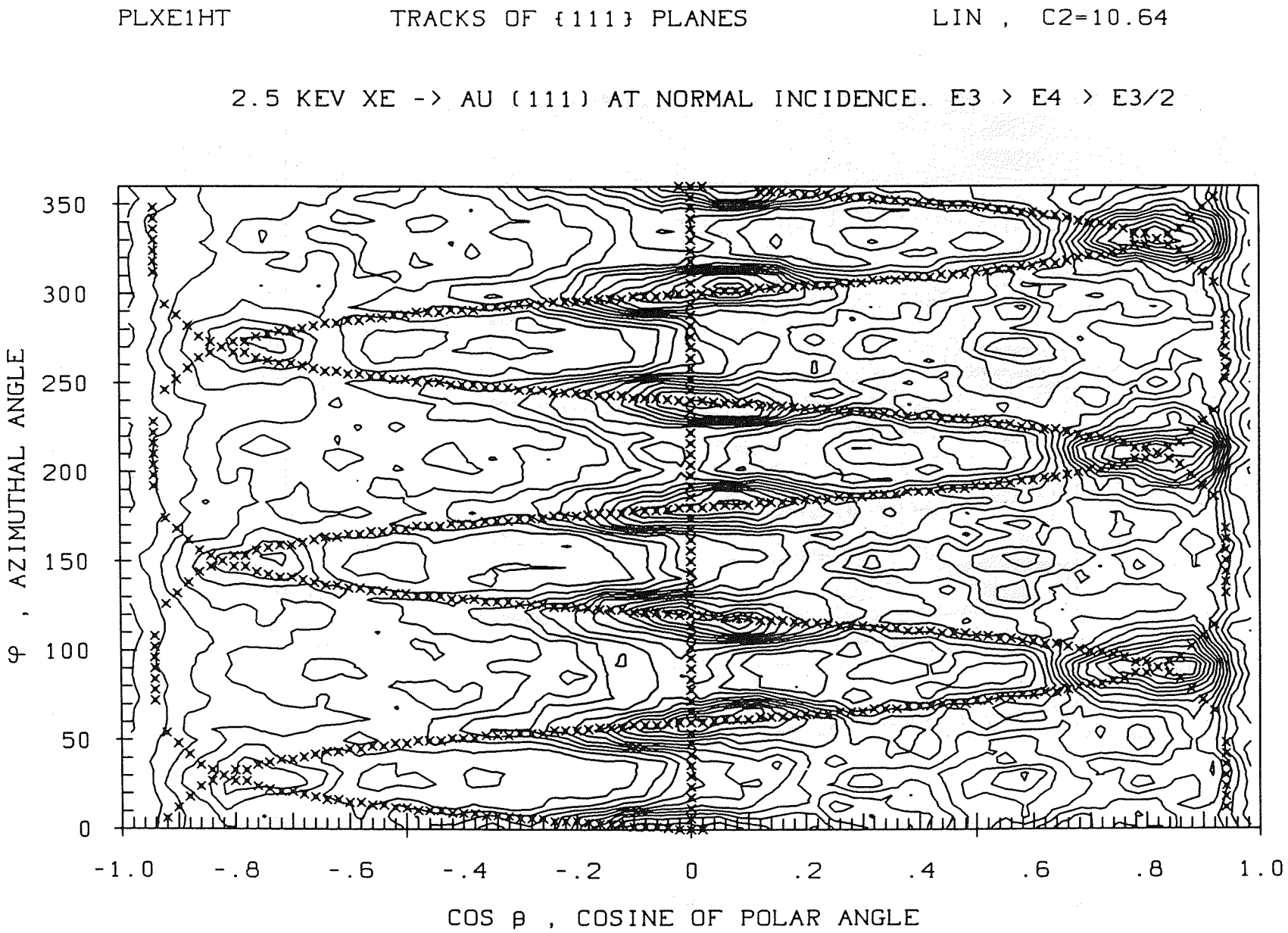
PLXE1HT
TRACKS OF {111} PLANES
LIN , C2=10.64
2.5 KEV XE -> AU (111) AT NORMAL INCIDENCE. E3 > E4 > E3/2
350
300
250
200
150
100
50
0
φ , AZIMUTHAL ANGLE
-1.0
-.8
-.6
-.4
-.2
0
.2
.4
.6
.8
1.0
COS β , COSINE OF POLAR ANGLE

Fig. 28

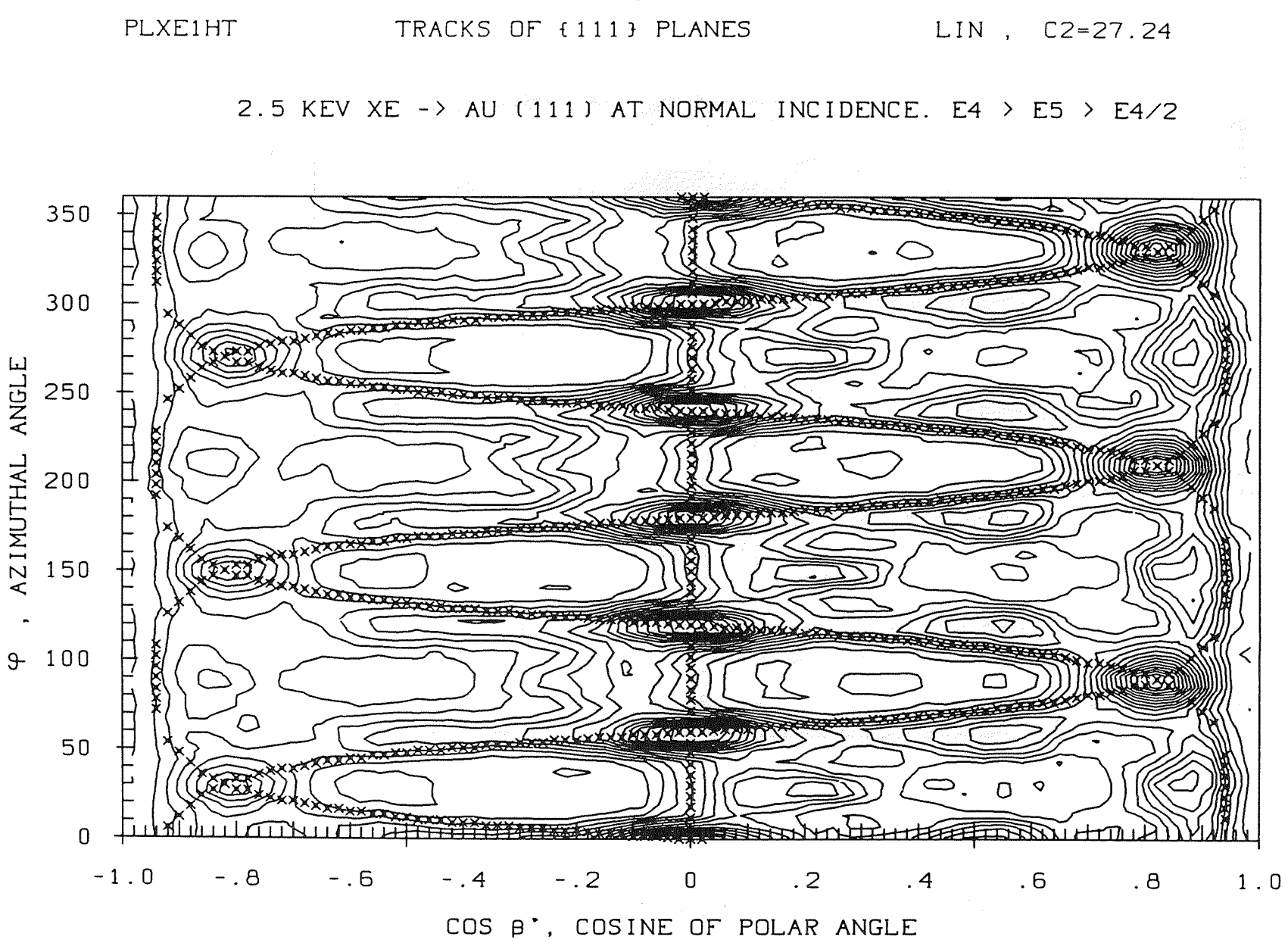
PLXE1HT
TRACKS OF {111} PLANES
LIN , C2=27.24
2.5 KEV XE -> AU (111) AT NORMAL INCIDENCE. E4 > E5 > E4/2
350
300
250
200
150
100
50
0
φ , AZIMUTHAL ANGLE
-1.0
-.8
-.6
-.4
-.2
0
.2
.4
.6
.8
1.0
COS β*, COSINE OF POLAR ANGLE

Fig. 29

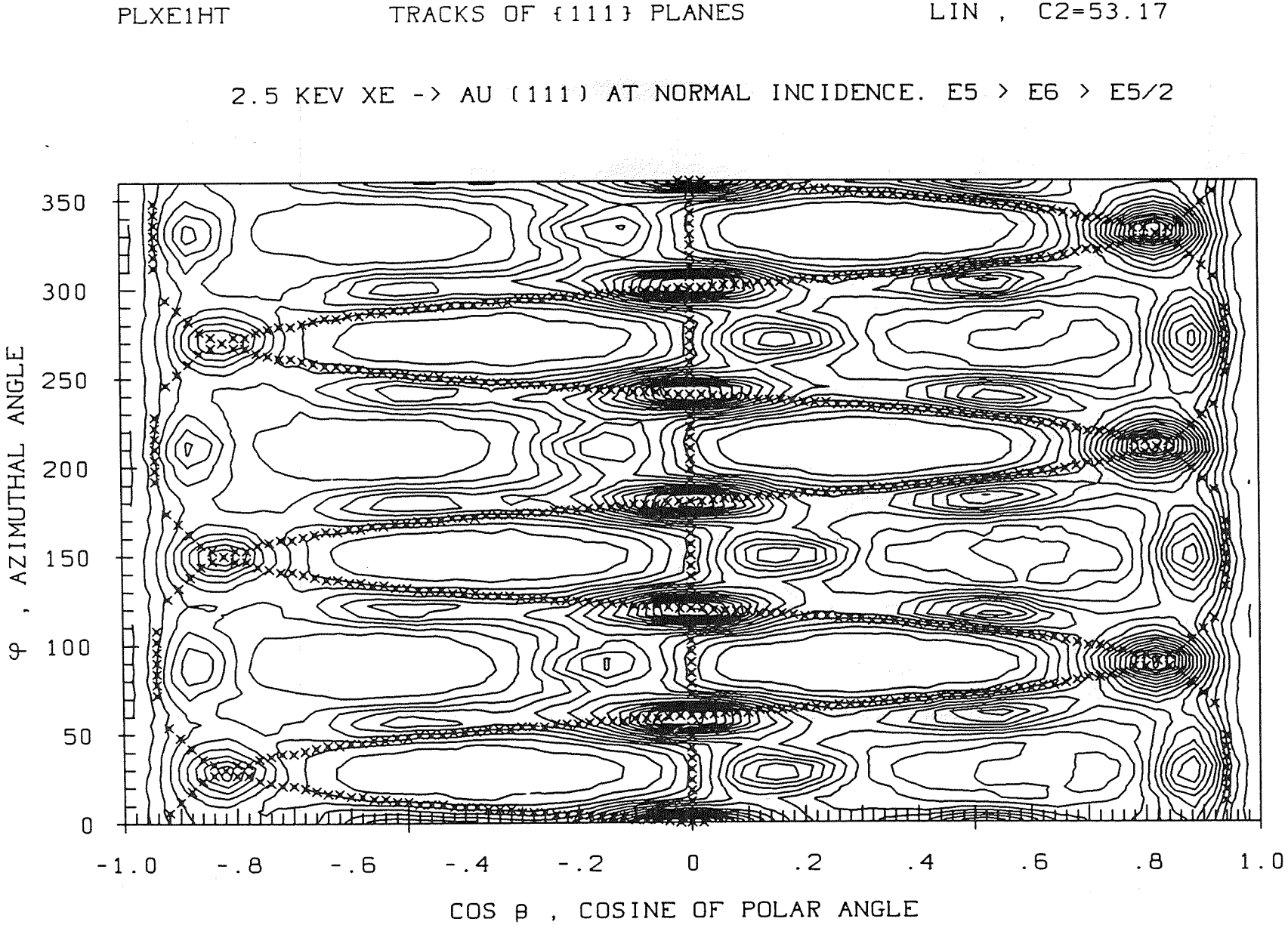
PLXE1HT
TRACKS OF {111} PLANES
LIN , C2=53.17
2.5 KEV XE -> AU (111) AT NORMAL INCIDENCE. E5 > E6 > E5/2
350
300
250
200
150
100
50
0
φ , AZIMUTHAL ANGLE
-1.0
-.8
-.6
-.4
-.2
0
.2
.4
.6
.8
1.0
COS β , COSINE OF POLAR ANGLE

Fig. 30

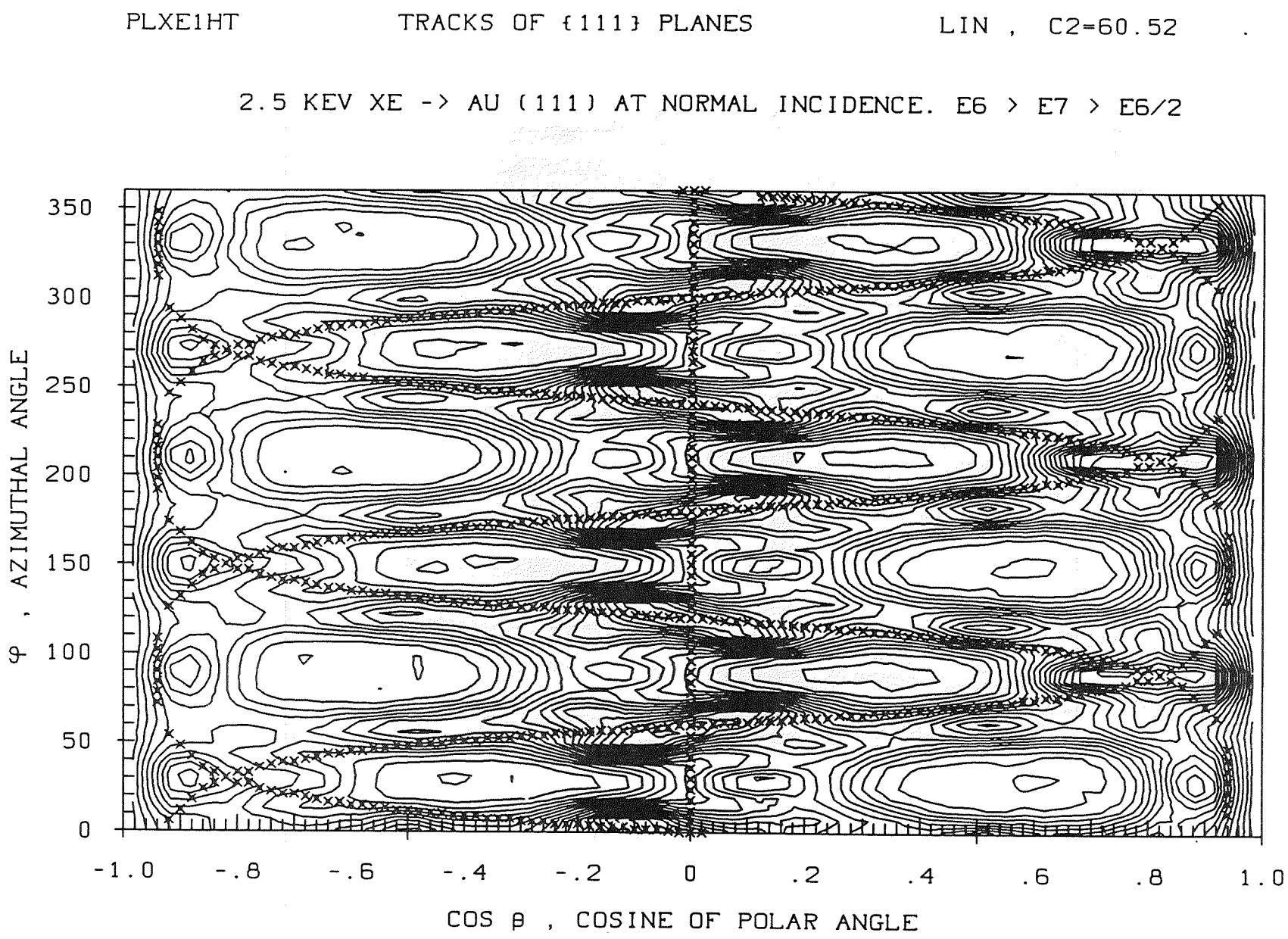
PLXE1HT
TRACKS OF {111} PLANES
LIN , C2=60.52
2.5 KEV XE -> AU (111) AT NORMAL INCIDENCE. E6 > E7 > E6/2
φ , AZIMUTHAL ANGLE
350
300
250
200
150
100
50
0
-1.0
-.8
-.6
-.4
-.2
0
.2
.4
.6
.8
1.0
COS β , COSINE OF POLAR ANGLE

Fig. 31

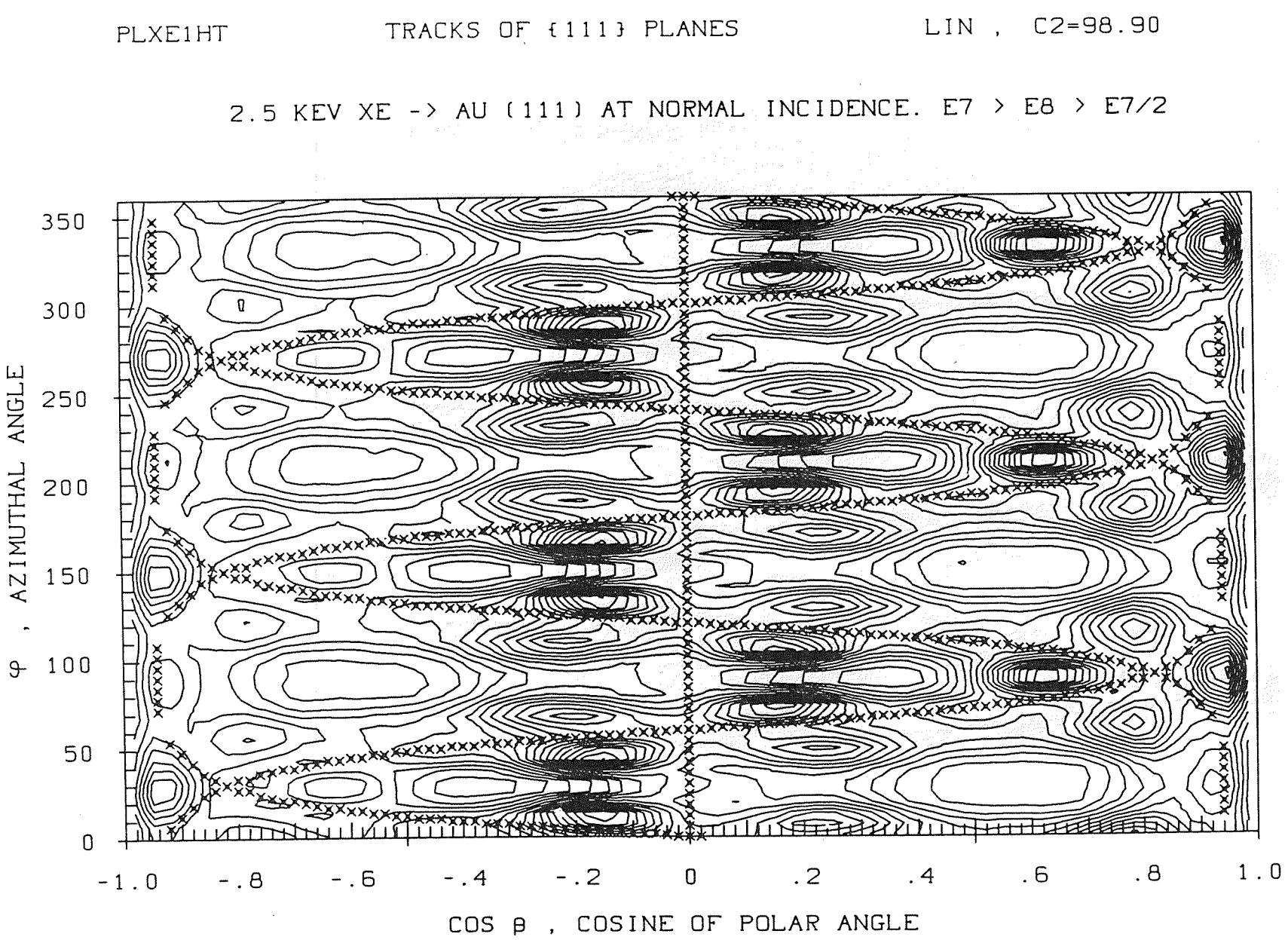
PLXE1HT
TRACKS OF {111} PLANES
LIN , C2=98.90
2.5 KEV XE -> AU (111) AT NORMAL INCIDENCE. E7 > E8 > E7/2
350
300
250
200
150
100
50
0
φ , AZIMUTHAL ANGLE
-1.0
-.8
-.6
-.4
-.2
0
.2
.4
.6
.8
1.0
COS β , COSINE OF POLAR ANGLE

Fig. 32

Figures 33 to 39

Contour line plots representing the direction distributions of moving atoms in cascades generated by 600 eV Xe atoms. The plots are drawn for atoms whose kinetic energy get lower than $E_0/2^n$ but greater than $E_0/2^{n+1}$, with n increasing from n=1 in fig. 25 to n=7 in fig. 31. Three different situations are compared:

a) Direction distributions in the half space including the vacuum and limited to half the interplanar spacing,

b) Same as in a), but the distributions for atoms moving in the vacuum is limited to those that fulfil the conditions to get sputtered,

c) Same as in b), but the refraction effect by the surface binding forces is included.

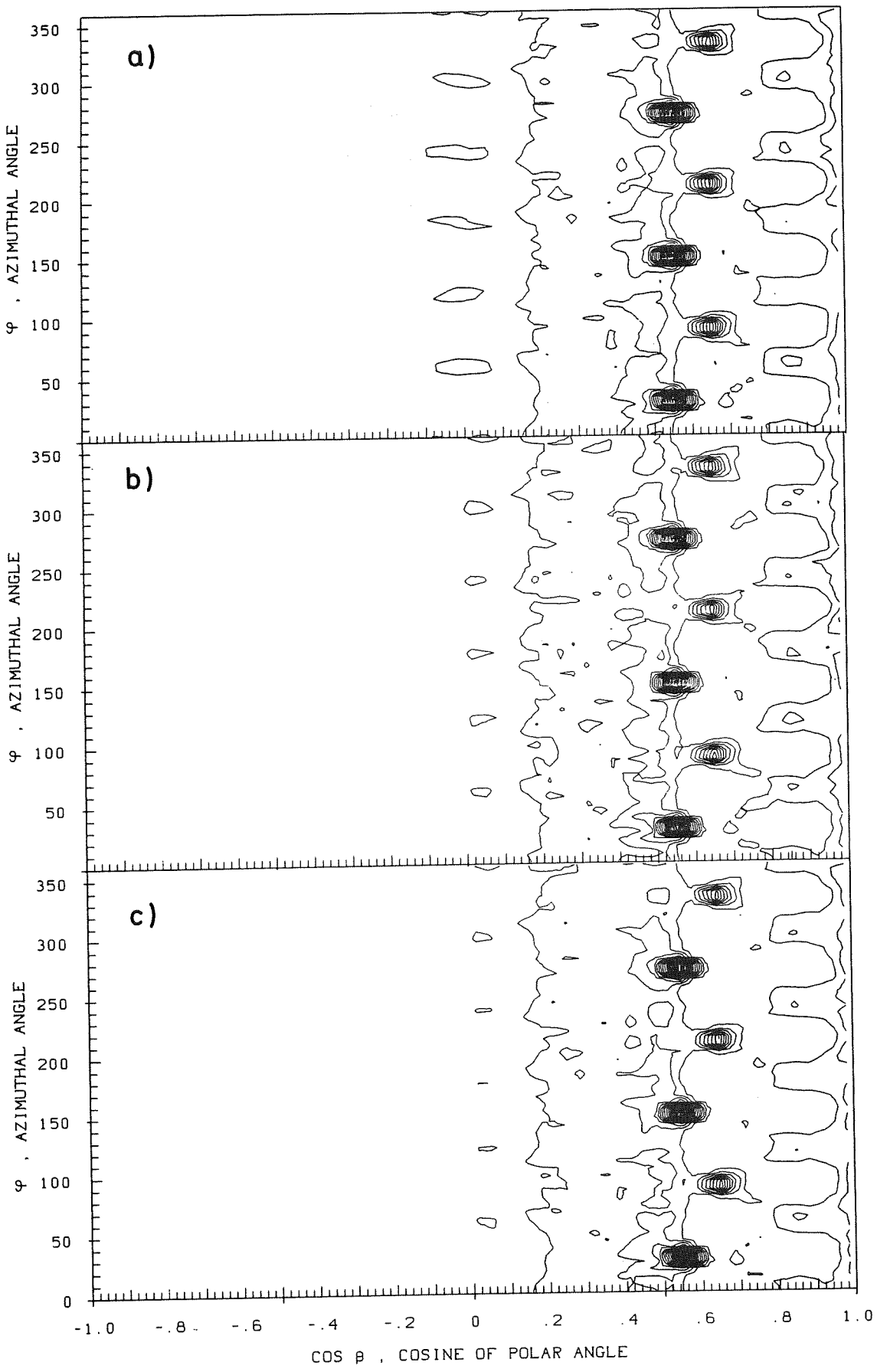
600 EV XE -> AU (111) AT NORMAL INCIDENCE. E0/2 > E1 > E0/4.
a)
b)
c)
φ , AZIMUTHAL ANGLE
350
300
250
200
150
100
50
0
-1.0
-.8
-.6
-.4
-.2
0
.2
.4
.6
.8
1.0
COS β , COSINE OF POLAR ANGLE

Fig. 33a,b,c

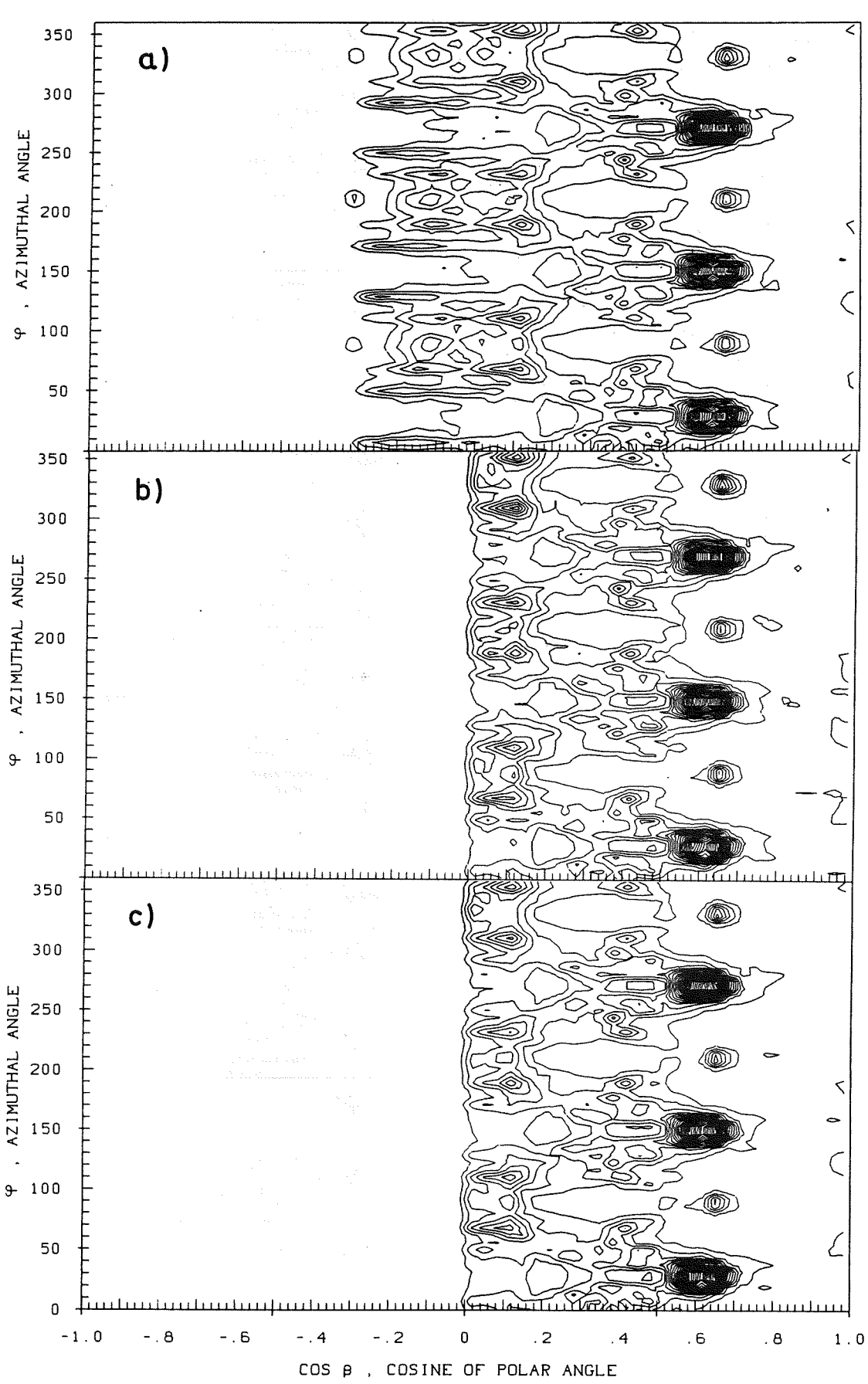
600 EV XE -> AU (111) AT NORMAL INCIDENCE. E1 > E2 > E1/2
a)
b)
c)
φ , AZIMUTHAL ANGLE
350
300
250
200
150
100
50
0
-1.0
-.8
-.6
-.4
-.2
0
.2
.4
.6
.8
1.0
COS β , COSINE OF POLAR ANGLE

Fig. 34a,b,c

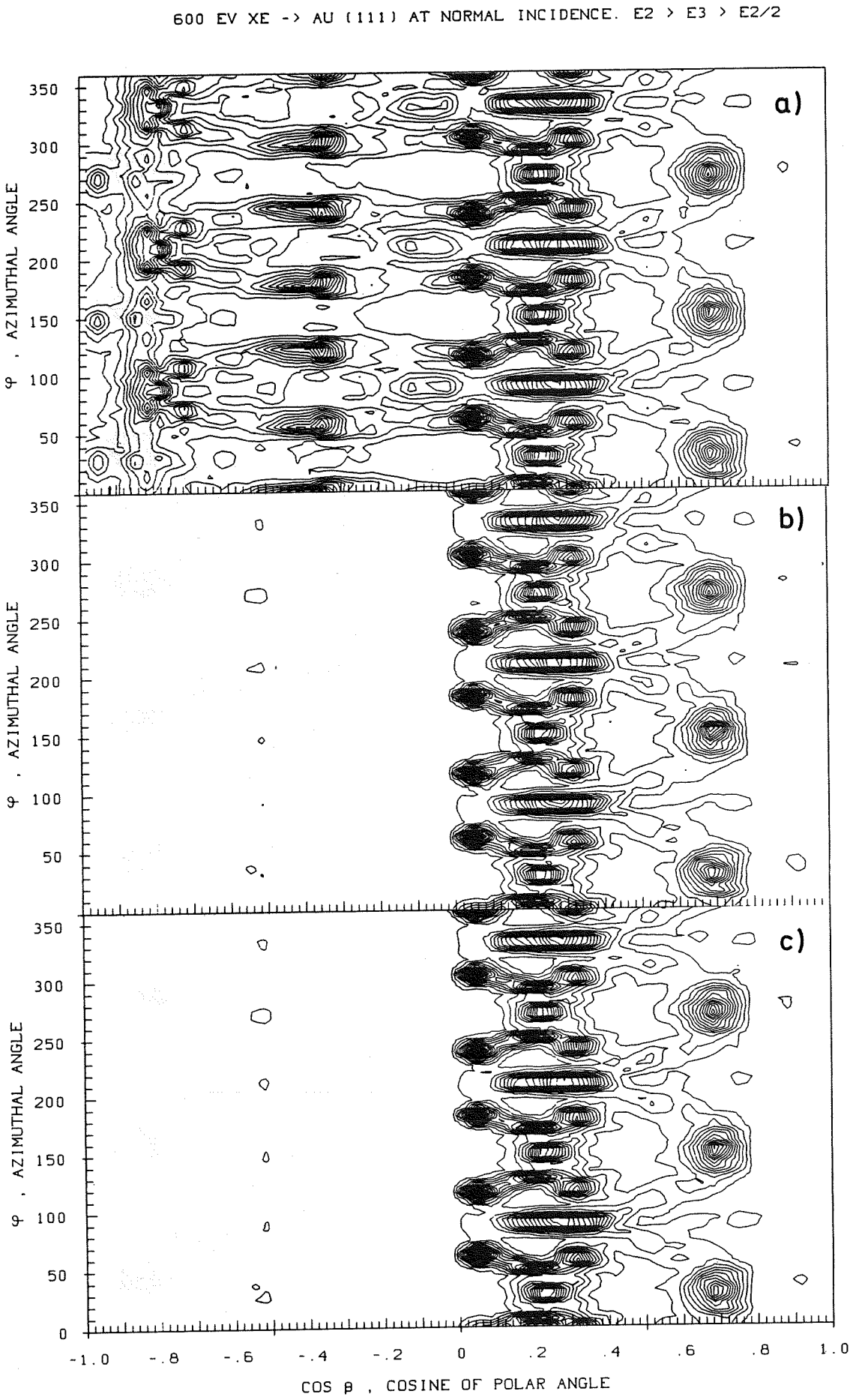
600 EV XE -> AU (111) AT NORMAL INCIDENCE. E2 > E3 > E2/2
a)
b)
c)
φ , AZIMUTHAL ANGLE
350
300
250
200
150
100
50
0
-1.0
-.8
-.6
-.4
-.2
0
.2
.4
.6
.8
1.0
COS θ , COSINE OF POLAR ANGLE

Fig. 35a,b,c

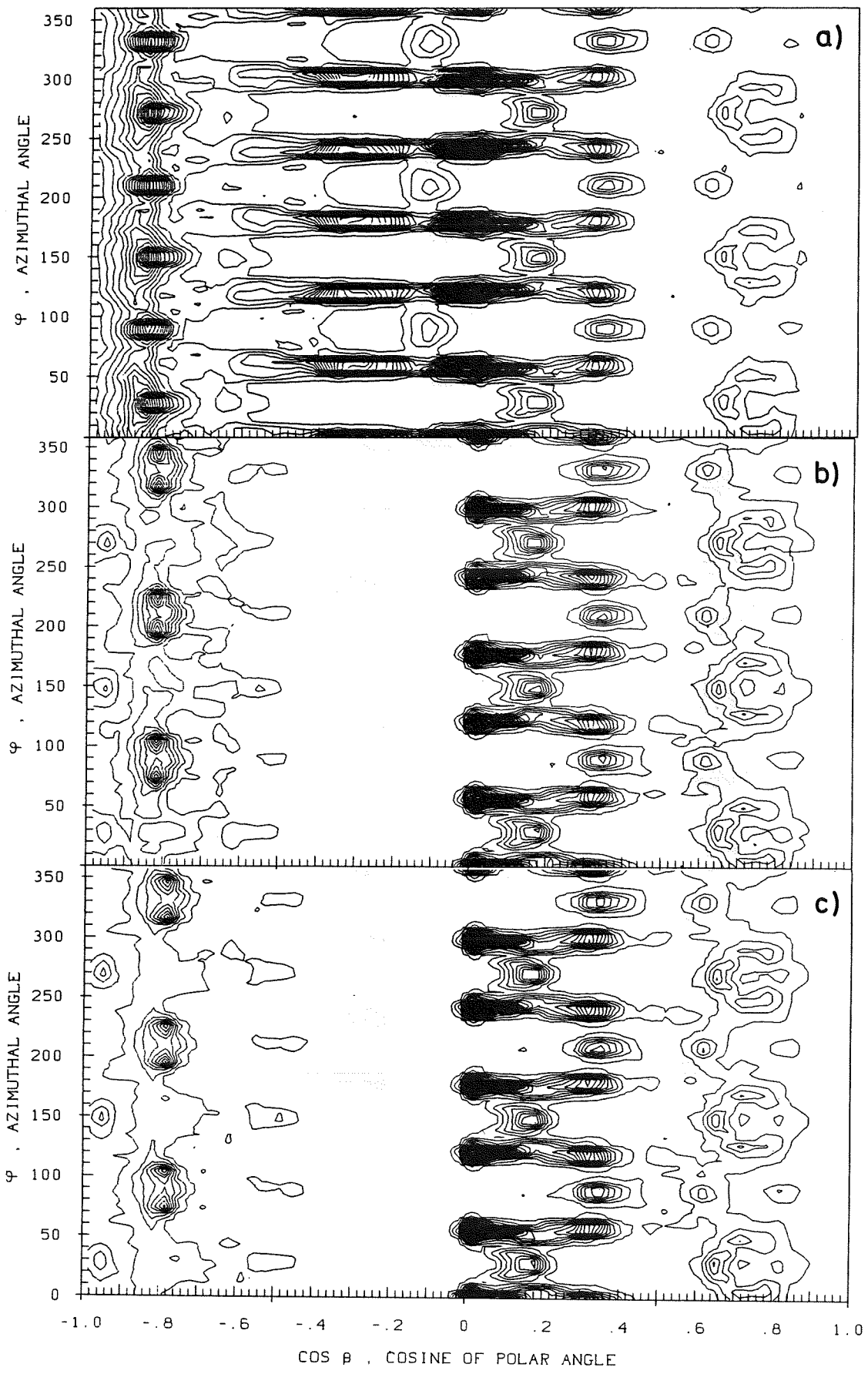
600 EV XE -> AU (111) AT NORMAL INCIDENCE. E3 > E4 > E3/2
a)
b)
c)
φ , AZIMUTHAL ANGLE
350
300
250
200
150
100
50
0
-1.0
-.8
-.6
-.4
-.2
0
.2
.4
.6
.8
1.0
COS β , COSINE OF POLAR ANGLE

Fig. 36a,b,c

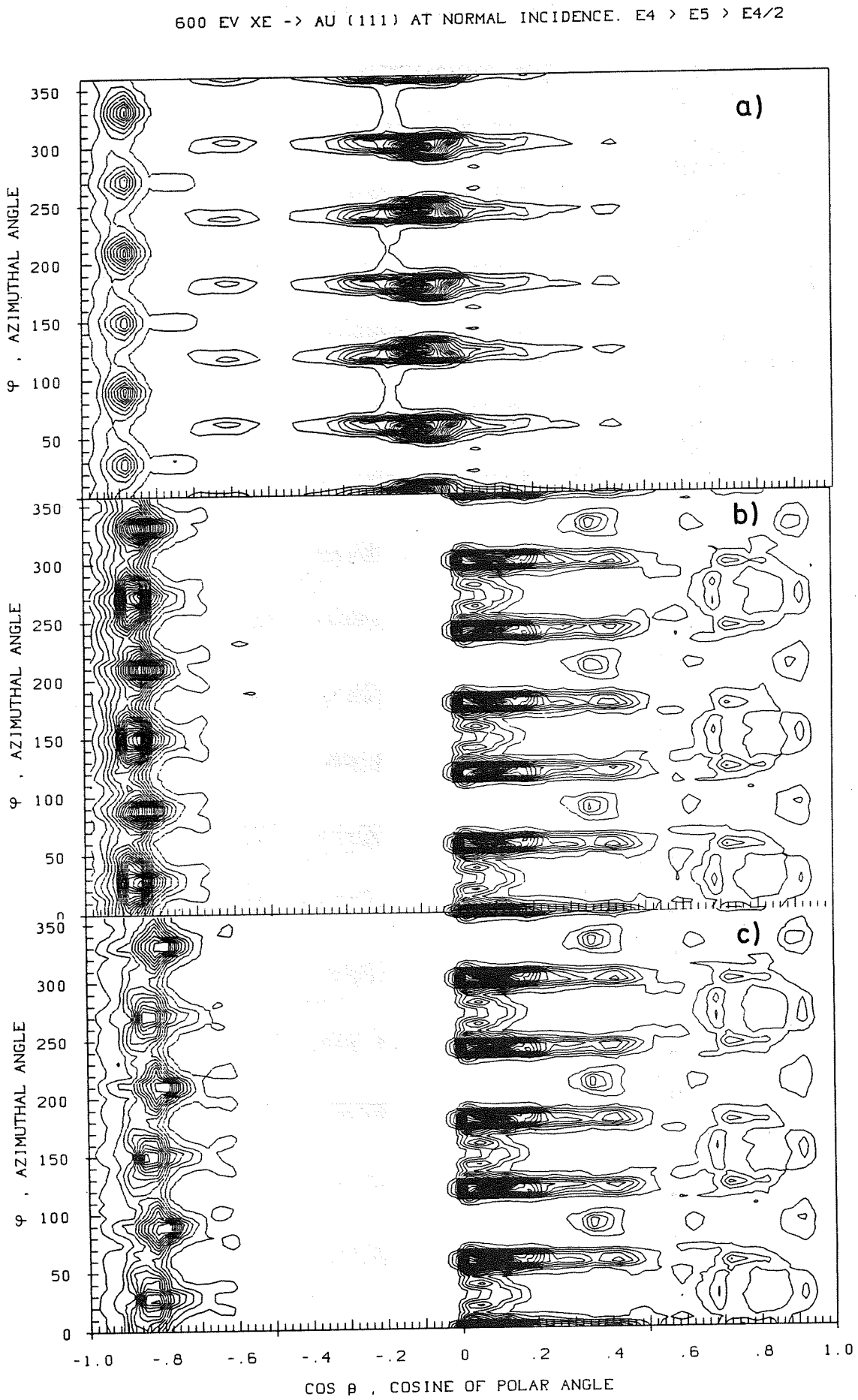
600 EV XE -> AU (111) AT NORMAL INCIDENCE. E4 > E5 > E4/2
a)
b)
c)
φ , AZIMUTHAL ANGLE
φ , AZIMUTHAL ANGLE
φ , AZIMUTHAL ANGLE
350
300
250
200
150
100
50
0
-1.0
-.8
-.6
-.4
-.2
0
.2
.4
.6
.8
1.0
COS β , COSINE OF POLAR ANGLE

Fig. 37a,b,c

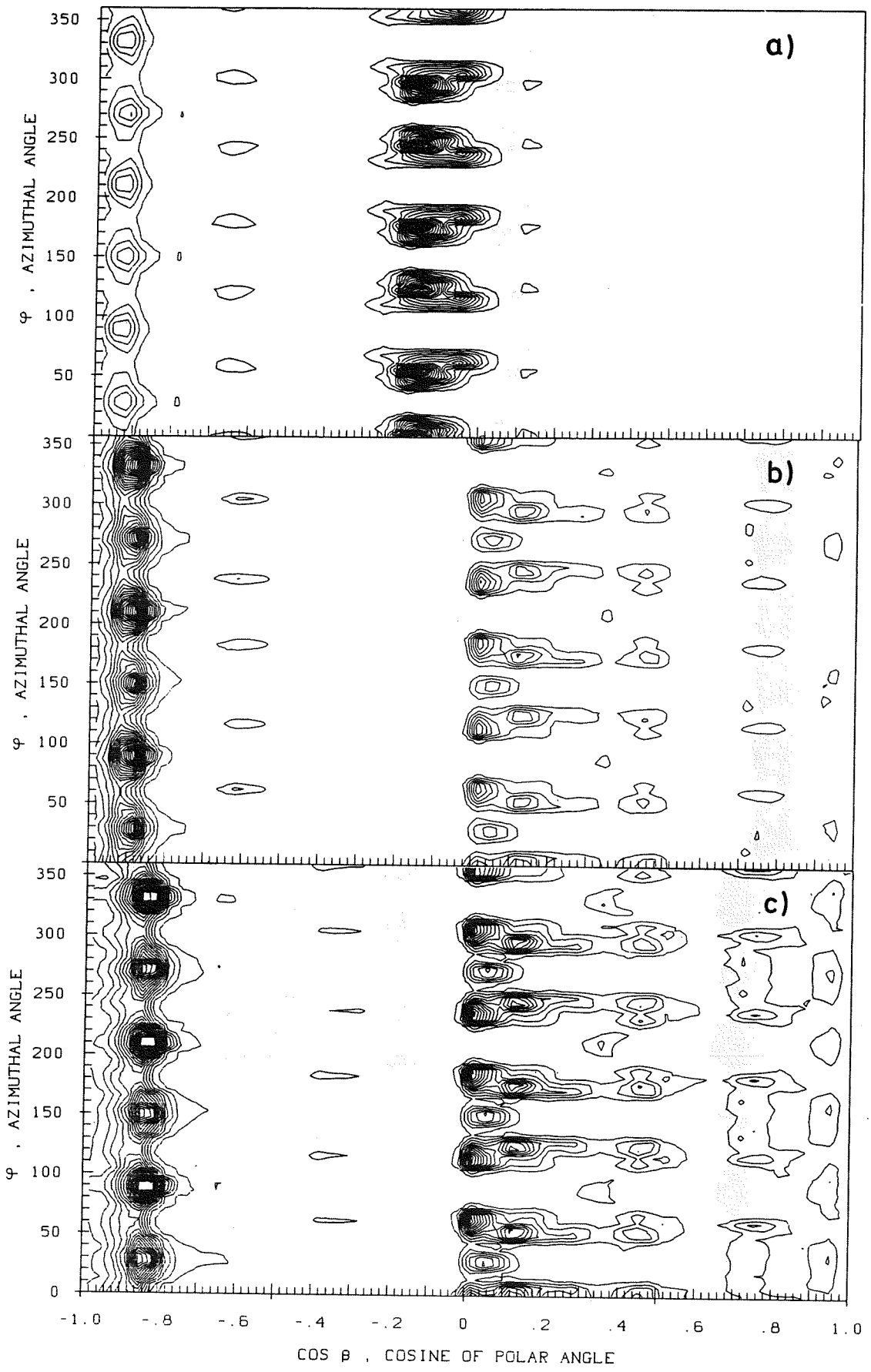
600 EV XE' -> AU (111) AT NORMAL INCIDENCE. E5 > E6 > E5/2
a)
b)
c)
φ , AZIMUTHAL ANGLE
0
50
100
150
200
250
300
350
-1.0
-.8
-.6
-.4
-.2
0
.2
.4
.6
.8
1.0
COS θ , COSINE OF POLAR ANGLE

Fig. 38a,b,c

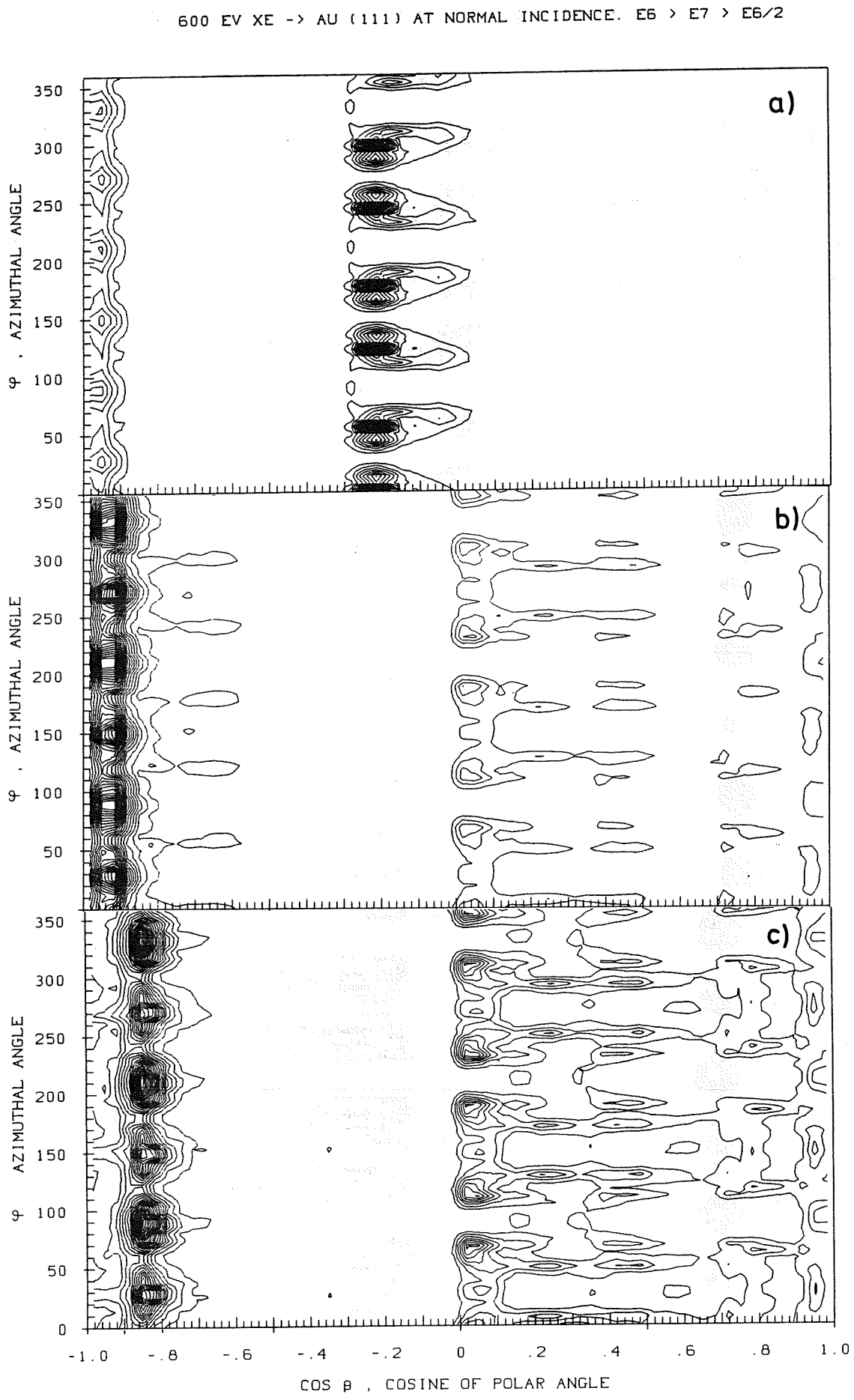
600 EV XE -> AU (111) AT NORMAL INCIDENCE. E6 > E7 > E6/2
a)
b)
c)
φ , AZIMUTHAL ANGLE
350
300
250
200
150
100
50
0
-1.0
-.8
-.6
-.4
-.2
0
.2
.4
.6
.8
1.0
COS β , COSINE OF POLAR ANGLE

Fig. 39a,b,c